1995

Nuclear magnetic resonance: its role as a microscopic probe of the electronic and magnetic properties of high-T[subscript c] superconductors and related materials

Byoung Jin Suh
Iowa State University

INFORMATION TO USERS

This manuscript has been reproduced from the microfilm master. UMI films the text directly from the original or copy submitted. Thus, some thesis and dissertation copies are in typewriter face, while others may be from any type of computer printer.

The quality of this reproduction is dependent upon the quality of the copy submitted. Broken or indistinct print, colored or poor quality illustrations and photographs, print bleedthrough, substandard margins, and improper alignment can adversely affect reproduction.

In the unlikely event that the author did not send UMI a complete manuscript and there are missing pages, these will be noted. Also, if unauthorized copyright material had to be removed, a note will indicate the deletion.

Oversize materials (e.g., maps, drawings, charts) are reproduced by sectioning the original, beginning at the upper left-hand corner and continuing from left to right in equal sections with small overlaps. Each original is also photographed in one exposure and is included in reduced form at the back of the book.

Photographs included in the original manuscript have been reproduced xerographically in this copy. Higher quality 6" x 9" black and white photographic prints are available for any photographs or illustrations appearing in this copy for an additional charge. Contact UMI directly to order.

UMI

A Bell & Howell Information Company
300 North Zeeb Road, Ann Arbor, MI 48106-1346 USA
313/761-4700 800/521-0600

Nuclear Magnetic Resonance: Its role as a microscopic probe of the electronic and magnetic properties of high-T_c superconductors and related materials

by

Byoung Jin Suh

A Dissertation Submitted to the

Graduate Faculty in Partial Fulfillment of the

Requirements for the Degree of

DOCTOR OF PHILOSOPHY

Department: Physics and Astronomy
Major: Condensed Matter Physics

Approved:

Signature was redacted for privacy.

In Charge of Major Work

Signature was redacted for privacy.

For the Major Department

Signature was redacted for privacy.

For the Graduate College

Iowa State University
Ames, Iowa

1995

To Sueyeon and Juwan

TABLE OF CONTENTS

1. INTRODUCTION **1**

2. BACKGROUND **4**

2.1 Theoretical Background 4

2.2 Experimental Background 18

3. NMR AS A PROBE TO STUDY SPIN DYNAMICS AND CORRELATIONS **30**

3.1 Spin Dynamics and Correlations in the Quasi-2D Antiferromagnet $Sr_2CuO_2Cl_2$ from ^{35}Cl NMR in Single Crystals 30

4. NMR AS A MICROSCOPIC PROBE TO STUDY ELECTRONIC AND MAGNETIC PROPERTIES **52**

4.1 Fermi-Liquid Behavior in $HgBa_2CuO_{4+\delta}$ from ^{199}Hg NMR in an Oriented Powder Sample 52

4.2 Electronic and Magnetic Properties of YNi_2B_2C from ^{11}B and ^{89}Y NMR and Magnetic Susceptibility Measurements in Single Crystals 76

5. NMR AS A PROBE TO STUDY THE VORTEX DYNAMICS IN HIGH-T_c SUPERCONDUCTORS **107**

5.1 NMR Investigation of Thermally Activated Flux Motion in $YBa_2Cu_3O_7$ from ^{89}Y Spin-Spin Relaxation Measurements 109

5.2 NMR Investigation of Thermally Activated Flux Motion in $HgBa_2CuO_{4+\delta}$ from ^{199}Hg Spin-Lattice Relaxation Measurements 123

6. SUMMARY AND CONCLUSIONS 134

REFERENCES 136

ACKNOWLEDGMENTS 144

APPENDIX. FIELD-INDUCED ANISOTROPY 145

1. INTRODUCTION

High-T_c superconductors (HTSC's) have fascinated physicists since the discovery of the first HTSC, $La_{2-x}Ba_xCuO_4$ by J. G. Bednorz and K. A. Müller [1]. In particular, the exotic electronic and magnetic properties of the quasi-particles involved in HTSC have received much attention in the attempt to explain the mechanism of the superconducting transition. The symmetry of the pairing in the superconducting state, the properties and the origin of the pseudo-spin gap, and the role of the antiferromagnetic fluctuations and/or correlations are examples of the issues at the basics of HTSC. In spite of the extensive theoretical effort no complete and accepted theory for the HTSC has been yet established.

Nuclear magnetic resonance (NMR) is an extremely versatile spectroscopic tool in solid state physics [2,3]. The power of NMR and nuclear quadrupole resonance (NQR) in the study of solids lies in the fact these techniques can obtain information on static and dynamical properties on the microscopic level. In HTSC, NMR and NQR have played an important role in investigating microscopic electronic and magnetic properties [4-6] thanks to the fortunate circumstance that many suitable nuclei ($^{63,65}Cu$, ^{17}O, ^{89}Y, $^{203,205}Tl$, ^{199}Hg and so on) are present in the cuprate superconductors. Furthermore NMR experiments could be also applied to investigate both the static and dynamical properties of the vortex state, since nuclei are good microscopic probes of local magnetic fields. A number of pioneering NMR works on the vortex state in HTSC have been reported in recent years and are reviewed in Ref. [7].

In this thesis, a series of NMR experiments in several representative HTSC and related materials are reported. We use NMR, as a microscopic probe, to investigate three aspects of superconductors: (i) the structure and dynamics of internal magnetic fields in the parent compounds of HTSC which are predominantly antiferromagnetic insulators, (ii) the

Fermi-liquid behavior of charge carriers in the normal and in the superconducting state, and (iii) the dynamical properties of the vortex state in HTSC which have a fundamental interest as well as a strong impact on possible applications of HTSC.

The thesis is organized as follows. Following a background helpful in reading this thesis such as NMR basics and some experimental aspects in Chapter 2, we summarize in Chapters 3 to 5 our results which have been published already in the scientific literature.

We start in Chapter 3 with the ^{35}Cl NMR and relaxation measurements in the spin S = 1/2 two-dimensional square-lattice Heisenberg antiferromagnet, $Sr_2CuO_2Cl_2$ around the paramagnetic-antiferromagnetic transition. The temperature dependence of the Cu^{2+} spin dynamics is derived from the ^{35}Cl relaxation rates. Important dimensional crossover effects in the correlations of spin dynamics as functions of temperature and of applied magnetic field have been demonstrated for the first time. In Chapter 4 two investigations which typify the kind of microscopic electronic and structural properties which can be obtained with NMR are presented. ^{199}Hg NMR and relaxation measurements were performed in a HTSC, $HgBa_2CuO_{4+\delta}$. All the parameters of the ^{199}Hg NMR are found to be determined by the coupling with the Fermi liquid of the charge carriers. The properties of the Fermi liquid in the normal state and the size and symmetry of the superconducting gap are discussed. Another study presented is ^{11}B and ^{89}Y NMR in a recently discovered quaternary intermetallic compound, YNi_2B_2C. By analyzing the magnetic susceptibility combined with the ^{11}B Knight shift data it was possible to separate the different contributions to the total magnetic susceptibility, i.e. the spin susceptibility of the conduction electrons, the orbital and diamagnetic contributions, and a contribution from a small amount of localized magnetic moments or paramagnetic impurities. In the normal state it is found that the antiferromagnetic fluctuations are negligible contrary to what is found in Cu-based HTSC. The opening of the superconducting gap obeys the predictions of the BCS theory. Chapter 5 reports about NMR studies on the vortex dynamics in two HTSC compounds: $YBa_2Cu_3O_7$ and $HgBa_2CuO_{4+\delta}$. In the section on $YBa_2Cu_3O_7$, thermally activated vortex motion detected by ^{89}Y spin-echo decay measurements is discussed. In the section on

$HgBa_2CuO_{4+\delta}$, the anisotropy in ^{199}Hg spin-lattice relaxation rates and its magnetic field dependence below T_c are presented and explained by an additional relaxation mechanism due to the thermal fluctuations of the vortices. In both cases it is shown that NMR and relaxation can provide useful information on the microscopic correlation time for vortex motion, the activation energy for vortex thermal jumping and the nature of the irreversibility line. The thesis concludes with a summary and the conclusions in Chapter 6.

2. BACKGROUND

The principles of NMR are well known, and we review here only the basic concepts in order to show the kinds of information this technique can provide. NMR experimental conditions and methods are also summarized in this chapter.

2.1 Theoretical Background

The application of a magnetic field $\boldsymbol{H}$ produces an interaction energy with a nucleus with a magnetic moment $\mu = \gamma\hbar\boldsymbol{I}$ according to the Hamiltonian due to so called Zeeman interaction:

$$\mathcal{H} = -\mu \cdot \boldsymbol{H} = \gamma\hbar\boldsymbol{I} \cdot \boldsymbol{H}. \tag{2.1}$$

Taking the field to be H_0 along the z direction, we find the eigenvalues of the Hamiltonian are $E = -\gamma\hbar H_0 m$ with $m = I, I\text{-}1, ..., -I$.

NMR is a typical resonance technique to detect the presence of such a set of energy levels by the form of spectral absorption. What is needed is to have an interaction that can cause transitions between levels. The coupling which produces magnetic resonances is an alternating magnetic field perpendicular to the applied static field. By the conservation of energy the angular frequency, ω, of the alternating or the radiofrequency (rf) field for the transition between the levels adjacent in energy is given by

$$\hbar\omega = \Delta E = \gamma\hbar H_0 \text{ or}$$
$$\omega = \gamma H_0. \tag{2.2}$$

Therefore, the NMR spectrum can be characterized by a sharp absorption line at the frequency $\nu_L = \omega_L/2\pi = \gamma H_0/2\pi$ where ν_L (or ω_L) is called a "Larmor frequency" and is the characteristic frequency of the given nucleus. However, this is only for the case of bare nuclei in the absence of any other interactions except the Zeeman interaction. For the nuclei in a condensed matter system, we can easily imagine that the NMR spectrum will exhibit a shift of the resonance frequency with respect to the Larmor frequency ν_L and/or a broadening of the NMR line due to the presence of additional local interactions.

In fact, the relative frequency shift with respect to ν_L and the linewidth of the NMR spectrum are important parameters of NMR are used to obtain information on the static properties of the local fields generated by the couplings of the probing nuclei with the environments, e.g. conduction electrons in a metal. In the following, we briefly review the local interactions and their contributions to NMR parameters.

2.1.1 The Hamiltonian

The complete Hamiltonian for a condensed matter system of nuclear spins I in an external magnetic field is given by:

$$\mathcal{H} = \mathcal{H}_Z + \mathcal{H}_{dip} + \mathcal{H}_Q + \mathcal{H}_{hf}\ , \tag{2.3}$$

where $\mathcal{H}_Z$ is the Zeeman coupling between the nuclear spin system and the external magnetic field which is already discussed above, $\mathcal{H}_{dip}$ is the nuclear dipolar interaction, $\mathcal{H}_Q$

is the electric quadrupole interaction, and $\mathcal{H}_{hf}$ is the hyperfine coupling between the nuclear spins and the local magnetic fields induced by electron spins and/or orbital motion.

2.1.1.1 Nuclear Dipolar Coupling

The nuclear dipolar interaction $\mathcal{H}_{dip}$ between nuclear spins:

$$\mathcal{H}_{dip} = \sum_{j<i} \frac{\hbar^2 \gamma^2}{r_{jk}^3} \left[\boldsymbol{I}_j \cdot \boldsymbol{I}_k - 3 \frac{\left(\boldsymbol{I}_j \cdot \vec{r}_{jk}\right)\left(\boldsymbol{I}_k \cdot \vec{r}_{jk}\right)}{r_{jk}^2} \right], \tag{2.4}$$

can in general be treated as a perturbation of the Zeeman Hamiltonian, and is responsible for the "homogeneous" broadening of the NMR line.

In solids, a reasonable picture of the real situation is given by the "rigid lattice" approximation, in which nuclear positions are fixed. A quantitative evaluation of the broadening of the resonance lines due to nuclear spin-spin coupling can be obtained by calculating the moments of the resonance line. For a normalized shape function $f(\omega)$ with a maximum at the frequency ω_0, the moment of order n with respect to ω_0 is given by

$$M_n = \int (\omega - \omega_0)^n f(\omega) d\omega. \tag{2.5}$$

In the case of a Gaussian line shape, the second moment corresponds to the square of the width. On the basis of the Hamiltonian Eq. (2.4), the second moment of the line due to the dipolar interaction between like nuclei can be calculated, giving the so called Van Vleck second moment:

$$M_2 = \frac{3}{4} \gamma^4 \hbar^2 I(I+1) \sum_k \frac{(1 - 3\cos^2 \theta_{jk})^2}{r_{jk}^6}, \tag{2.6}$$

where r_{jk} is the distance between the spin $\boldsymbol{I}_j$ and $\boldsymbol{I}_k$ and θ_{jk} is the angle between $\vec{r}_{jk}$ and the external field $\boldsymbol{H}$. The extension of this expression to the case of the interaction between unlike nuclei can be found in Ref. [2] together with the corrections necessary when quadrupole couplings are effective.

2.1.1.2 Electric Quadupole Coupling

The nuclear quadrupole coupling is the interaction between the nuclear charge cloud and the electric field gradient created by surrounding electrons. Classically this arises from the finite extension of the nuclear charge, which can give rise to a nuclear quadrupole moment. In bulk matter the electric field gradient (EFG) is defined by the tensor

$$V_{ij} = \left(\frac{\partial^2 V}{\partial x_i \partial x_j} \right), \tag{2.7}$$

where V is the electrostatic crystal potential. Employing the choice of principal axes,

$$\frac{\partial^2 V}{\partial x^2} \leq \frac{\partial^2 V}{\partial y^2} \leq \frac{\partial^2 V}{\partial z^2}, \tag{2.8}$$

in the coordinate frame of the principal axes, the quadrupole Hamiltonian is given by

$$\mathcal{H}_Q = \frac{e^2 qQ}{4I(2I-1)} \left[3I_Z^2 - I(I+1) + \frac{1}{2}\eta(I_+^2 + I_-^2) \right], \tag{2.9}$$

where $eq = V_{zz}$, $\eta = (V_{xx} - V_{yy})/V_{zz}$, $I_\pm = I_x \pm iI_y$ and Q is a quantity characteristic of the given nucleus, called the quadrupole moment, which vanishes for nuclei with spin $I = 1/2$.

In the case of high magnetic fields, or whenever the Zeeman coupling is much stronger than the quadupole coupling, $\mathcal{H}_Q$ can be treated by a perturbative approach. The

energy levels depend on the mutual orientation of the principal axis of the EFG tensor and the external magnetic field $\boldsymbol{H}$. Let θ be the angle between the z axis of the EFG tensor and $\boldsymbol{H}$ and consider the simple case of an axially symmetric EFG, where $\eta = 0$. To simplify the notation, we define:

$$\nu_Q = \frac{3e^2Q}{2I(2I-1)h}, \quad \mu = \cos\theta . \tag{2.10}$$

Then the transition frequency after the first and second order perturbation corrections is given by

$$\nu(m \leftrightarrow m-1) = \nu_L + \frac{1}{2\nu_Q}(m-\frac{1}{2})(3\mu^2-1) + \frac{\nu_Q^2}{32\nu_L}(1-\mu^2)$$
$$\times \left\{\left[102m(m-1) - 18I(I+1) + 39\right]\mu^2 - \left[6m(m-1) - 2I(I+1) + 3\right]\right\}, \tag{2.11}$$

where the second and third terms are from the first and second order quadrupole effects respectively. It is seen that for half-integer spin the central line (1/2↔-1/2) is affected only by the second order effect. Eq. (2.11) also indicates that the first order effect generates $2I$ resonance lines in the NMR spectrum including the unperturbed central line.

2.1.1.3 Hyperfine Coupling

The hyperfine coupling is the magnetic interaction between nuclear spins and surrounding electrons. There are several kinds of magnetic hyperfine couplings and the Hamiltonian as given, for example, by Bloembergen and Rowland [8] is

$$\mathcal{H} = 2\cdot\frac{8\pi}{3}\mu_B\gamma_N\hbar\boldsymbol{I}\cdot\boldsymbol{S}(\boldsymbol{r})\delta(\boldsymbol{r}) - 2\mu_B\gamma_N\hbar\boldsymbol{I}\cdot\left[\frac{\boldsymbol{S}}{r^3} - \frac{3\boldsymbol{r}(\boldsymbol{S}\cdot\boldsymbol{r})}{r^5}\right] - \gamma_N\hbar\frac{e}{mc}\left[\boldsymbol{I}\cdot\frac{(\boldsymbol{r}\times\boldsymbol{p})}{r^3}\right], \tag{2.12}$$

where μ_B is the Bohr magneton, γ_N is the nuclear gyromagnetic ratio, $\boldsymbol{I}$ and $\boldsymbol{S}$ are the nuclear spin and electron spin respectively, $\boldsymbol{r}$ is the radius vector of the electron with nucleus at the origin, and $\boldsymbol{p}$ is the linear momentum of the electron.

The first term in Eq. (2.12) is the Fermi contact interaction term. It was first employed to explain NMR shifts (the so-called Knight shift, discussed below) for "simple" metals, where *s*-wave functions describe the major part of the conduction electrons [9]. It is noted that only *s*-electrons or the *s*-component of the electronic wave-function, have non-zero probability density at the nuclear sites, and can contribute to the contact interaction. The second term represents the spin dipolar interaction between nuclear and electron spins, which causes an anisotropic Knight shift in the absence of cubic symmetry. This interaction is particularly important in the case of the presence of localized electron spins in paramagnetic insulators. The anisotropic Knight shift is defined in the next section. The third term represents the interaction of the nuclear spin with the magnetic moment associated with the orbital motion of the electron induced by the applied magnetic field. This interaction can be important in some *d*-band transition metals and is related to the Van Vleck paramagnetism.

2.1.2 NMR Parameters

2.1.2.1 Knight Shift (*K*)

The Knight shift K of a metal is defined as the relative shift of the resonance frequency of the metal, ν_m, with respect to the resonance frequency of a suitable reference material, ν_r, at a given external field $\boldsymbol{H} = H_0\mathbf{k}$ as:

$$K \equiv \frac{\nu_m - \nu_r}{\nu_r} = \frac{\langle \Delta H \rangle}{H_0} . \tag{2.13}$$

That is, the Knight shift is the direct measurement of the magnitude of the local field $\Delta \boldsymbol{H}$ induced by the hyperfine interactions. A diamagnetic ionic salt is most often used for the reference compound. It is noted that various diamagnetic contributions from *s* and *p* valence and closed shell electrons (atomic cores) in the reference compound produce small but measurable magnetic fields at the nucleus which oppose the applied field and thus shift the resonance in a diamagnetic sense, but it is assumed that the magnetic field at the nucleus is shifted by the same amount in the metal and in the salt when the conduction bands become populated. This kind of shift is defined as "chemical shift", δ.

2.1.2.2 Nuclear Spin-Lattice Relaxation Rate (NSLR, T_1^{-1}, or R_1)

When the system of nuclear spins in the external field is perturbed by the irradiation with rf field at ν_L, it recovers to thermal equilibrium by interacting with all the available degrees of freedom of the system (electrons, phonons, diffusion processes and so on) which are usually called the "lattice". The characteristic recovery time is called the "spin-lattice relaxation time", T_1, and its inverse is called the "spin-lattice relaxation rate", T_1^{-1} or R_1. The exact source of the nuclear spin-lattice relaxation rate (NSLR) is the fluctuating part of the local magnetic field $\Delta \boldsymbol{H}$ induced by the interaction of the nucleus with its surroundings (lattice). For an exponential recovery of the magnetization, the relaxation rate due to a fluctuating local field is expressed in terms of the transition probability, *W*. For weak time dependent fluctuations of the local field and from time dependent perturbation theory [2,3] one has

$$\frac{1}{T_1} = 2W = \frac{\gamma^2}{2} \int_{-\infty}^{+\infty} \langle \Delta H_+(t) \Delta H_-(0) \rangle \, e^{i\omega_L t'} dt \,, \tag{2.14}$$

where ω_L is the Larmor frequency and $\Delta H_\pm = \Delta H_x \pm i\Delta H_y$, when taking the direction of the total magnetic field $\boldsymbol{H} + \Delta \boldsymbol{H}$ as the *z* axis. The Fourier transform of the correlation function of the local-field components, $\int_{-\infty}^{+\infty} \langle \Delta H_+(t) \Delta H_-(0) \rangle \, e^{i\omega_L t'} dt$, represents the spectral density,

discussed in chapter 3. The expression (2.14) is quite general so it can be applied for the case of the local-field fluctuation modulated by the relative motion of the nucleus with respect to an inhomogeneous magnetic field such as vortex motion in HTSC [10], discussed in chapter 5.

2.1.2.3 Nuclear Spin-Spin Relaxation Rate (T_2^{-1})

Besides spin-lattice relaxation, we will encounter several other relaxation processes, the most prominent being spin-spin relaxation. A possible simple mechanism for the spin-spin relaxation for solids in which the large concentrations and correspondingly the small distance between nuclear spins exist arises from the relatively strong spin interactions. The tight coupling between the spins allows rapid energy transfer from one spin to another, leading to the establishment of a thermal equilibrium inside the nuclear spin system itself. This process is the spin-spin relaxation and its characteristic time is called the "spin-spin relaxation time", T_2, and its inverse T_2^{-1} is called the "spin-spin relaxation rate". Since energy exchange between spins conserves the total energy of the spin system, in contrast to spin-lattice relaxation, there is no necessity of transfer of energy to a heat reservoir (lattice) for the spin-spin relaxation. The T_2-process is described in a classical description in terms of the decay of the transverse magnetization, which is a more visible way to understand the process and will be discussed in more detail later.

2.1.3 NMR in Metals: The Korringa Relation

The source of the Knight shift first used to interpret shifts in simple metals was that of the Fermi contact interaction term between the resonating nucleus and the *s*-electrons. According to the theory first proposed by Townes, Herring and Knight [9],

$$K = \frac{8\pi}{3}\chi_p \left\langle |\psi_s(0)|^2 \right\rangle_{FS} , \qquad (2.15)$$

where χ_p is the Pauli paramagnetic spin susceptibility per atom, and $<|\psi(0)|^2>_{FS}$ is the square of the s-wave function at the nuclear sites averaged over those electrons at the Fermi surface (FS).

In simple *s*-band metals, the contact term dominates in both the Knight shift and nuclear spin-lattice relaxation rate (NSLR). Korringa derived for an independent particle model, the so called Korringa relation [11]:

$$K^2 T_1 T = S,$$
$$S \equiv \frac{h}{8\pi^2 k_B}\left(\frac{\gamma_e}{\gamma_N}\right)^2, \tag{2.16}$$

where γ_e and γ_N are the gyromagnetic ratios of the free electron and the nucleus, respectively and k_B is the Boltzmann constant. It is convenient to describe the deviation from the ideal behavior by so-called Korringa ratio:

$$\kappa \equiv \frac{K^2 T_1 T}{S}, \tag{2.17}$$

which, in ideal case, is equal to unity.

The deviations from unity in the Korringa ratio can arise from a number of sources. Electron-electron interactions, which affect K and T_1 differently, are a common cause of the deviations from unity. The Korringa-type relation does not hold for the orbital contribution to K and to T_1. The orbital Knight shift depends on an average density of states throughout the band, whereas the orbital contribution to T_1 depends upon the density of states at the Fermi surface. For example, in superconductors the orbital relaxation rate goes to zero as the temperature goes to zero, whereas the orbital Knight shift often remains finite.

2.1.4 NMR in HTSC

A variety of experiments and theoretical descriptions have emphasized the role of Cu^{2+} spins in HTSC which affect the normal state behavior and may be related to the mechanism driving the superconducting transition. Thus the microscopic study of spin susceptibility including its dynamical properties both in the normal and in the superconducting state of HTSC is one of the main issues in HTSC. NMR has offered the most powerful tools to investigate the microscopic properties of the spin system in HTSC. We briefly discuss what kinds of information on the electronic and magnetic properties of HTSC are provided by NMR technique.

The simple expression (2.15) for the Knight shift which represents only the effects of the contact hyperfine interaction in the Hamiltonian (2.12) can be generalized to include the other hyperfine interactions. In order to focus on the spin contribution, it is convenient to decompose the total shift K^{tot} into spin (K^{sp}) and orbital contributions (K^{orb})

$$K_\alpha^{tot}(T) = K_\alpha^{sp}(T) + K_\alpha^{orb}\ , \tag{2.18}$$

where α is an index which specifies the orientation of the external magnetic field with respect to the crystal axis system and K^{orb} is the sum of the Van Vleck term K^{VV} and the chemical shift δ. By analogy to Eq. (2.15), the two contributions to K in Eq. (2.18) can be expressed in terms of the hyperfine coupling constant A and of the static local susceptibility χ as [12]:

$$\begin{aligned} K_\alpha^{sp} &= A_\alpha^{sp}\chi_\alpha^{sp}\ , \\ K_\alpha^{orb} &= A_\alpha^{orb}\chi_\alpha^{orb} + \delta . \end{aligned} \tag{2.19}$$

As discussed before, in superconductors or HTSC, K^{orb} remains temperature-independent below the superconducting transition temperature T_c, whereas K^{sp} is expected to decrease with decreasing temperature in the superconducting state due to the decrease of the quasiparticle density of states at the Fermi level as a result of the opening of the superconducting gap.

While the Knight shift yields direct information on the uniform spin susceptibility, the nuclear spin-lattice relaxation rate (NSLR, T_1^{-1}) offers a tool to investigate the dynamical spin susceptibility. The NSLR, T_1^{-1}, in Eq. (2.15) can be written in terms of the imaginary part of the generalized dynamical spin susceptibility, χ'' [13]:

$$\left(\frac{1}{T_1 T}\right)_\alpha = \sum_q |A_\alpha(\vec{q})|^2 \frac{\chi''(\vec{q},\omega_L)}{\omega_L}, \qquad A_\alpha(\vec{q}) = \sum_j (A_j)_\alpha e^{i\vec{q}\cdot\vec{r}_j}, \tag{2.20}$$

where, ω_L is the nuclear resonance frequency. If one models the generalized susceptibility $\chi(q,\omega)$ for a highly correlated electronic system [14] then the NSLR can yield useful information through Eq. (2.20). One of the main issues in HTSC is whether the Fermi liquid of doped oxygen holes and the Cu *d*-electrons form a single spin fluid described by a unique spin susceptibility $\chi(q,\omega)$ or by the sum of two independent contributions: $\chi(q,\omega) = \chi_o(q,\omega) + \chi_{AF}(q,\omega)$. In either case the Cu spins which are strongly coupled by an antiferromagnetic (AF) exchange interaction are expected to give rise to an enhanced susceptibility for $q = q_{AF}$. The presence of the filtering factors $A(q)$ in Eq. (2.20) allows one to use different nuclei with different local symmetry in the same system to probe different regions in q-space of $\chi(q,\omega)$. It is noted that in the presence of weakly interacting Fermi gas and for a direct contact hyperfine interaction of the conduction electrons with the nucleus the expression (2.20) reduces to the Korringa relation [13].

The spin-spin relation rate, T_2^{-1}, in HTSC has proved to be an important tool to study the static spin susceptibility. It has been shown that the Gaussian contribution, T_G^{-1}, to the

spin-spin relaxation rate of planar Cu in YBCO compounds is much stronger than expected from the nuclear dipolar-dipolar coupling [15,16]. The effect is due to an enhanced Cu nuclear-nuclear spin coupling induced through an indirect coupling via electron spins and can therefore be related to the static spin susceptibility [17,18]. Contrary to the Knight shift which probes only the $q = 0$ component of the susceptibility, T_G^{-1} can give information on the q-dependence of $\chi'(q)$.

The fact that T_G^{-1} probes $\chi'(q)$ allows one to test the opening of a gap in the spin excitation spectrum, a so called spin pseudo-gap, by comparing T_G^{-1} with the spin-lattice relaxation rates [4,5,19].

2.1.5 NMR at Phase Transitions

A phase transition is a typical effect related to the collective behavior of a many-particle interacting system. A convenient description of the collective behavior is usually done in terms of correlation functions.

NMR and NQR measurements, both of static and dynamical parameters, provide valuable insights into the local properties at phase transitions. In these techniques the nucleus is used as a probe of the electric and magnetic interactions in the system at the microscopic level. In particular, nuclear relaxation rate measurements are suitable for investigating the long-time behavior of the correlation functions which is of special importance in presence of slowing-down of the fluctuations occurring around the critical points in structural and magnetic transitions.

By introducing, as an example, the discussion about the critical dynamics in the paramagnetic phase of a spin $S = 1/2$ 2D Heisenberg antiferromagnetic (AF) system [20] we briefly review how the relaxation rate can be related to the correlation of the local critical variables that reflects the critical effects.

We start with the general expression (2.14) for NSLR. For a paramagnetic system, $\Delta \boldsymbol{H}(t)$ in Eq. (2.14) represents the local field at the nuclear sites due to the nucleus-electron hyperfine coupling including the dipolar part which should be relevant in the case we discuss here. Let the spin components of the localized electronic spins be $S_\alpha(t)$ and assume isotropic fluctuations of the S_α components (Heisenberg model). Then Eq. (2.14) can be rewritten in terms of the collective spin components $\boldsymbol{S}_\mathbf{q}$ in the form [21]:

$$\begin{aligned} 2W &= \frac{\gamma^2}{2}\frac{1}{N}\sum_{\mathbf{q}}\left|\Delta \boldsymbol{H}_\mathbf{q}\right|^2 \int\left\langle S_\mathbf{q}^+(t)S_\mathbf{q}^-(0)\right\rangle dt \\ &= \gamma^2 \frac{1}{N}\sum_{\mathbf{q}}\left|\Delta \boldsymbol{H}_\mathbf{q}\right|^2\left|S_\mathbf{q}\right|^2 \Big/ \Gamma_\mathbf{q}\,, \end{aligned} \tag{2.21}$$

where $|\boldsymbol{S}_\mathbf{q}|^2$ is the mean square amplitude and $\Gamma_\mathbf{q}$ is the decay rate of the collective spin fluctuations, while $\Delta \boldsymbol{H}_\mathbf{q}$ is the Fourier transform of the lattice functions which couple the nucleus to the spins S_i(t). In the case that the hyperfine field at the probing nucleus does not cancel for an AF arrangement of the spins, one expects the main contribution to the relaxation rate of the nucleus to come from AF fluctuations. By expanding the $\Delta \boldsymbol{H}_\mathbf{q}$ factor around the value corresponding to the critical wave vector q_{AF} describing the staggered order below the 3D ordering temperature, T_N, and by using conventional scaling arguments [22] for the $\mathbf{q}$ dependence of the in-plane correlated fluctuations, Eq. (2.21) becomes

$$2W = (\gamma \hbar_{eff})^2 \frac{1}{N}\sum_q \frac{\xi^{2-\eta} f(q\xi)}{\omega_e \xi^{-z} g(q\xi)}\,, \tag{2.22}$$

where z and η are critical scaling exponents [22] and h_{eff} is the static field at the nuclear site resulting from the spin configuration of the ordered magnetic structure while $\mathbf{q}$ is the 2D wave vector measured with respect to q_{AF}. In Eq. (2.22), we have written $|\boldsymbol{S}_\mathbf{q}|^2$ in terms of the correlation length (in lattice units) while the decay rate of the fluctuations $\Gamma_\mathbf{q}$ has been

expressed by a scaling form in terms of the Heisenberg exchange frequency ω_e: $\Gamma_q = (\omega_e/\xi^z)g(q\xi)$, z being a characteristic dynamical scaling exponent, and $f(q\xi)$ and $g(q\xi)$ are homogeneous functions of the product $x = q\xi$. By transforming the q summation in Eq. (2.22) into a 2D integral and taking into account the convergence of $\int[f(x)/g(x)]dx$ to a number of the order of unity, one finally has

$$2W = (\gamma\hbar_{eff})^2 \frac{1}{\omega_e} \xi^{z-\eta}, \tag{2.23}$$

where $\omega_e = [(8/3)J^2nS(S+1)]^{1/2}/\hbar$ with J, the electronic spin exchange interaction and n, the number of nearest-neighbor magnetic ions. It is noted that in the high-temperature limit of no correlation ($\xi \to 1$), Eq. (2.23) reduces to the well-known result for paramagnets [23] with $(h_{eff})^2 = \Sigma < h_i^2 >$.

Eq. (2.23) is a simple relation which allows one to obtain the static correlation length ξ from the NSLR. It is noted that the derivation of the static properties (ξ) from the dynamical properties (NSLR) is valid only if the scaling of Γ_q with ξ is fulfilled. The relation (2.23) will be used in the study of the NSLR in $Sr_2CuO_2Cl_2$ [24], discussed in chapter 3. The local critical variable chosen here is one or more of the spin components $S_\alpha(t)$. This method can be applied also to other phase transitions or collective phenomena when a suitable local critical variable is chosen. More detailed and rigorous discussions appear in Ref. [21].

2.2 Experimental Background

2.2.1 NMR Instrumentation

2.2.1.1 NMR Spectrometer

The NMR measurements were performed with home-built coherent Fourier transform pulse spectrometers employing a programmable pulse sequencer [25]. The receiver was similar to that of [26] consisting of a preamplifier and three limiting amplifier stages, with the addition of a phase sensitive quadrature detector and a modified Evans Electronic Model 4139A fast leakage, gated integrator. A four-phase rf switch employing a double sideband, together with the pulse programmer, supplied the rf pulses. High-speed data acquisition, signal averaging, and fast Fourier transformation were accomplished with a combination of Hewlett-Packard 54504A or LeCroy 9410 digitizing oscilloscopes with a National Instruments IEEE-488 interface to a Digital Equipment Cooperation LSI-11/73 computer.

2.2.1.2 Probe and Temperature Control Unit

The wide frequency-range tunable probe with a single coil and tuning and matching capacitors was specially designed to fit to an Oxford Instruments CF1200 continuous flow cryostat. Low temperature was obtained by flowing liquid He or liquid N_2 through the cryostat using an Oxford Instruments GFS type transfer tube. Temperature was controlled from 4.2 K to 500 K with an Oxford Instruments ITC-4 temperature controller. The sample temperature was measured using (Au-0.07% Fe)/Chromel or Chromel/Constantan thermocouples.

2.2.2 Experimental Methods

In this section, basic concepts and techniques of experimental Fourier transform (FT) pulse NMR which are useful to understand how to measure the NMR parameters are introduced.

2.2.2.1 Classical Description

According to the classical theory of electromagnetism, a magnetic moment μ in a magnetic field $\boldsymbol{H}$ experiences a torque $\tau = \mu \times \boldsymbol{H}$, which is equal to the rate of change of its angular momentum. Since $\mu = \gamma\hbar\boldsymbol{I}$, we can describe the motion of the magnetic moment by the equation

$$\frac{d\mu}{dt} = \mu \times \gamma\boldsymbol{H} . \tag{2.24}$$

It is useful to describe the motion in a rotating frame. In a frame rotating with a angular velocity ω with respect to the laboratory frame the equation of motion is rewritten as

$$\frac{\delta\mu}{\delta t} = \mu \times \gamma(\boldsymbol{H} + \frac{\omega}{\gamma}) . \tag{2.25}$$

This has the same form as Eq. (2.24) provided the external field $\boldsymbol{H}$ is replaced by an effective field $\boldsymbol{H}_{\text{eff}} = \boldsymbol{H} + \omega/\gamma$. We can now readily solve for the motion of μ in a static field $\boldsymbol{H} = H_0\mathbf{k}$ by choosing ω such that $\boldsymbol{H}_{\text{eff}} = 0$, i.e. $\omega = -\gamma H_0\mathbf{k}$. Since in this reference frame $\delta\mu/\delta t = 0$, μ remains fixed with respect to $\mathbf{i}$, $\mathbf{j}$, and $\mathbf{k}$, so that the motion with respect to the laboratory frame is that of a vector fixed in a set of axes which themselves rotate at $\omega = -\gamma H_0\mathbf{k}$. In other words, μ rotates at an angular frequency $\omega = -\gamma H_0\mathbf{k}$ with respect to the laboratory. The angular frequency γH_0 is called the "Larmor frequency". We like to stress

that the classical precession frequency ω is identical in magnitude with the angular frequency ω_L needed for magnetic resonance absorption, as found by elementary quantum theory discussed in the previous section. This correspondence of the classical and quantum mechanical treatments allows one to describe the resonance phenomena as a motion of the expectation value of the magnetic moment, μ, which is a classical vector.

2.2.2.2 Free Induction Decay (FID) and Spin Echoes

Now we extend the equation of motion to the case with an additional perturbing rf field $\boldsymbol{H}_1$. Suppose $\boldsymbol{H}_1 = H_1\mathbf{i}$ is fixed in the rotating frame, i.e. $\boldsymbol{H}_1$ is perpendicular to $\boldsymbol{H}$ and rotating around $\boldsymbol{H}$ with the angular frequency ω of the rotating frame. Then we can write the equation of motion:

$$\frac{\delta\mu}{\delta t} = \mu \times \gamma\left[(H_0 + \frac{\omega}{\gamma})\mathbf{k} + H_1\mathbf{i}\right] = \mu \times \gamma\boldsymbol{H}_{\text{eff}} . \qquad (2.26)$$

Physically, Eq. (2.26) states that in the rotating frame, the moment acts as though it is experiencing effectively a static magnetic field $\boldsymbol{H}_{\text{eff}} = (H_0 + \omega/\gamma)\mathbf{k} + H_1\mathbf{i}$. If the resonance condition is fulfilled exactly ($\omega = -\gamma H_0\mathbf{k}$), the effective field is then simply $H_1\mathbf{i}$. The magnetic moment that is initially parallel to the static field will then precess in the y-z plane. If we turn on H_1 for a short time, t_p, by applying a radio frequency "pulse" the moment would precess through an angle $\theta = \gamma H_1 t_p$. If t_p were chosen such that $\theta = \pi/2$ (90 degree pulse), the moment is turned from the z-direction to the y-direction. Following the turn-off of H_1, the moment would then remain at rest in the rotating frame, and hence precess in the laboratory pointing normal to the static field.

This model suggests a very simple method of observing magnetic resonance. We put a sample we wish to study in a coil, the axis of which is oriented perpendicular to the external field $\boldsymbol{H}$. In thermal equilibrium there will be an excess of moments pointing along $\boldsymbol{H}$. Application of an alternating voltage with an angular frequency of the Larmor

frequency to the coil produces a rf field perpendicular to $\boldsymbol{H}$. By adjusting H_1 and t_p, we may apply a $\pi/2$ pulse. Following the pulse, the average magnetization will be perpendicular to $\boldsymbol{H}$ and will precess at angular frequency γH_0. As a result, the moments will produce a flux through the coil which will alternate as the spins precess. The resultant induced electromotive force (emf) may be observed.

What we have suggested so far would indicate that the induced emf would persist indefinitely, but in practice, the interactions of the spins with their surroundings cause a decay, so called "free induction decay (FID)" (i.e. decay "free" of H_1). It is noted that the situation in which the excess magnetic moments are in the plane perpendicular to $\boldsymbol{H}$ corresponds to a zero average magnetization projection in the direction of the applied field. This is not a thermal equilibrium situation. The recovery of the system towards equilibrium which implies the growth of the average magnetization along $\boldsymbol{H}$ is determined by the spin-lattice relaxation time.

Now consider what would happen if we apply a second rf pulse a time τ after the first. Actually, Hahn did it first and made the remarkable discovery that there appeared another free induction signal at a time 2τ after the initial pulse [27]. He named the signal the "spin echo". The discovery of spin echo provided the key impetus to the development of pulse NMR and must therefore be ranked among the most significant contributions to magnetic resonance.

To produce a signal at the time of the echo, the spins must somehow have gotten back in phase. The essential physical ideas of refocusing can be mostly easily seen by considering a pulse sequence in which the first pulse produces a rotation of $\pi/2$, the second a rotation of π instead of the $\pi/2$ again which were used by Hahn originally. Such a sequence we denote as a $\pi/2$ - π pulse sequence. Consider a group of spins initially in thermal equilibrium in a static field in the z-direction. The thermal equilibrium magnetization $\boldsymbol{M}_0$ then lies along $\boldsymbol{H}$ as shown in Fig. 2.1(a). We assume there is a spread in magnetic fields over the sample, and take the average value of the field to be H_0. Application of a $\pi/2$ pulse using $\boldsymbol{H}_1 = H_1\mathbf{i}$ in the rotating frame rotates $\boldsymbol{M}_0$ to lie along the y

axis as shown Fig. 2.1(b). In our discussion we consider H_1 to be sufficiently strong that t_p is negligibly short. We designate the time just before or just after the pulses by using the signs "-" and "+", respectively. If there is no inhomogeneity in the static field, all spins within the sample would precess at γH_0, so the magnetization of every portion of the sample would remain oriented along the y axis. However, in practice, inhomogeneity exists and it leads to a spread in precession rates and dephasing, which correspondingly causes the free induction decay after the initial pulse (see Fig. 2.2). Consider a small portion of the sample with a local field deviation $\Delta H = H - H_0$ represented by a magnetization deviation $\delta \boldsymbol{M}$. The magnetization $\delta \boldsymbol{M}$ will remain in the x-y plane since we neglect T_1-processes. But at the end of a time interval τ, the direction of $\delta \boldsymbol{M}$ within that plane will advance from the y-direction by some angle θ given by

$$\theta = \gamma \Delta H \tau , \tag{2.27}$$

where ΔH represents the inhomogeneity of the static field. The situation is shown in Fig. 2.1(c). (Note that ΔH may be either positive or negative, so that the "advance in phase" may be either positive or negative.) Suppose now we apply a π pulse at $t = \tau$ using $\boldsymbol{H}_1 = H_1 \mathbf{i}$ again and adjust the pulse duration. The situation just after the π pulse is shown in Fig. 2.1(d). Noting the orientation of $\delta \boldsymbol{M}$, we immediately see that during a second time interval τ, $\delta \boldsymbol{M}$ will again advance through the same angle θ, which will bring it exactly along the negative y axis at $t = 2\tau$. The argument applies to all spins, no matter what ΔH they experience, because the result does not depend on the angle of advance.

Though all spins are in phase at $t = 2\tau$, they get out of phase again owing to the field inhomogeneity, so the free induction decays again. Note that its form as a function of time during the dephasing from $t = 2\tau$ onward must be identical to the form of the decay following the initial $\pi/2$ pulse (see Fig. 2.2). The buildup of the echo signal just prior to $t = 2\tau$ is the mirror image in time of the decay after $t = 2\tau$.

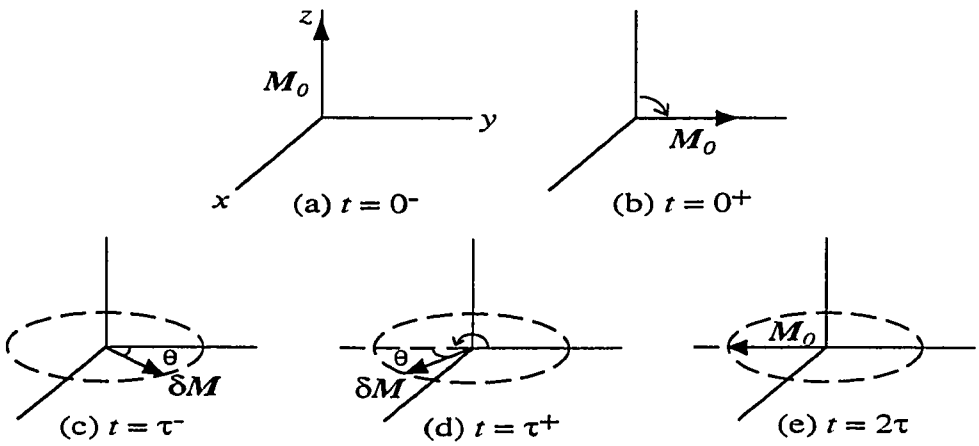

Fig. 2.1 The formation of a spin echo in a $(\pi/2)_x$ - τ - $(\pi)_{-x}$ pulse sequence in the rotating reference frame. M_0 is the magnetization in thermal equilibrium and δM is an element of magnetization. Note the M_0 rotated along $+y$ axis just after the $\pi/2$ pulse is reconstructed along $-y$ axis at $t = 2\tau$ (see the text for details).

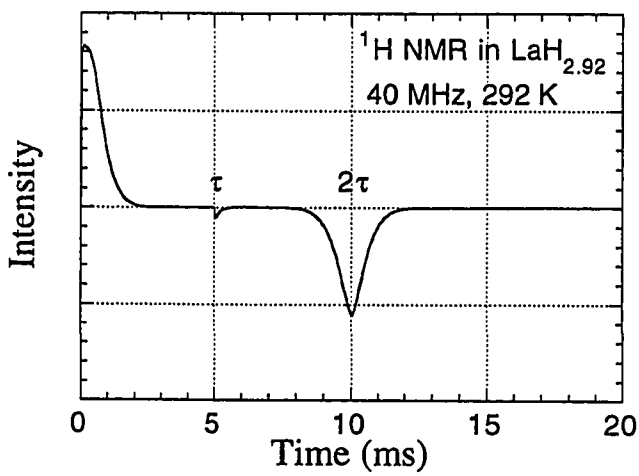

Fig. 2.2 Example of a FID and spin echo: ^{1}H NMR signal (absorption part only) in $LaH_{2.92}$ using a $(\pi/2)_x$ - τ - $(\pi)_{-x}$ pulse sequence. Inhomogeneous magnetic field was applied to obtain the fast decay of FID. The mark at $t = \tau$ indicates the 2nd pulse. Note the change of the sign from positive (for FID) to negative (for spin echo) as illustrated in Fig. 2.1.

2.2.2.3 NMR Spectrum and Knight Shift (K)

The plot of the response versus frequency (or equivalently magnetic field) is called a spectrum. The NMR spectrum can be obtained directly by sweeping external magnetic field in the original NMR technique, a so-called continuous wave (CW) NMR. In pulse NMR, however, the NMR signal obtained in the time domain is called the free induction decay (FID). The well-known Fourier transformation (FT) relates the representations in the two complementary domains. Specifically, the FT in NMR relates the signal in the time domain to the spectrum in the frequency domain. Thus, in pulse NMR, the spectrum is obtained by the FT of the FID or equivalently of half of the spin echo signal.

Pulse NMR has a great advantage over the CW NMR in view of its high resolution and the power of relaxation measurements. However, pulse NMR is limited for the case of broad spectra which, in practice, we meet quite often. Thus, in the case of a broad spectrum, a sort of combination of pulse and CW NMR techniques is applied to measure the spectrum. The simplest one is to record the amplitude of the FID or spin echo as a function of frequency (or field) by sweeping frequency (or field) in pulse NMR. Another way is to have spectra by FT processing at different frequencies and sum all the spectra. In order to increase resolution, it is recommended to simply increase the number of frequency points and to reduce the coverage of frequency range by using a narrow band pass filter and/or a small value of rf field (H_1) intensity. In this thesis we applied the former method to measure the large anisotropic spectrum of ^{199}Hg NMR in $HgBa_2CuO_{4+\delta}$, discussed in chapter 4, and the latter to measure the spectra of ^{35}Cl NMR in $Sr_2CuO_2Cl_2$ and ^{11}B NMR in YNi_2B_2C involving the satellites due to the first order quadrupole effects, discussed in chapters 3 and 4, respectively.

As discussed before, the Knight shift, K, is obtained by measuring the relative shift of the resonance-peak frequency with respect to the resonance frequency of a reference material when we obtain the NMR spectrum [see Eq. (2.13)]. The definition Eq. (2.13) is valid when the Knight shift is isotropic. In general, the Knight shift is a tensor and should be characterized by nine components which reduce to three in the diagonal reference frame. For tetragonal symmetry, which is the situation most commonly encountered in this thesis,

one can express the Knight shift tensor in terms of the two components: the isotropic (K_{iso}) and the axial component (K_{ax})

$$K_{iso} \equiv \frac{1}{3}(K_{\parallel} + K_{\perp}) ,$$
$$K_{ax} \equiv \frac{1}{3}(K_{\parallel} - K_{\perp}) , \tag{2.28}$$

where $K_{\parallel,\perp}$ represent the Knight shifts for the applied field parallel or perpendicular to the axially symmetric crystal axis, respectively. It is noted that the isotropic Knight shift, K_{iso}, gives the value of the powder-averaged Knight shift over the sample and the axial component, K_{ax}, gives information on the anisotropy of the Knight shift, whereby the total anisotropy is represented by $3K_{ax} \equiv K_{\parallel} - K_{\perp}$.

2.2.2.4 Spin-Spin Relaxation Time (T_2)

If one looks at Fig. 2.2 carefully, one can easily realize that the amplitude of the spin echo is less than that of the FID. This is due to T_2-process decay during the time 2τ. In fact, the spin-spin relaxation time is usually measured by monitoring the spin-echo amplitude decay in the ordinary two-pulse sequence, $\pi/2 - \tau - \pi$, with variable time interval τ. As we know, the ordinary spin-echo sequence refocuses the dephasings which arise from the inhomogeneous magnetic field. This is true even for the case that the local-field inhomogeneity comes from the dipolar coupling between different nuclear species. However, other spin interactions, i.e. the dipolar coupling between like nuclei produces an irreversible decay of the transverse magnetization. The second π pulse inverts all the like nuclei neighbors, so that a nucleus which was precessing more rapidly than average in the first time interval τ, finds its neighbors inverted, and thus precesses more slowly in the second interval. Therefore, the dipolar coupling between like nuclei is not refocused and its contribution to the dephasing of the spin precession is reflected in the decay of the spin-echo amplitude.

In addition, a local-field fluctuation in time can give rise to a decay of the spin-echo amplitude because the rephasing rate during the second interval τ may differ from the dephasing rate during the first interval τ due to the change of the local field. Diffusional motion in liquids is the typical case. Thus, as shown by Carr and Purcell [28], suppose the spin-echo decay due to the homonuclear dipolar interaction is an exponential with a characteristic time T_2. We can then write the decay of the total transverse magnetization for motional diffusion as a product of two contributions:

$$M(t = 2\tau) = \exp\left(-\frac{t}{T_2}\right)\exp\left[-\frac{\gamma^2 G^2 D}{12}t^3\right] \tag{2.29}$$

where G is the field gradient, assumed to be uniform, and D is the diffusion constant.

Now we briefly introduce an advanced pulse sequence using multiple pulses, the so-called Carr-Purcell-Meiboom-Gill sequence (CPMG) [29]. The CPMG sequence given by $(\pi/2)_x$ - τ - $[\pi_y$ - 2τ - π_y - 2τ - $]_n$ pulse sequence is well known to reduce, for $2\tau \rightarrow 0$, the contribution to the decay of the spin echo due to diffusion and allows one to separate the two contributions since the spin-echo decay in a multiple π pulse sequence becomes, at $t = 2n\tau$,

$$M(t = 2n\tau) = \exp\left(-\frac{t}{T_2}\right)\exp\left[-\frac{\gamma^2 G^2 D\tau^2}{3}t\right]. \tag{2.30}$$

On the other hand, the CPMG sequence was found to generate important spin-locking effects in solids and the spin-locking effects turned out be detrimental to the analysis of the decay mechanisms [30]. In order to circumvent the problem of spin locking we have devised a modified sequence with alternating phases of the y pulse in the CPMG sequence, the so-called AP-CPMG sequence. The AP-CPMG sequence was applied for the study of

flux motion in $YBa_2Cu_3O_7$ from ^{89}Y spin-spin relaxation measurements [31], discussed in chapter 5 and detailed discussions of the AP-CPMG sequence appear in Ref. [30].

2.2.2.5 Spin-Lattice Relaxation Time (T_1)

The spin-lattice relaxation time, T_1, can be simply obtained by measuring the characteristic time of the recovery of the longitudinal nuclear magnetization towards equilibrium after inverting the magnetization with a π pulse. At a time t after the inversion, a $\pi/2$ pulse (or a spin-echo sequence) is applied to monitor the recovered value of the magnetization. For the case of exponential recovery, the recovery curve is given by

$$M_z(t) = M_\infty\left[1-2\exp\left(-\frac{t}{T_1}\right)\right], \tag{2.31}$$

where M_∞ is the value of the longitudinal magnetization at equilibrium. This method is called the "inversion recovery" method. Another common method of T_1 measurement is the so-called "saturation comb" method where a series of $\pi/2$ pulses (a saturation comb) is applied to set the magnetization to zero. The recovery curve in this method is given by

$$M_z(t) = M_\infty\left[1-\exp\left(-\frac{t}{T_1}\right)\right]. \tag{2.32}$$

Since it is not necessary to wait until equilibrium is restored, the saturation method is faster than the inversion recovery method. On the other hand, the saturation method gives a less accurate T_1 than the inversion recovery method since only half of the full recovery curve is used to fit the data.

The single exponential recovery law in the above is for the simplest case with spin I = 1/2. For spin $I > 1/2$ the recovery of the magnetization is not generally exponential since the transitions are not simply between only two levels and the energy level spacing is not

equivalent due to the quadrupolar modification of the Zeeman levels. The recovery law can be derived quite generally by solving the so-called "master equation" [32] and is strongly dependent on the relaxation mechanism and on the initial saturation conditions. The relaxation mechanism can be of magnetic origin (magnetic hyperfine interaction) or of electric origin (electric quadrupole interaction). We will here consider only the NSLR due to the magnetic interaction which can be characterized by a single parameter W, the relaxation transition probability corresponding to the transitions for $\Delta m = \pm 1$. We now consider two ways to selectively irradiate only the central line: (i) A sequence of a saturating pulses is applied for a short duration $\tau << T_1$. In this case, the populations of the $m = \pm 1/2$ levels are saturated but the pulses are not applied long enough to allow the satellite level populations to come to equilibrium with the populations in the $m = \pm 1/2$ levels. (ii) The saturating pulses are applied for a time $\tau >> T_1$ long enough to allow lattice relaxation to bring the satellite levels into equilibrium with the $m = \pm 1/2$ levels. For $I =$ 3/2 the resultant expressions of the recovery law of the central line ($1/2 \leftrightarrow -1/2$) are given below for the two conditions described above and for magnetic relaxation:

$$\text{(i)} \quad \frac{M_\infty - M(t)}{M_\infty} = 0.1 \cdot \exp(-2Wt) + 0.9 \cdot \exp(-12Wt)\,, \tag{2.33a}$$

$$\text{(ii)} \quad \frac{M_\infty - M(t)}{M_\infty} = 0.4 \cdot \exp(-2Wt) + 0.6 \cdot \exp(-12Wt)\,. \tag{2.33b}$$

When the central line is narrow and the satellites are well apart in frequency from the central line, the condition (i) can be easily achieved with a single saturating pulse. It is noted that the single exponential recovery can be obtained even for $I > 1/2$ if one saturates whole spectrum including satellites and the relaxation mechanism is due to magnetic interaction.

In this work, for both the ^{35}Cl ($I = 3/2$) and the ^{11}B ($I = 3/2$) NSLR measurements, discussed in chapters 3 and 4 respectively, we saturated the central line with a single pulse.

For ^{11}B NSLR, $2W$, the data are found to fit the recovery law (2.33a) since the satellites are well apart from the central line in the whole temperature range investigated. However, for ^{35}Cl NSLR, $2W$, the data do not fit to Eq. (2.33a). This is not surprising because the line width of the ^{35}Cl NMR in $Sr_2CuO_2Cl_2$, in particular for $\boldsymbol{H} \perp \boldsymbol{c}$, increases with decreasing temperature, correspondingly the satellites overlap with the central line near the Néel temperature T_N (see chapter 3 for details). In this case, the recovery is usually in between the two cases (2.33a) and (2.33b), and is expressed as below with additional fitting parameters to decide the proportion of each term:

$$\frac{M_\infty - M(t)}{M_\infty} = C_1 \exp(-2Wt) + C_2 \exp(-12Wt) \; . \tag{2.34}$$

The ^{35}Cl NSLR, $2W$, in chapter 3 were obtained by using the Eq. (2.34).

3. NMR AS A PROBE TO STUDY SPIN DYNAMICS AND CORRELATIONS

We present a typical microscopic NMR investigation of spin dynamics and correlations in an undoped high-T_c cuprate parent compound.

3.1 Spin Dynamics and Correlations in the Quasi-2D Antiferromagnet $Sr_2CuO_2Cl_2$ from ^{35}Cl NMR in Single Crystals

3.1.1 Introduction

The undoped layered perovskite system $Sr_2CuO_2Cl_2$ has attracted attention due to the possibility of clarifying the properties of the spin $S = 1/2$ two-dimensional (2D) square-lattice Heisenberg antiferromagnet (2DSLHA), and therefore perhaps of the doped high-T_c superconductors. The structural and magnetic properties of $Sr_2CuO_2Cl_2$, investigated by x-ray diffraction, neutron scattering, magnetic susceptibility and muon spin rotation [33-35], were found to be similar to those of La_2CuO_4. However, an important difference is that the structure of $Sr_2CuO_2Cl_2$ remains tetragonal down to at least 10 K [33,34]. This lack of an orthorhombic distortion, such as occurs in La_2CuO_4 below 530 K, eliminates [34] the relatively large Dzyaloshinskii-Moriya anisotropy term in the spin Hamiltonian which is responsible for the canted moment in the antiferromagnetic (AF) state of La_2CuO_4 below its Néel temperature $T_N = 325$ K [36,37]. This in turn allows the effects of much weaker

anisotropies such as the planar XY and the intraplanar anisotropies intrinsic to weakly coupled undistorted CuO_2 planes to be more clearly identified in $Sr_2CuO_2Cl_2$. The combination of neutron scattering studies, numerical simulations, and theories on e.g. Pr_2CuO_4, Nd_2CuO_4 and especially La_2CuO_4 has contributed to form a coherent picture of the low temperature properties of the $S = 1/2$ 2DSLHA [36-41]. Recently the same combination of experiments and theory was applied [42] to $Sr_2CuO_2Cl_2$, with $T_N = 256.5 \pm 1.5$ K in zero magnetic field, which is an even better $S = 1/2$ 2DSLHA model system [34-37]. The instantaneous 2D spin-spin correlation length, $\xi(T)$, was accurately determined over a wide temperature range above T_N and compared with theories and Monte Carlo simulations. Good agreement was found with no evidence of crossover effects in $\xi(T)$ upon cooling towards T_N in spite of the small but non-negligible XY anisotropy given by $J^{XY}/J = 1.4\times10^{-4}$, where the Cu-Cu intraplanar AF exchange constant $J = 1450$ K [42]. The absence of crossover effects is surprising since $\xi(300\text{ K})$ is already over 100 times the Cu-Cu distance a in the CuO_2 plane [42] and one expects that a very small XY anisotropy should induce a crossover from 2D Heisenberg to 2D XY-like spin behavior for $T \rightarrow T_N^+$ [38-42]. Crossover effects have been suggested but not clearly resolved from experiments on La_2CuO_4 above T_N [38,43]. Furthermore, the application of a strong magnetic field should introduce further anisotropic behavior. Preliminary results of ^{35}Cl nuclear magnetic resonance (NMR) in powder and single crystal samples of $Sr_2CuO_2Cl_2$ suggested the occurrence of crossover effects [20] and field-induced effects [44], respectively.

In this chapter we report extensive ^{35}Cl NMR and static magnetization investigations on good quality single crystals of $Sr_2CuO_2Cl_2$ aimed at exploring the effects of both the planar anisotropy and the magnetic field (H) induced anisotropy on the correlated spin dynamics and on T_N of the Cu^{2+} spins. For $\boldsymbol{H} \parallel \boldsymbol{c}$ the primary [45] XY symmetry of the Cu^{2+} spins in the CuO_2 (ab) plane is preserved and the ^{35}Cl nuclear spin-lattice relaxation rate (NSLR) is proportional to the spectral density of the fluctuations of the Cu^{2+} spin components in the ab plane, while for $\boldsymbol{H} \perp \boldsymbol{c}$ the ^{35}Cl NSLR contains terms proportional to

the fluctuations of the Cu^{2+} spins out of the *ab* plane. From the enhancement of the NSLR as $T \rightarrow T_N^+$ and from its anisotropy, we find evidence for Heisenberg to *XY*-like crossover behavior. The crossover effects are supported with additional evidence obtained from the measurements of ^{35}Cl spin-spin relaxation rate, T_2^{-1}. Furthermore, for $\boldsymbol{H} \perp \boldsymbol{c}$ we measured a Néel temperature which increases from the zero-field value of $T_N = 257.0 \pm 0.5$ K to $T_N = 265.3 \pm 1.0$ K for $H = 8.2$ T. This effect can be explained in terms of an anisotropy induced by the applied field $\boldsymbol{H}$. In fact, the direction of $\boldsymbol{H}$ in the *ab* plane becomes a hard axis and thus the combination of the *XY* anisotropy, J^{XY}, and $\boldsymbol{H}$ drives the spin system towards an easy axis anisotropy. This effect is qualitatively similar to the field-induced anisotropies widely studied in other 2D antiferromagnets [46]. We present the data for the anisotropic broadening and shift of the ^{35}Cl NMR lines occurring above T_N which seem to indicate the presence of field-induced two dimensional short range ordering above T_N.

3.1.2 Experimental Details

Single crystal samples of $Sr_2CuO_2Cl_2$ were prepared at Ames Laboratory by L. L. Miller using the method described in detail elsewhere [33]. The ^{35}Cl NMR measurements were carried out in stack of $Sr_2CuO_2Cl_2$ single crystals with approximate volume $7 \times 4 \times 1$ mm^3. The ^{35}Cl line width, paramagnetic shift, NSLR, and T_2^{-1} were measured in the temperature range 230 to 400 K for the central line transition at 4.7 and 8.2 Tesla. The ^{35}Cl ($I = 3/2$) NMR spectrum at 4.7 Tesla displays a narrow central line with negligible second order quadrupole effects and two satellite transitions as shown in Fig. 3.1. The sharpness of the spectrum indicates that the "mosaic" spread of the stack is very small. From the rotation pattern we find a quadrupole frequency $\nu_Q \equiv qQe^2/2h = (242 \pm 5)$ kHz at $T = 293$ K. The shift of the central line was measured with respect to NaCl aqueous solution. The spin-lattice relaxation rate (NSLR, $2W$) was obtained from the fit of the recovery of the

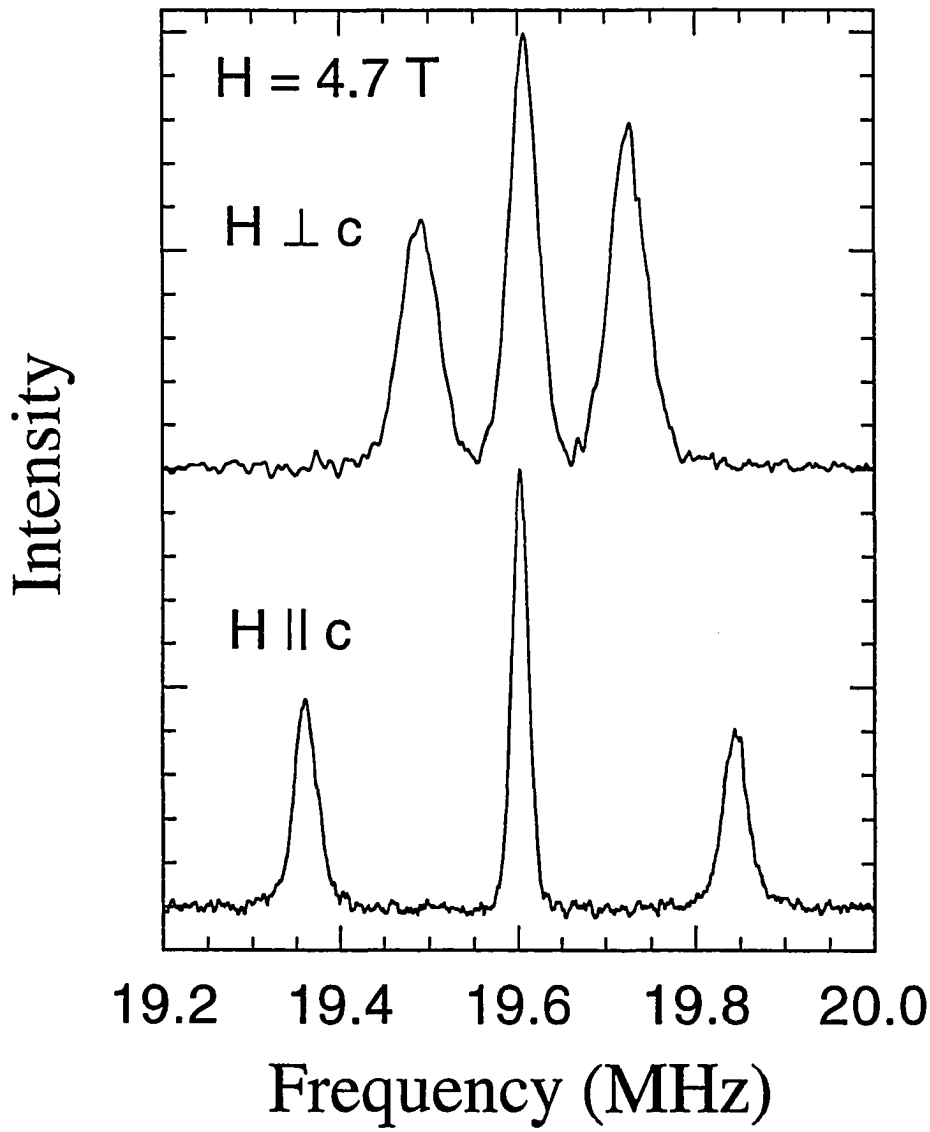

Fig. 3.1 ^{35}Cl NMR spectra in stacked $Sr_2CuO_2Cl_2$ single crystals for $H = 4.7$ Tesla and for two orientations of the external field with respect to the crystal c axis: $\boldsymbol{H} \parallel \boldsymbol{c}$ and $\boldsymbol{H} \perp \boldsymbol{c}$.

nuclear magnetization of the central line after saturation with a single $\pi/2$ pulse to the expression [see Eq. (2.34)]:

$$\frac{M(\infty) - M(t)}{M(\infty)} = C_1 \exp(-2Wt) + C_2 \exp(-12Wt) \, . \tag{3.1}$$

In order to measure T_2^{-1}, the decay of the spin-echo signal was measured as a function of separation τ between two radio frequency (rf) pulses in an ordinary pulse sequence, $(\pi/2)_x$ - τ - $(\pi)_y$. The shape of the spin-echo decay was not a simple form such as a single exponential or a single Gaussian but could be fit by the product of two functions, an exponential and a Gaussian:

$$M(t = 2\tau) = M(0) \exp\left(-\frac{t}{T_L}\right) \exp\left[-\left(\frac{t}{T_G}\right)^2\right] . \tag{3.2}$$

Magnetization (M) measurements were carried out (at Ames Laboratory by L. L. Miller) up to a maximum field $H = 5.5$ T on a stack of four single crystal plates with a total mass of 294 mg, with their c axes aligned as for the NMR measurements, using a Quantum Design SQUID magnetometer. The effect of a lack of orientational order in the ab plane on the NMR and M results, which could conceivably affect the data for $T \leq T_N$, was not investigated. Below $H \sim 0.3$ Tesla, the $M(H)$ isotherm data (not shown) exhibited negative curvature, tentatively attributed to ferromagnetic impurities and equivalent to ≈ 15 at. ppm of iron metal impurities with respect to Cu; the susceptibility data presented later are corrected for this contribution.

3.1.3 Experimental Results

The results for the temperature dependence of the ^{35}Cl line shift and width are shown in Figs. 3.2 and 3.3, respectively for two magnetic field intensities and two orientations. The measurements for $\boldsymbol{H} \perp \boldsymbol{c}$ are not reported for $T < T_N$ since the ^{35}Cl resonance line becomes very broad. For $\boldsymbol{H} \perp \boldsymbol{c}$, we observed the onset of a broadening and a shift (not observed for $\boldsymbol{H} \parallel \boldsymbol{c}$) of the ^{35}Cl NMR line for $T < 320$ K, in agreement with the previous report [44]. The results of ^{35}Cl NSLR, $2W$, measurements are shown in Fig. 3.4. The maxima of $2W(T)$ occur at T_N. A prominent feature of the data in Fig. 3.4 is the sizable field dependence of T_N when the field is applied in the *ab* plane, whereas to within our resolution ($\pm$ 0.5 K) T_N is independent of H for $\boldsymbol{H} \parallel \boldsymbol{c}$. The results for the temperature dependence of the exponential component, T_L^{-1}, and of the Gaussian component, T_G^{-1}, of the spin-echo decay due to spin-spin relaxation are shown in Figs. 3.5(a) and (b) respectively.

Magnetic susceptibility (χ) data corrected for the diamagnetic core contribution are shown in Fig. 3.6 for both $\boldsymbol{H} \parallel \boldsymbol{c}$ ($\chi_{\parallel}$) and $\boldsymbol{H} \perp \boldsymbol{c}$ ($\chi_{\perp}$). Our $\chi_{\perp}(T)$ data exhibit a clear, sharp field-dependent cusp, the peak of which we assume to be at T_N. The field dependence of T_N for $\boldsymbol{H} \perp \boldsymbol{c}$ is shown in Fig. 3.7. To within our precision, the $\chi_{\perp}(T)$ and ^{35}Cl NMR measurements yield the same $T_N(H)$ dependence for $\boldsymbol{H} \perp \boldsymbol{c}$. Similar to previous results [34], no obvious anomaly in $\chi_{\parallel}(T)$ is seen at $T_N \sim 260$ K; rather, $\chi_{\parallel}(T)$ appears to show only a smooth minimum at $T_{cr} \approx 300$ K. However, examination of the temperature derivative of these $\chi_{\parallel}(T)$ and additional data at other fields reveals a local minimum in slope at T_N for each data set, which is found to be qualitatively field-independent, consistent with our NMR results.

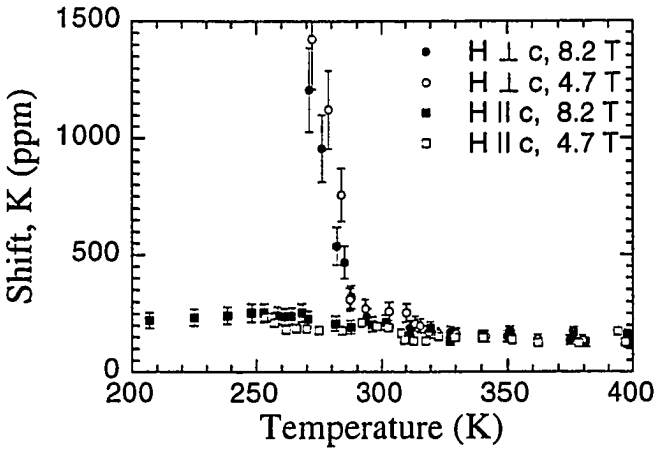

Fig. 3.2 ^{35}Cl NMR shift, K, vs temperature in stacked $Sr_2CuO_2Cl_2$ single crystals for two intensities and two orientations of the external magnetic field H.

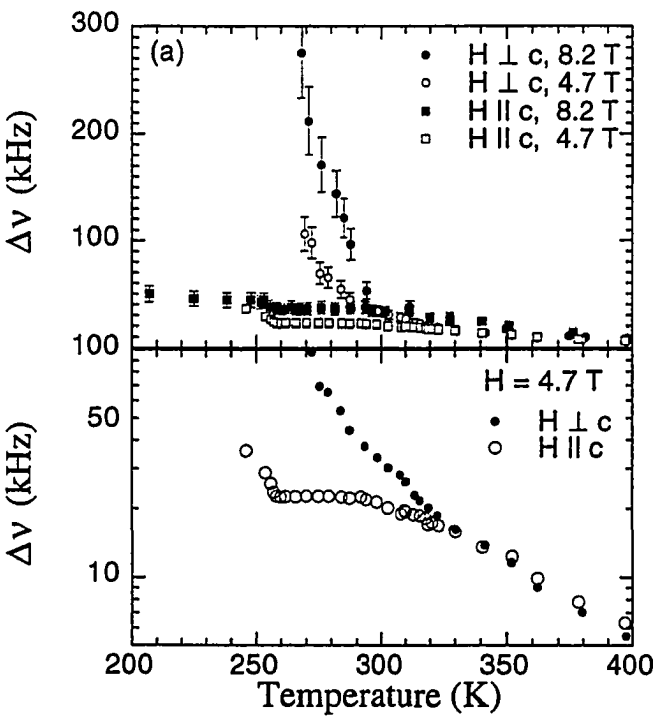

Fig. 3.3 ^{35}Cl NMR linewidth, $\Delta\nu$, vs T in stacked $Sr_2CuO_2Cl_2$ single crystals: (a) Linear-scale plot of $\Delta\nu$ for two magnetic field intensities. (b) Semi-log plot of $\Delta\nu$ for $H = 4.7$ T.

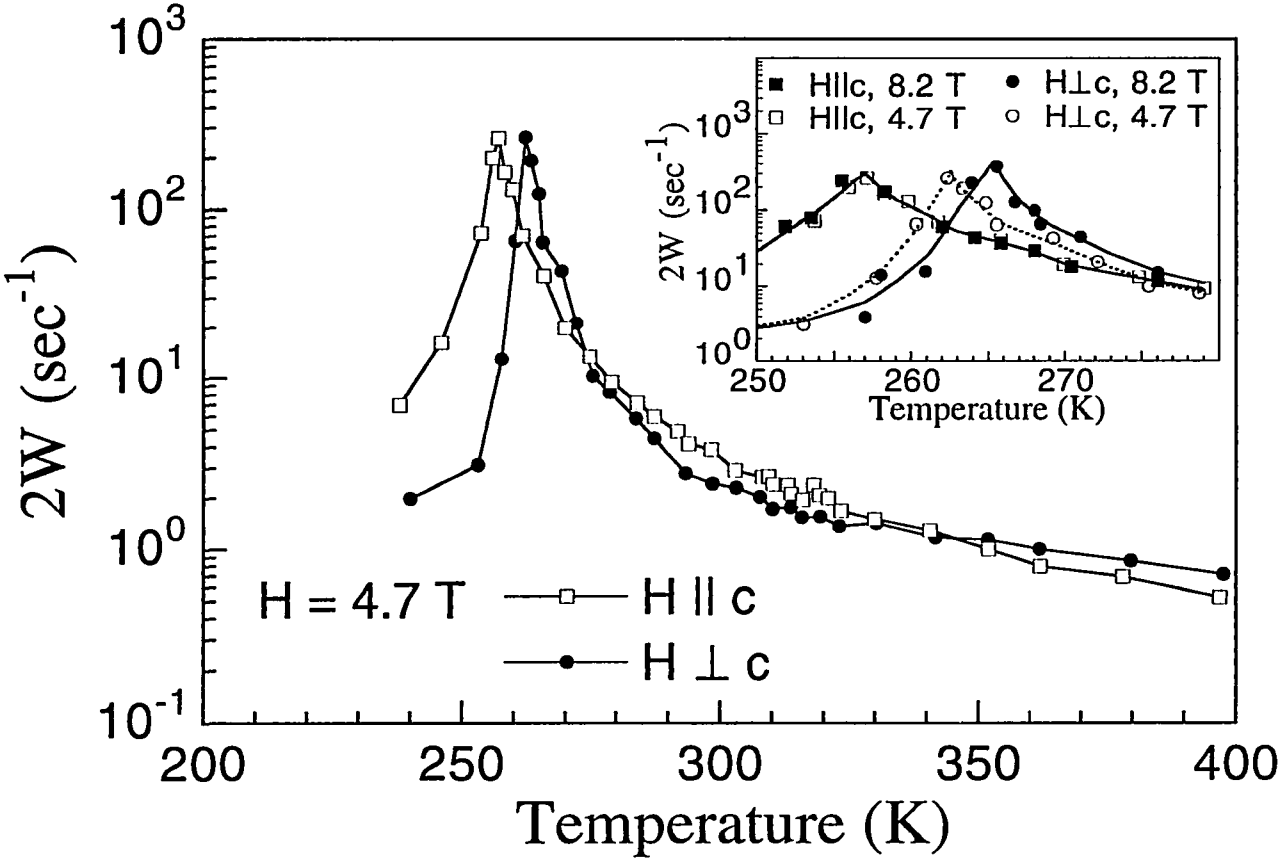

Fig. 3.4 ^{35}Cl NSLR, $2W$, vs T in stacked $Sr_2CuO_2Cl_2$ single crystals for $H = 4.7$ T. The maximum of $2W$ occurs at T_N. The inset shows expanded plots of data near T_N for $H = 4.7$ T and 8.2 T.

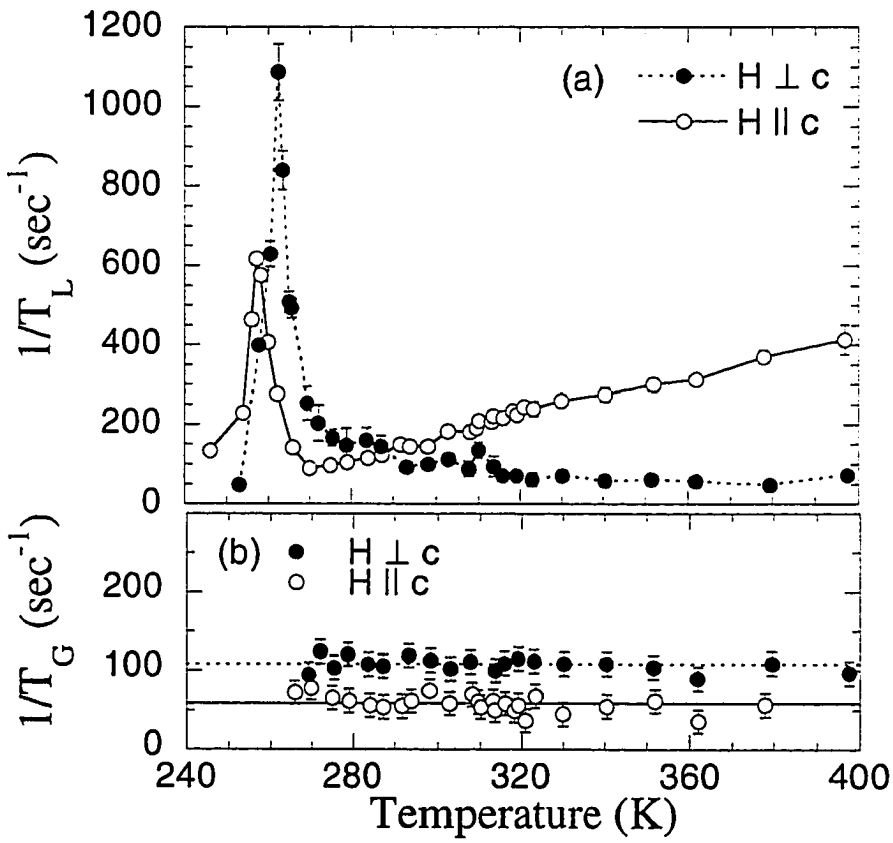

Fig. 3.5 Plots of the ^{35}Cl nuclear spin-spin relaxation rate components in $Sr_2CuO_2Cl_2$ single crystals for $H = 4.7$ T: (a) The exponential component (T_L^{-1}) vs T. The curves are only guides for the eye. (b) The Gaussian component (T_G^{-1}) vs T. The lines are the average values of T_G^{-1}; dashed line, $(T_G^{-1})_\perp = 107$ sec^{-1}, and solid line, $(T_G^{-1})_\parallel = 58$ sec^{-1}.

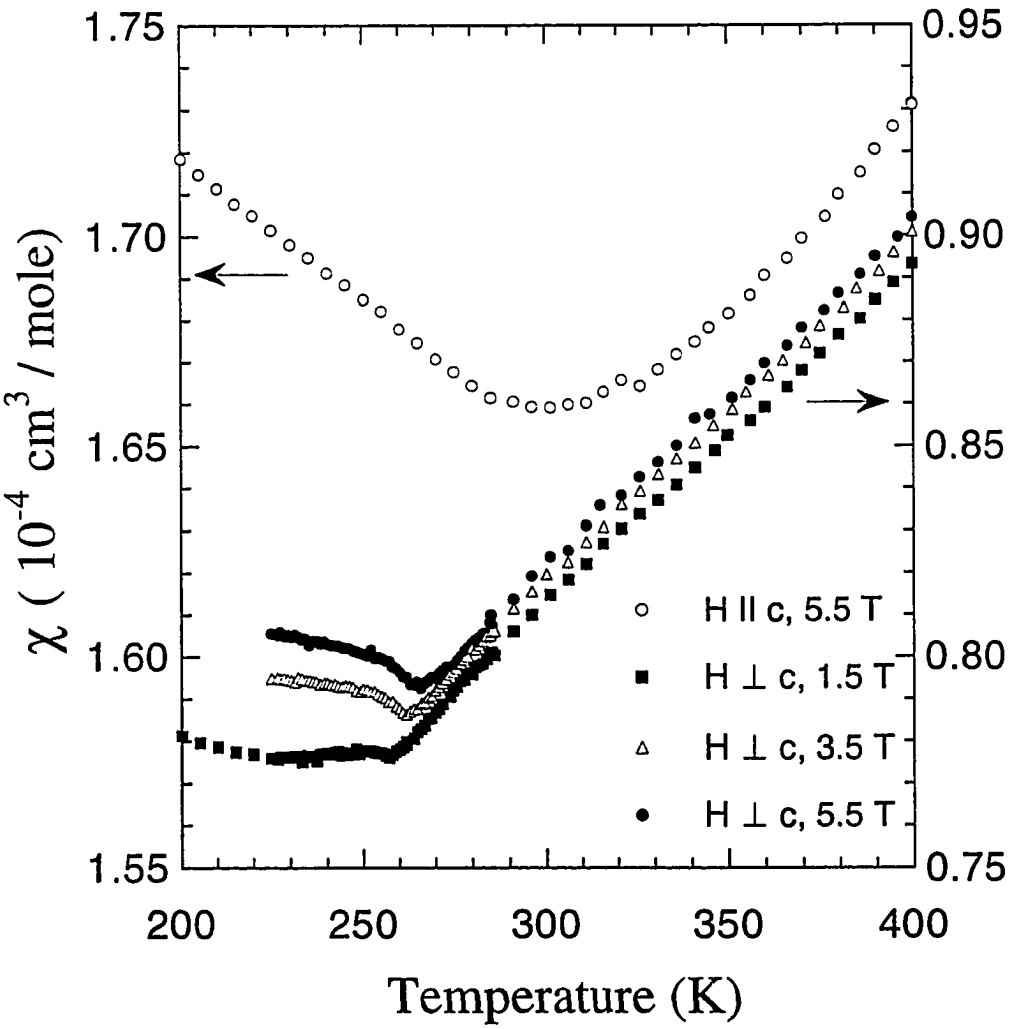

Fig. 3.6 Plots of magnetic susceptibility, χ, in $Sr_2CuO_2Cl_2$ single crystals. The data are corrected for the ion core diamagnetism. Note the two (expanded) linear scales. (Courtesy of L. L. Miller)

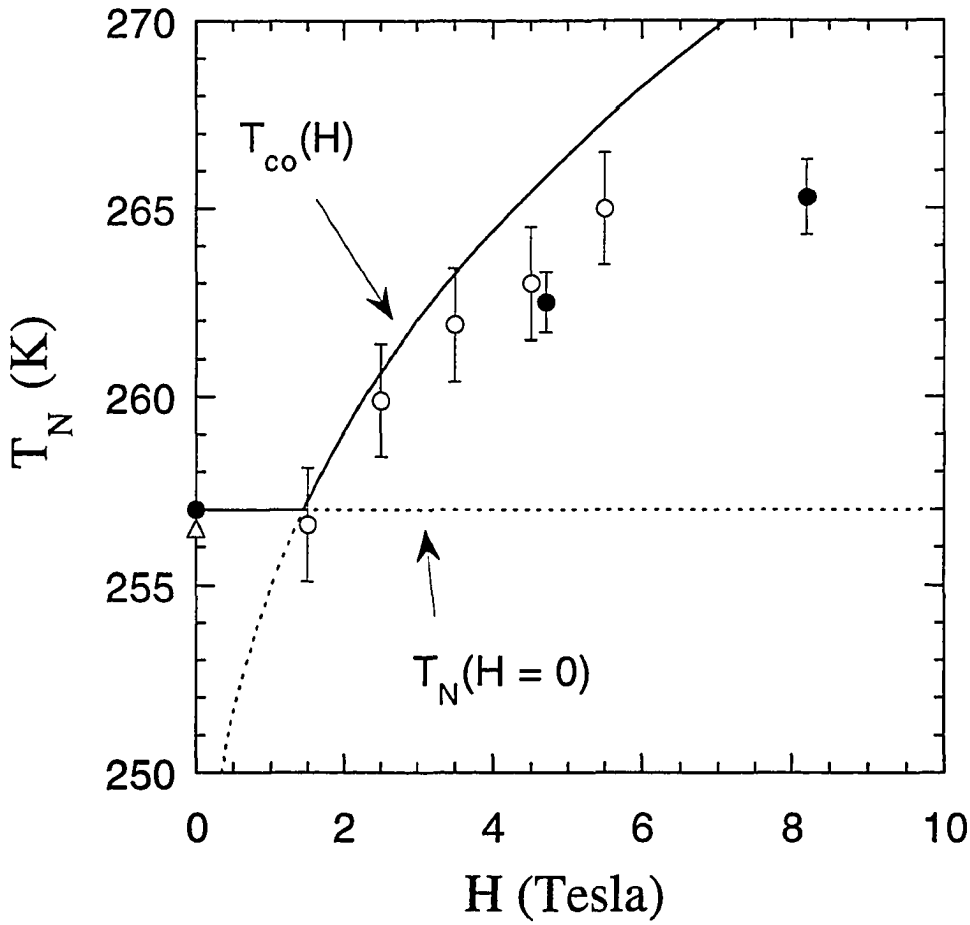

Fig. 3.7 Magnetic field effects on T_N, for $\boldsymbol{H} \perp \boldsymbol{c}$: (•) from NMR, and (o) from magnetic susceptibility. The solid line is the combination of $T_N(H = 0)$ held constant up to $H_{co} = 1.4$ T and the $T_{co}(H)$ calculated from Eq. (3.9) in the text. The $T_N(H = 0)$ is from (Δ) zero field neutron scattering [42], and (•) ^{35}Cl NMR for $\boldsymbol{H} \parallel \boldsymbol{c}$ ($H = 4.7$ T and 8.2 T) which should correspond to $T_N(H = 0)$.

3.1.4 Discussion

3.1.4.1 Spin-Lattice Relaxation and Spin Dynamics

Before analyzing the above $T_N(H)$ data, we look at the critical spin dynamics as manifested by the enhancement of $2W$ for $T \rightarrow T_N^+$. From the small value of the paramagnetic shift, we can infer that the contact hyperfine interaction, $\boldsymbol{AS}\cdot\boldsymbol{I}$, at the ^{35}Cl site is small, possibly of the same magnitude as the dipolar interaction [44]. The first nearest neighbor Cu^{2+} magnetic moment at distance d along the c axis yields a dipolar field which differs at most by 15% from the total dipolar field for AF correlated spins [44]. For the contact term, only the first neighbor contributes. Thus we can write for the local hyperfine field at the ^{35}Cl site

$$\vec{h} = \vec{h}_{dip} + \vec{h}_{contact} = \frac{1}{d^3}(-\mu_a\hat{a} - \mu_b\hat{b} + 2\mu_c\hat{c}) + A(\mu_a\hat{a} + \mu_b\hat{b} + \mu_c\hat{c}), \tag{3.3}$$

where $\hat{a}$, $\hat{b}$ and $\hat{c}$ are the unit vectors of the crystal axes reference frame and $\mu_{a,b,c}$ are the instantaneous components of a Cu^{2+} nearest neighbor magnetic moment to a given ^{35}Cl nucleus. The general expression for the NSLR obtained from time dependent perturbation theory and in the weak collision approximation [see Eq. (2.14)] is:

$$2W = \frac{1}{2}\gamma^2 \int_{-\infty}^{+\infty} < h_+(t)\cdot h_-(0) > e^{i\omega_L t} dt \tag{3.4}$$

where $\omega_L = \gamma H$ is the Larmor frequency. Since the two local hyperfine fields in Eq. (3.3) are uncorrelated [2], we derive from Eqs. (3.3) and (3.4):

$$2W_{\parallel} = \frac{\gamma^2}{2d^6}\cdot\{2J_{\perp}(\omega_L)\} + \frac{\gamma^2 A^2}{2}\cdot\{2J_{\perp}(\omega_L)\} \qquad (\boldsymbol{H} \parallel \boldsymbol{c}),$$
$$2W_{\perp} = \frac{\gamma^2}{2d^6}\cdot\{J_{\perp}(\omega_L) + 4J_{\parallel}(\omega_L)\} + \frac{\gamma^2 A^2}{2}\cdot\{J_{\perp}(\omega_L) + J_{\parallel}(\omega_L)\} \qquad (\boldsymbol{H} \perp \boldsymbol{c}), \tag{3.5}$$

where $J_{\perp}(\omega_L) \equiv J_{aa}(\omega_L) = J_{bb}(\omega_L)$, $J_{\parallel}(\omega_L) \equiv J_{cc}(\omega_L)$ and $J_{\alpha\beta}(\omega_L) \approx J_{\alpha\beta}(0)$ $= \int < \mu_{\alpha}(t)\mu_{\beta}(0) > dt$ are the spectral densities of the fluctuations of the Cu^{2+} magnetic moment components, $\mu_{\alpha,\beta}$.

The important point apparent from Eqs. (3.5) is that the measurement of the ^{35}Cl NSLR for different orientations of the external magnetic field allows one to gain direct information about the symmetry of the fluctuations. In Fig. 3.8 we plot as a function of temperature the quantity:

$$\frac{2\cdot 2W_{\perp} - 2W_{\parallel}}{2W_{\parallel}} = C\frac{J_{\parallel}(\omega_L)}{J_{\perp}(\omega_L)}, \tag{3.6}$$

where the proportionality constant C is of order unity and depends on the relative strength of the dipolar to contact hyperfine interactions. The fact that $C\,J_{\parallel}(\omega_L)/J_{\perp}(\omega_L)$ strongly decreases with decreasing temperature as $T \rightarrow T_N^+$ is a strong indication that the fluctuations of the out-of-plane components of the Cu^{2+} spins [i.e. $J_{\parallel}(\omega \approx 0)$] are strongly suppressed on approaching T_N from above. In other words, *the Cu^{2+} spin system crosses over from Heisenberg to XY-like behavior upon cooling towards T_N*. This interpretation is consistent with the $\chi(T)$ data in Fig. 3.6(b). From quantum Monte Carlo calculations [47], a Heisenberg to *XY*-like crossover is expected to increase $\chi_{\parallel}$, resulting in a broad minimum [48], but should not appreciably affect $\chi_{\perp}$ compared with the 2D Heisenberg behavior which decreases monotonically with decreasing T in our temperature range. Above $T_{cr} \sim$

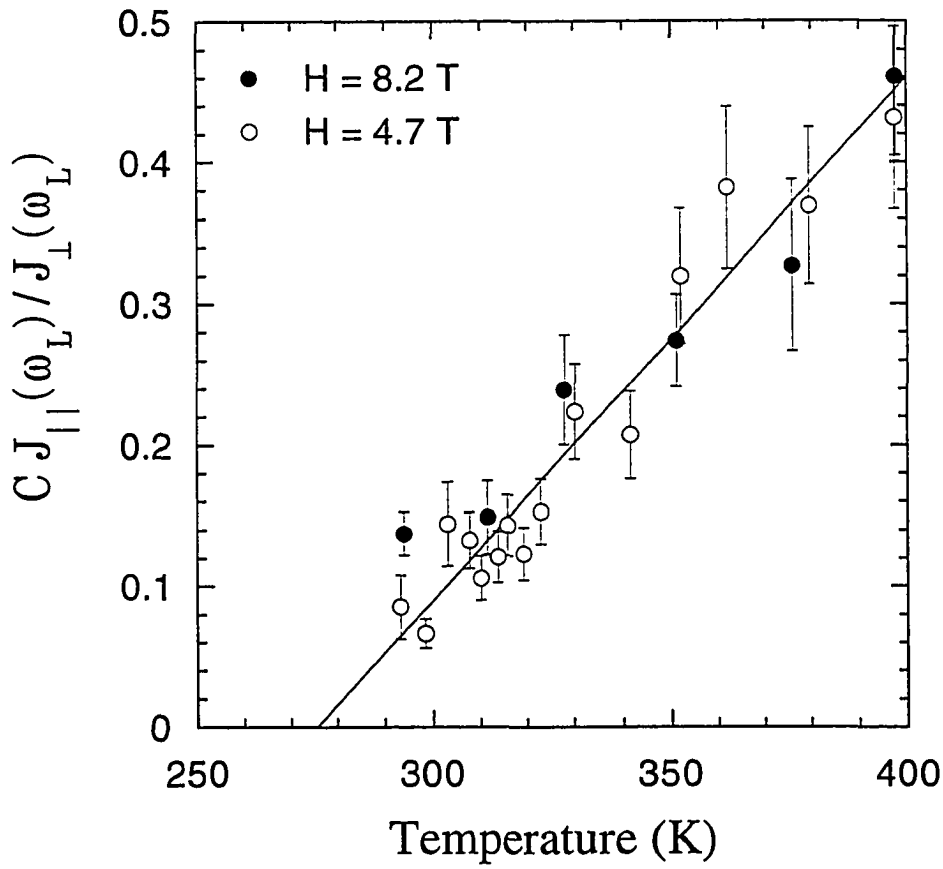

Fig. 3.8 Temperature dependence of the ratio of the spectral densities, $CJ_{\|}(\omega_L)/J_{\perp}(\omega_L)$, as obtained from the combination of ^{35}Cl $2W_{\|}$ (for $\boldsymbol{H} \| \boldsymbol{c}$) and $2W_{\perp}$(for $\boldsymbol{H} \perp \boldsymbol{c}$) [see Eq. (3.6)].

300 K, both $\chi_{\|}$ and $\chi_{\perp}$ increase with T as expected for an $S = 1/2$ 2DSLHA with $J \sim 1500$ K, due to the progressive loss of short-range AF correlations (decreasing ξ [42]) [36,37].

3.1.4.2 Spin-Spin Relaxation and Spin Dynamics

Now we discuss the observed unconventional anisotropy and strong temperature dependence of ^{35}Cl T_2^{-1} shown in Fig. 3.5. First, as can be seen from Fig. 3.5(b), the Gaussian contribution, T_G^{-1}, to the spin-spin relaxation rate is anisotropic and practically temperature independent. An approximate calculation of the Van Vleck second moment [Eq. (2.6)] due to homonuclear ^{35}Cl nuclear dipolar interaction yields $T_2^{-1} = (<\Delta\nu^2>/2)^{1/2} =$ 43 sec^{-1} for $\boldsymbol{H} \| \boldsymbol{c}$ and $T_2^{-1} = 63$ sec^{-1} for $\boldsymbol{H} \perp \boldsymbol{c}$ in the case of a simple Gaussian shape of the spin-echo decay. The calculated values agree both in magnitude and in sign of the anisotropy with T_G^{-1}, our experimental results. We conclude that the temperature independent Gaussian component of the spin-echo decay is due to nuclear dipolar interaction. On the other hand, the exponential component of the spin-echo decay, T_L^{-1}, [see Fig. 3.5(a)] is indicative of a contribution due to the ^{35}Cl nucleus - Cu^{2+} electron spin interaction modulated by the fast Cu^{2+} spin dynamics and thus can give information on crossover effects. This kind of T_2^{-1} is obtained from a time dependent perturbation theory [2,3,21] as:

$$\frac{1}{T_L} = \frac{1}{T_2} = \frac{1}{2}\gamma^2 \int \langle h_z(t) \cdot h_z(0) \rangle dt + \frac{1}{2T_1} \tag{3.7}$$

where $h_z(t)$ is the component of the local field parallel to $\boldsymbol{H}$ at the ^{35}Cl site due to the Cu^{2+} magnetic moments. As it was discussed in the above the dominant contribution to the ^{35}Cl hyperfine interaction comes from the dipolar and/or contact interaction of the ^{35}Cl nucleus with the first neighbor Cu^{2+} magnetic moment. By combining Eqs. (3.3) and (3.7) one has

$$\left(\frac{1}{T_L}\right)_{\parallel} = \left(\frac{1}{2T_1}\right)_{\parallel} + \frac{\gamma^2}{2d^6}\cdot 4J_{\parallel}(0) + \frac{\gamma^2 A^2}{2}J_{\parallel}(0) \qquad (\boldsymbol{H} \parallel \boldsymbol{c}),$$
$$\left(\frac{1}{T_L}\right)_{\perp} = \left(\frac{1}{2T_1}\right)_{\perp} + \frac{\gamma^2}{2d^6}\cdot J_{\perp}(0) + \frac{\gamma^2 A^2}{2}J_{\perp}(0) \qquad (\boldsymbol{H} \perp \boldsymbol{c}). \tag{3.8}$$

Comparing the data in Fig. 3.5 with the values of $T_1^{-1} = 2W$ in Fig. 3.4 one has $T_L^{-1} >> T_1^{-1}$ above T_N which implies $J_{\alpha\beta}(0) >> J_{\alpha\beta}(\omega_L)$. Thus, by neglecting the first term in Eq. (3.8), one has $(T_L^{-1})_{\parallel} = (4\gamma^2/2d^6 + \gamma^2A^2/2)J_{\parallel}(0)$ and $(T_L^{-1})_{\perp} = (\gamma^2/2d^6 + \gamma^2A^2/2)J_{\perp}(0)$. Figure 3.9 shows the direct ratio $(T_L^{-1})_{\parallel}/(T_L^{-1})_{\perp}$ vs temperature. The saturating value of the ratio $(T_L^{-1})_{\parallel}/(T_L^{-1})_{\perp} \cong 5.5 \pm 1$ well above T_N is consistent with Eq. (3.8) for a relatively small contact hyperfine interaction A. As $T \rightarrow T_N^+$, $(T_L^{-1})_{\parallel}$ decreases in agreement with what is expected if the longitudinal out-of-plane fluctuations, $J_{\parallel}(\omega \cong 0)$, are progressively suppressed with decreasing temperature [see Figs. 3.5(a) and 3.9]. We conclude, consistent with the conclusion inferred from NSLR measurements, that the Cu^{2+} spin system crosses over from Heisenberg to XY-like behavior upon cooling towards T_N. Very close to T_N the NSLR is strongly enhanced. Thus the first term in Eq. (3.8) is no longer negligible and $(T_L^{-1})_{\parallel,\perp}$ are also enhanced. The fact that $T_L^{-1} >> T_1^{-1}$ [i.e. $J_{\alpha\beta}(0) >> J_{\alpha\beta}(\omega_L)$] well above T_N probably contains important information about the type of correlated spin-order in the system but it cannot be presently understood. One could speculate that very low frequency modes are present contributing to T_L^{-1} but not to T_1^{-1} or that the critical modes in this low-dimensional system have a diffusive character with consequent logarithmic divergence of the spectral density as $\omega \rightarrow 0$ [49].

3.1.4.3 Critical Behavior of Spin Dynamics and Crossover Effects

The critical enhancement of the NSLR for $\boldsymbol{H} \parallel \boldsymbol{c}$, $2W_{\parallel}$, is proportional to $J_{\perp}(\omega \approx 0)$. Since the correlation length ξ extends over more than 30 lattice spacings in the temperature range investigated, the NSLR which probes local fluctuations (or equivalently the Cu^{2+} spin autocorrelation function) should be driven by the correlated spin dynamics at the 2D AF

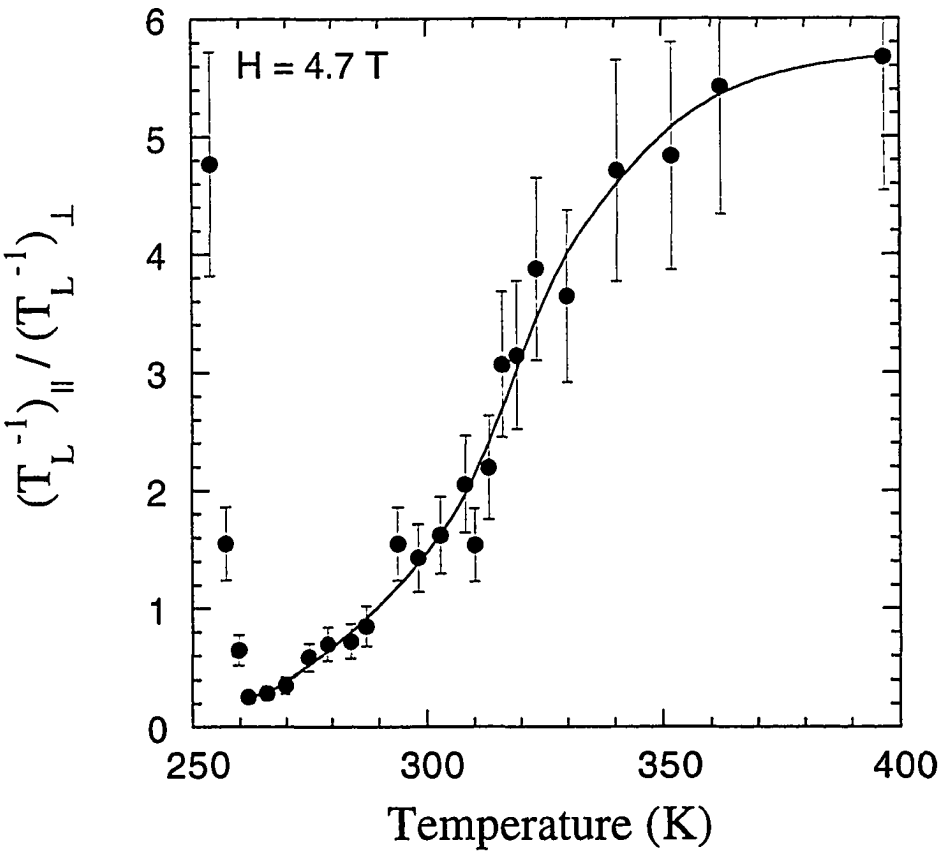

Fig. 3.9 The ratio $(T_L^{-1})_{\parallel} / (T_L^{-1})_{\perp}$ vs temperature. The curve is only a guide for the eye.

wave vector $\boldsymbol{q} = (\pi/a, \pi/a)$. Thus by applying dynamical scaling arguments we can write [see Eq. (2.23)]: $2W_{\parallel} \propto \xi_{\perp}^{z-\eta}$ where $\xi_{\perp}$ is the correlation length of the Cu^{2+} *ab* plane spin components and z, η are critical scaling exponents [22]. In Fig. 3.10, in the temperature range $300 < T < 400$ K, the NSLR is described by an exponential law: $2W_{\parallel} \propto \xi_{\perp}^{z-\eta} \propto \exp[(2310\text{ K})/T]$ while in the temperature range $260 < T < 280$ K the NSLR can be fit as $2W_{\parallel} \propto \xi_{\perp}^{z-\eta} \propto \exp[(3080\text{ K})/(T-231\text{ K})]^{1/2}$. The behavior found here for $\xi_{\perp}$ above room temperature is consistent with the expression which fits the neutron scattering [42] and Monte Carlo [40,41] data, i.e. $\xi_{\perp} \propto 0.276\exp(1.25J/T)$ for $J = 1450$ K and $z-\eta = 1.3 \pm 0.2$. On the other hand, the faster divergent behavior observed in the 20 K range just above T_N is consistent with $\xi_{\perp} \propto \exp[B/(T-T_c)]^{1/2}$ pertaining to an *XY* model with $T_c = 231 \pm 5$ K and $B = 1.3J \pm 0.2J$ in reasonable agreement with theoretical calculations [40,41] which, for an anisotropy $J^{XY} = 1.4\times10^{-4}\,J$ [42], predict $T_c = 243$ K. The dipolar and other weak interactions yield an easy-axis anisotropy in the *ab* plane of order 10^{-5} K [45]. Although this tiny anisotropy is important in deciding the spin structure below T_N [45], it would lead to a crossover to Ising-like dynamic behavior only extremely close to T_N and can thus be disregarded.

3.1.4.4 Magnetic-Field Effects

When an external magnetic field is applied in the *ab* plane, the field creates an additional small Ising-like anisotropy which is evidently an order of magnitude or more greater than the other in-plane anisotropies [45] for fields larger than 1 Tesla as shown next [46], and we therefore neglect all but the field-induced in-plane anisotropy in the following. In this case, the Cu^{2+} spin system is shown to be driven towards a 2D Ising-like system and the T_N increases as shown above in Fig. 3.7. In order to test this model quantitatively we start by estimating the effective field-induced anisotropy parameter $D(H)$ given by (see Appendix)

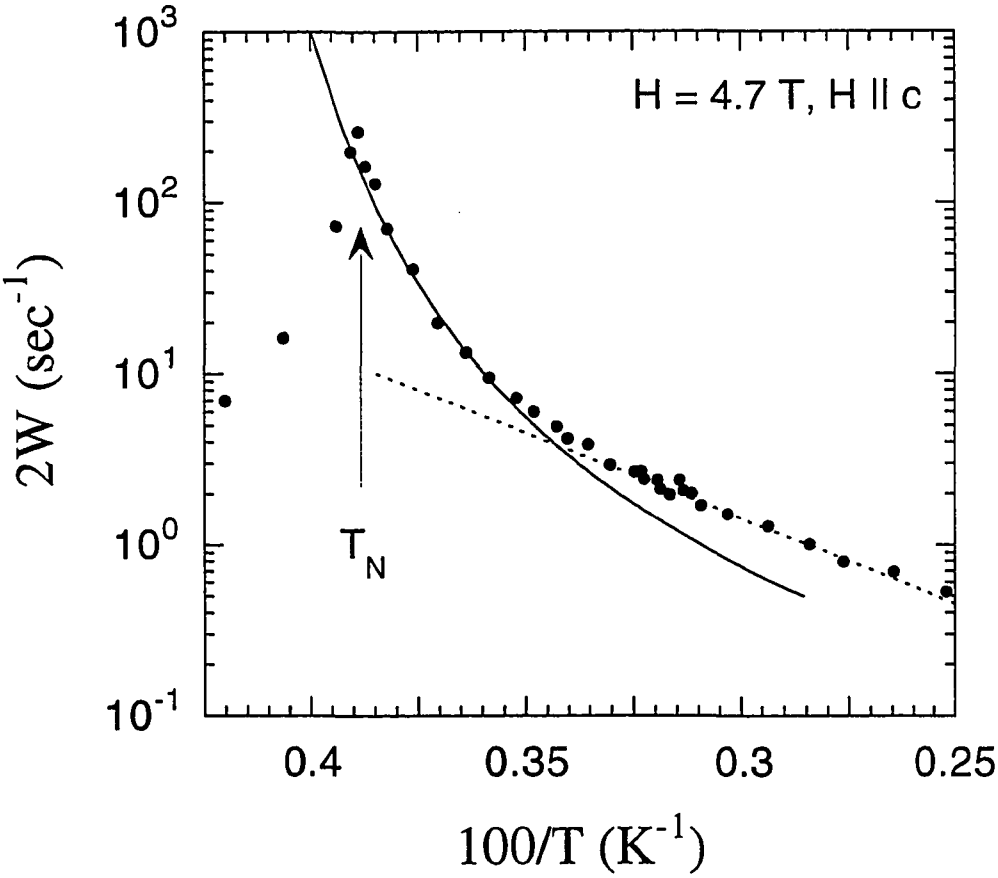

Fig. 3.10 Plot of NSLR ($2W$) for $\boldsymbol{H} \parallel \boldsymbol{c}$, $2W_{\parallel}$, as a function of reciprocal temperature. The lines are best fits to the data above T_N: dotted line, $2W_{\parallel} \propto \exp[(2310\ \mathrm{K})/T]$, and solid line, $2W_{\parallel} \propto \exp[3080\ \mathrm{K}/(T-231\ \mathrm{K})]^{1/2}$

$$D(H) = \frac{g^2 \mu_B^2 H^2}{4nJ(K)} \,. \tag{3.9}$$

Equation (3.9) was used successfully to explain field-induced anisotropic effects in 1D and 2D AF systems [46,50-52], and we have $D(H) = 7.75\times 10^{-5}\, H^2$ (K) (with H in Tesla, for the number of the nearest neighbors $n = 4$, $g = 2$ and $J = 1450$ K). Although small, the field-induced anisotropy can induce a 2D $XY \rightarrow$ 2D Ising crossover at a temperature T_{co}. From general scaling arguments [40,41], one expects the crossover to occur when $\xi_{XY}(T_{co}) \sim 1/\sqrt{D(H)}$, a mean field result, and the 3D transition at T_N should occur soon thereafter with decreasing temperature due to finite interlayer coupling. Thus, in analogy with the 2D Heisenberg to 3D Heisenberg crossover expression in the molecular field approximation given in e.g., Eq. (7) in Ref. [41], one has in the present case:

$$D(H)\cdot S^2 \cdot \frac{\xi_{XY}^2(T_{co})}{a^2} \cong T_{co}. \tag{3.10}$$

We suggest that as long as $T_{co}(H) < T_N(H = 0)$, the 3D transition is triggered by the small interplane coupling J' in conjunction with the 2D XY correlation length. When $T_{co}(H) > T_N$ $(H = 0)$ the 3D transition, while still triggered by J', is expected at a temperature just below T_{co} since for an Ising system the correlation length diverges at finite temperature. To evaluate $T_{co}(H)$ from Eq. (3.10), we use the temperature dependence of the correlation length in the XY regime obtained from the fit of $2W_{\|}$ vs. temperature in Fig. 3.10: $\xi_{XY}(T)/a = P \exp[1.3J/(T\text{–}231\text{ K})]^{1/2}$. The constant P can be estimated by matching the Heisenberg and XY correlation lengths at $T = 290$ K (see Fig. 3.10): $[\xi(290\text{ K})/a]_{\text{Heis.}} = [\xi(290\text{ K})/a]_{XY}$ and by using $[\xi(T)/a]_{\text{Heis.}} = 0.276\exp(1.25J/T)$, the Monte Carlo calculation results [40,41], yielding $P = 0.49 \pm 0.1$. Thus, with $\xi_{XY}/a = 0.49\exp[(1900\text{ K})/(T\text{–}231\text{ K})]^{1/2}$, one can evaluate $T_{co}(H)$ from Eq. (3.10) as shown in Fig. 3.7. Since the curve in Fig. 3.7 represents

$T_{co}(H)$, it is not a fit to the data but rather indicates that the experimentally measured $T_N(H)$ values have the same trend as the $XY \rightarrow$ Ising crossover temperature. This suggests that for $H \gtrsim$ 2 Tesla the 3D AF transition is driven by the rapid growth of the 2D in-plane correlation length due to the field-induced Ising-like anisotropy. Our interpretation is not expected to change when a quantum mechanical derivation of $T_{co}(H)$ becomes available; for example, decreasing S in Eq. (3.10) from 1/2 to 0.4, which might be expected due to quantum fluctuations, shifts our calculated $T_{co}(H)$ curve somewhat to higher H but still fits the trend of the data.

3.1.4.5 Anomalous Broadening and Anisotropy of NMR Lines

Anomalous broadening and anisotropy of the ^{35}Cl NMR line shift and width are observed as shown in Figs. 3.2 and 3.3, respectively. The linewidths, $\Delta\nu$, are in good agreement with previous results [44]. Regarding the shifts, K, vs T we can see a field independent enhancement of K in Fig. 3.2 for the applied field in the *ab* plane which could not be observed previously [44] due to poorer quality of the single crystal stack available previously. As discussed previously [44] the enhancement and the anisotropy of $\Delta\nu$ cannot be explained by demagnetization effects nor by random ferromagnetic impurities. Also, the magnetic susceptibility displays a weak temperature dependence with no enhancement close to T_N; thus the observed enhancement of $\Delta\nu$ and of K cannot be simply the result of the paramagnetism of the Cu^{2+} magnetic moments. On the other hand the results could be explained qualitatively if one assumes that the application of the magnetic field in the *ab* plane stabilizes static two-dimensional short range order of the Cu^{2+} moments [44]. It is interesting to note that the onset of the anisotropy in the line broadening occurs around the temperature at which $(T_L^{-1})_{\|}$, i.e. the out-of-plane fluctuations, $J_{\|}(0)$, decreases most rapidly (see Fig. 3.9).

3.1.5 Summary and Conclusions

In conclusion, we have demonstrated the occurrence of crossover effects due to the small anisotropies present in the $S = 1/2$ 2DSLHA $Sr_2CuO_2Cl_2$. From the suppression of the out-of-plane fluctuations and from the critical enhancement of the ^{35}Cl NSLR, we infer that around 290 K the correlation length of the Cu^{2+} in-plane spin components crosses over from Heisenberg behavior $(\xi/a)_{Heis.} = 0.276\exp(1.25J/T)$ as given by neutron scattering results in zero field [42] to XY-like behavior $(\xi/a)_{XY} = 0.49\exp[1.3J/(T-231\text{ K})]^{1/2}$. The result was obtained for $\boldsymbol{H} \parallel \boldsymbol{c}$. Since for this orientation of the external magnetic field the symmetry in the ab plane is preserved, one expects almost identical behavior in zero field. Recent neutron scattering results in zero field do indeed indicate a suppression of out-of-plane fluctuations occurring below about 300 K [53], in agreement with our results. On the other hand, for $\boldsymbol{H} \perp \boldsymbol{c}$ the field induces an additional anisotropy and, as a consequence, the T_N increases. For example, for $S = 1/2$, the field for which the system would cross over from XY to Ising-like at $T_N(H = 0) = 257$ K is $H_{co} = 1.4$ Tesla (Fig. 3.7) as obtained by setting $T_{co} = 257$ K in Eq. (3.10) and solving for H.

Generally our data can be explained quantitatively in terms of crossover effects near T_N with a coherent and reasonable set of parameters which are in agreement with the parameters already reported in the literature [42]. Thus we have described the spin correlations in the spin $S = 1/2$ 2DSLHA with weak XY anisotropy and in an external magnetic field.

Finally, it is noted that the magnitudes of all the parameters of the ^{35}Cl NMR are too large to be accounted for by a "bare" dipolar interaction between ^{35}Cl and Cu^{2+} magnetic moments as in Eqs. (3.5) and (3.8). It is quite likely that the partial covalent Cl-Cu bond induces an enhanced pseudo-dipolar interaction which we infer to be almost one order of magnitude larger than the "bare" dipolar interaction in order to explain the data.

4. NMR AS A MICROSCOPIC PROBE TO STUDY ELECTRONIC AND MAGNETIC PROPERTIES

NMR measurements were performed in two superconductors: $HgBa_2CuO_{4+\delta}$ which is a HTSC of the CuO_2 family and YNi_2B_2C which belongs to a class of newly discovered quaternary intermetallic compounds with behavior close to the conventional superconductors. The NMR study of the microscopic electric and magnetic properties presented here allows one to make an interesting comparison between the distinctive features of the two kinds of superconductors.

4.1 Fermi-Liquid Behavior in $HgBa_2CuO_{4+\delta}$ from ^{199}Hg NMR in an Oriented Powder Sample

4.1.1 Introduction

$HgBa_2CuO_{4+\delta}$ (Hg1201) which has the highest critical temperature, T_c, among the single CuO_2 layered compounds, is a good system for an NMR study of HTSC because of its relative simple structure [54] and its stability with respect to oxygen stoichiometry. There is only one kind of Cu site in the usual square planar coordination with four oxygen atoms in the same plane of the Cu. The copper oxide planes are linked by O-Hg-O chains which involve the apical oxygens [denoted O(2)]. As proved in the preliminary ^{199}Hg NMR study in Hg1201 powder sample [55], the ^{199}Hg nucleus ($I = ½$) is a promising probe

for an NMR study of the properties of the Fermi liquid because: (i) there is no perturbation due to quadrupole interaction, (ii) the large atomic hyperfine coupling constant allows one to have a sensitive probe of the behavior of the Fermi liquid, and (iii) the symmetric location of Hg in the crystal lattice filters out the antiferromagnetic (AF) fluctuations of Cu electronic spins [56] provided that they are correlated between adjacent CuO_2 planes.

The Knight shift (K), the nuclear spin-spin relaxation rate (T_2^{-1}), and the nuclear spin-lattice relaxation rate (NSLR, T_1^{-1}) have been measured as functions of temperature for two crystal orientations with respect to the applied field, $\boldsymbol{H} \parallel \boldsymbol{c}$ and $\boldsymbol{H} \perp \boldsymbol{c}$. All the NMR parameters are found to be driven by the coupling with the Fermi liquid of the charge carriers and they give information about the spin susceptibility in both the normal and the superconducting state including the superconducting energy gap and the symmetry of pairing in the superconducting state. A small anisotropy in the relaxation rate with respect to the magnetic field orientation is observed below T_c and above the irreversibility temperature. The effect can be ascribed to a contribution to nuclear relaxation associated with the thermal motion of vortices as will be discussed in chapter 5.

4.1.2 Experimental Details

A single-phase powder sample of optimally oxygen-doped Hg1201 with $T_c = 96$ K was prepared at Texas Center for Superconductivity at the University of Houston by Q. Xiong [57,58]. The powder grains of an average diameter 12~20 μm were mixed with a low viscosity and low magnetic susceptibility out-gassed epoxy (EPOTEK 301) in a Teflon container and placed in a magnetic field of 8.2 Tesla for 15 h. A flat-plate sample was prepared for the x-ray diffraction studies to test whether the c axis of the grain-aligned sample was perpendicular to the surface of the plate. At the same time cylindrical samples with different sizes were made for both magnetization and NMR measurements.

X-ray diffraction patterns (measured at Ames Laboratory by M. Xu) for an aligned sample is shown in Fig. 4.1 where the enhancement of background intensity at low diffraction angle is from the amorphous epoxy. By comparing the relative intensity of the (003) line with the (102) main line characteristic of the randomly oriented powder [55], we could estimate that more than 85 % of the grains are aligned with the crystallite *c* axis along the field. Although the alignment obtained is not perfect, it is sufficient to give detailed information on the orientation dependence of the Knight shift and relaxation rates because of the large anisotropy of the Knight shift in the whole temperature range investigated. These data will be shown and discussed in the following section.

The sample quality after alignment was characterized by DC magnetization measurements (performed at Ames Laboratory by J. Sok) to test whether the sample has been contaminated in the alignment process or not. As shown in Fig. 4.2, a sharp superconducting transition was observed for the aligned sample, strongly suggesting that the sample quality was not affected by the alignment process.

^{199}Hg NMR measurements were performed at 62 MHz in a magnetic field of 8.2 Tesla. Typical $\pi/2$ radio frequency (rf) pulse lengths for ^{199}Hg were 4 μs corresponding to an rf magnetic field strength of 80 G. The rf field strength was sufficient to cover the whole spectrum with the linewidth less than 60 kHz above 20 K for both orientations. NMR spectra were obtained from the FT of half of the echo signal. The spin-echo decay rate, T_2^{-1}, was monitored with an ordinary two-pulse spin-echo (TPSE) sequence $(\pi/2)_x - \tau - (\pi)_y$ with variable τ separation. The nuclear spin-lattice relaxation rate (NSLR, T_1^{-1}) measurements were performed by monitoring the return to thermal equilibrium of the nuclear magnetization with a $\pi/2$ rf pulse after inverting the magnetization with a π rf pulse.

All measurements were taken in field cooled conditions with an applied magnetic field of 8.2 T which is much greater than the lower critical field H_{c1}, and in the temperature range 10 K < T < 300 K for two crystal orientations with respect to the applied magnetic field: $\boldsymbol{H} \parallel \boldsymbol{c}$ and $\boldsymbol{H} \perp \boldsymbol{c}$.

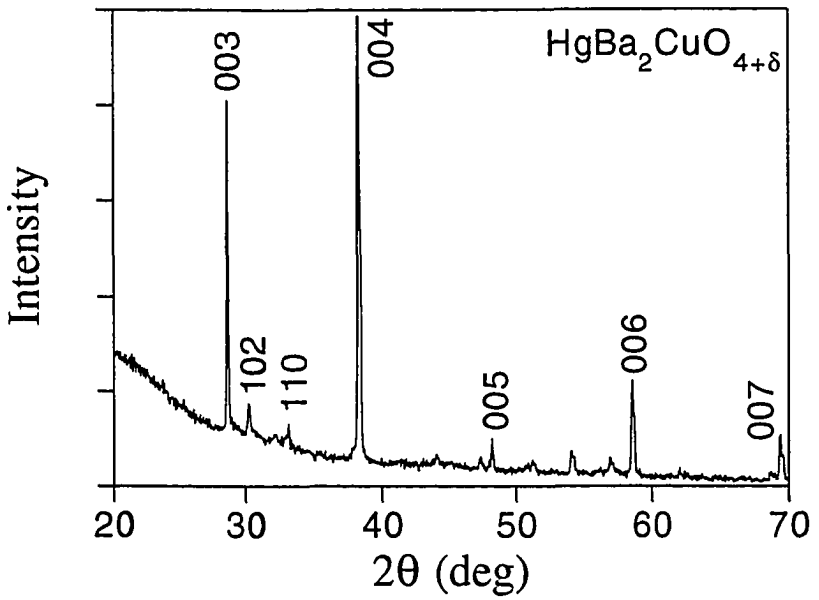

Fig. 4.1 X-ray diffraction pattern of an optimally oxygen-doped $HgBa_2CuO_{4+\delta}$ powder sample with grains aligned with a common crystallite *c* axis. (Courtesy of M. Xu)

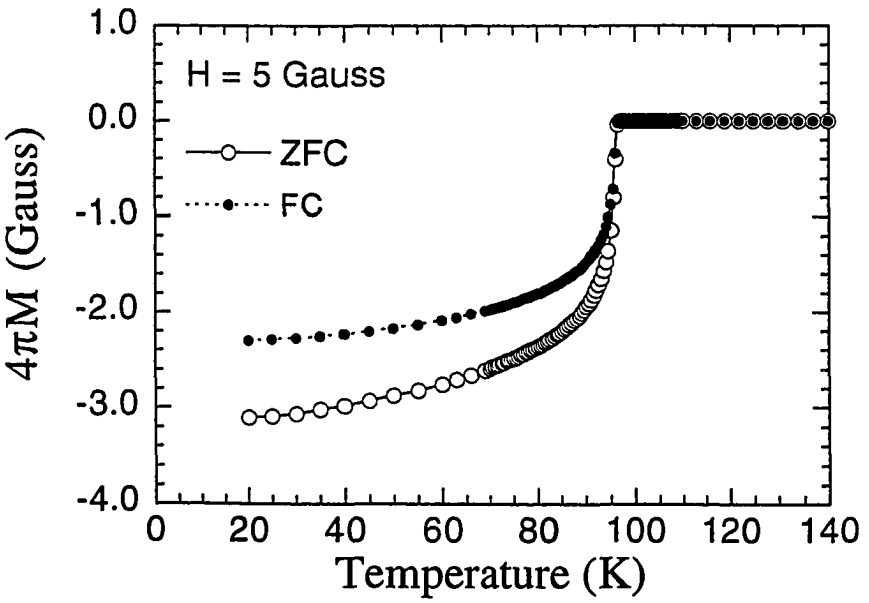

Fig. 4.2 DC magnetization for $H \parallel c$ vs temperature for the aligned $HgBa_2CuO_{4+\delta}$ sample: (o) Zero field cooled and (•) Field cooled. (Courtesy of J. Sok)

4.1.3 Results

4.1.3.1 ^{199}Hg NMR Spectrum and Knight Shift (K)

Representative ^{199}Hg NMR spectra in the oriented powder sample are shown in Fig. 4.3 for both orientations, $\boldsymbol{H} \parallel \boldsymbol{c}$ and $\boldsymbol{H} \perp \boldsymbol{c}$, and compared with the powder spectrum obtained from a randomly oriented powder sample of Hg1201 [55] in order to show the good correspondence of the powder pattern features with the oriented powder signals. The signals for the oriented powder are slightly anisotropic revealing the presence of some powder not aligned as indicated also by the x-ray diffraction pattern in Fig. 4.1. In spite of the small degree of misalignment of the sample, the large anisotropy of the Knight shift allows for sufficient spectral resolution to measure the orientation dependence of the Knight shifts and the relaxation rates with good accuracy.

The Knight shifts, $K_{\parallel}$ and $K_{\perp}$, were obtained from the relative frequency shift of the peak positions of the spectra with respect to the ^{199}Hg resonance frequency in an aqueous solution of $Hg(NO_3)_2$. The results are shown in Fig. 4.4 as a function of temperature while in Table 4.1 we give numerical results for three representative temperatures. Both $K_{\parallel}$ and $K_{\perp}$ are found to decrease rapidly below T_c as expected for the superconducting gap opening. An important feature for the interpretation of the data is the linear relation between $K_{\parallel}$ and $K_{\perp}$ which holds in the whole temperature range investigated as shown in the inset of Fig. 4.4. A linear relation between $K_{\parallel}$ and $K_{\perp}$ was previously reported for ^{89}Y NMR in

Table 4.1 ^{199}Hg Knight shifts in Hg1201 at three representative temperatures; K^{tot} is the observed total Knight shift and K^{sp} is the spin contribution term extracted by using the Korringa relation.

T (K)	$K_{\parallel}^{tot}$ (%)	$K_{\perp}^{tot}$ (%)	K_{iso}^{tot} (%)	K_{ax}^{tot} (%)	K_{iso}^{sp} (%)	K_{ax}^{sp} (%)
294	-0.19	0.26	0.11	-0.15	0.07	0.01
102	-0.21	0.25	0.10	-0.15	0.06	0.01
15	-0.28	0.20	0.04	-0.16	≈0.0	≈0.0

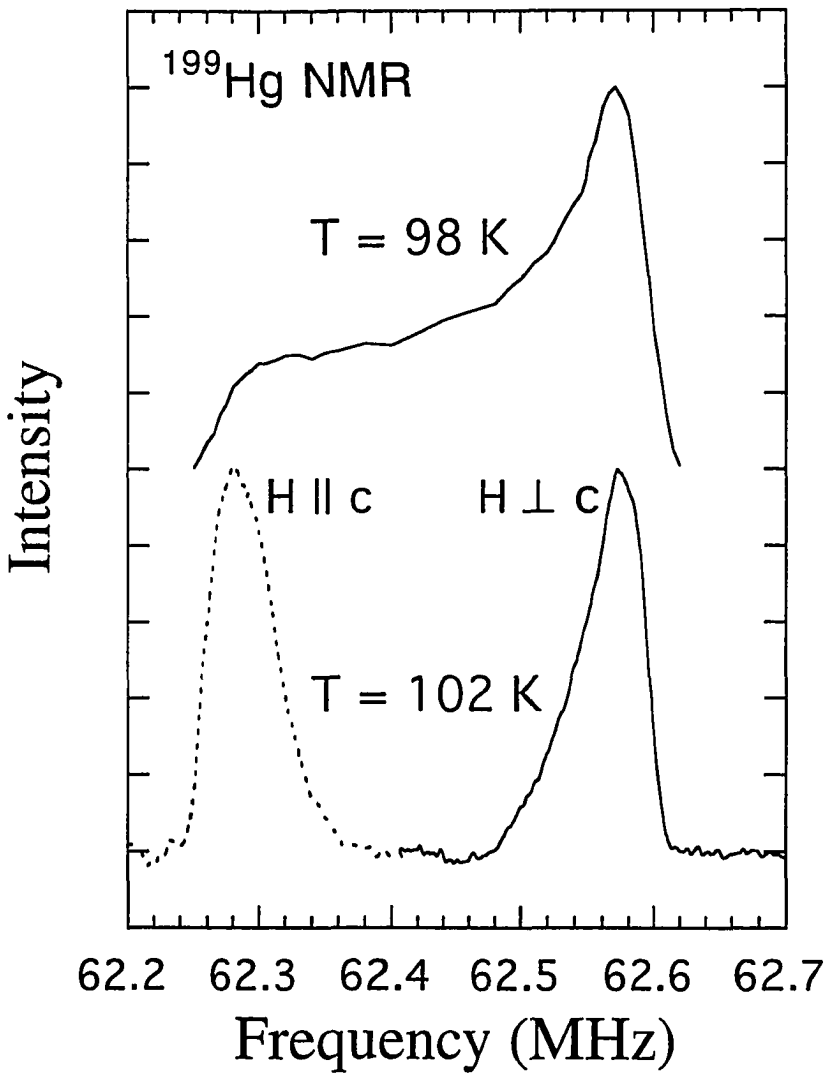

Fig. 4.3 Representative ^{199}Hg NMR spectra for $H = 8.2$ T in a randomly oriented powder sample (upper trace) and in the aligned sample for two orientations of the external magnetic field (lower trace): for $\boldsymbol{H} \parallel \boldsymbol{c}$ (dashed) and for $\boldsymbol{H} \perp \boldsymbol{c}$ (solid).

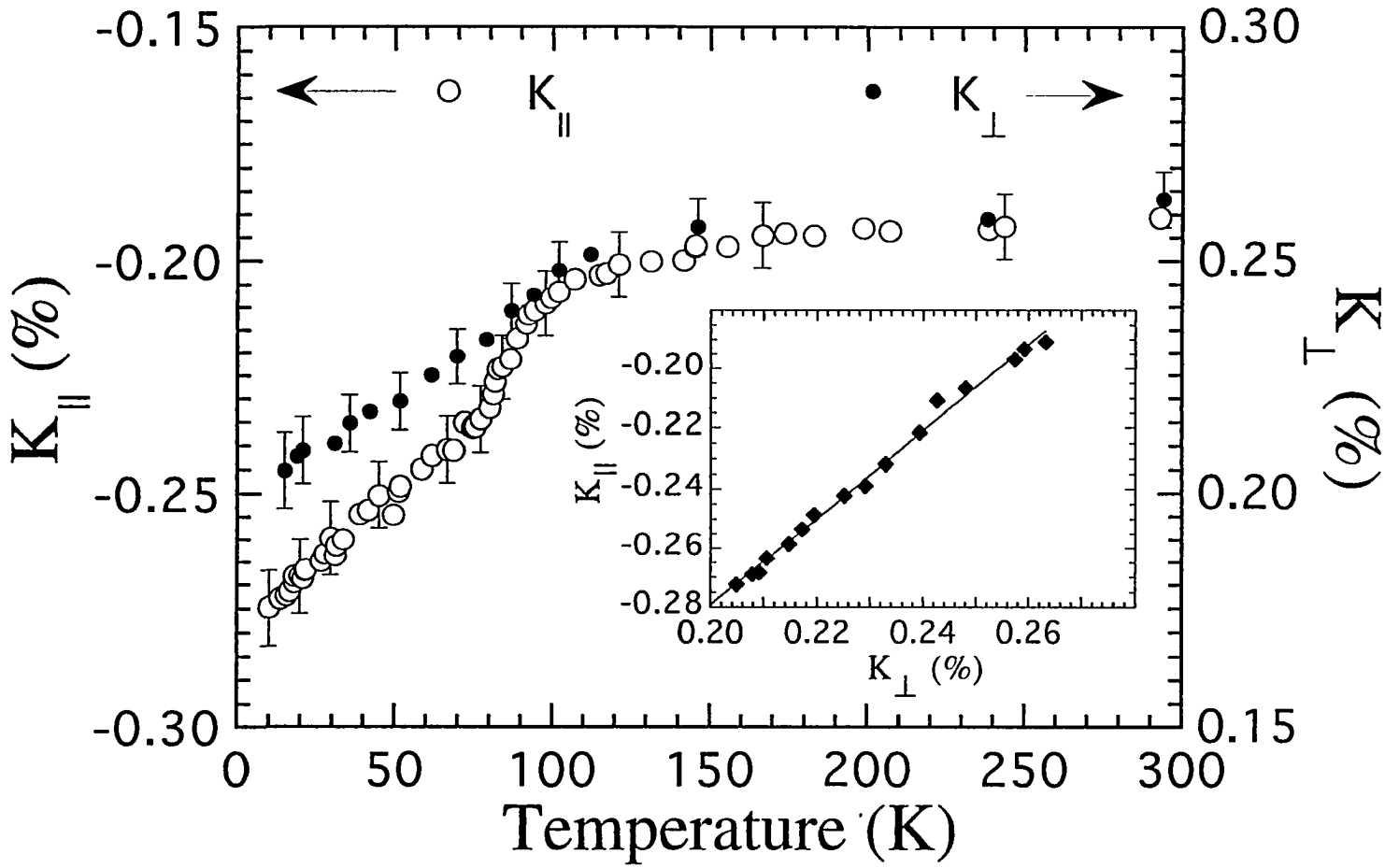

Fig. 4.4 Plots of the ^{199}Hg Knight shifts for two orientations of the external magnetic field: (o) $K_{\parallel}$ for $\boldsymbol{H} \parallel \boldsymbol{c}$ and (•) $K_{\perp}$ for $\boldsymbol{H} \perp \boldsymbol{c}$. Note the different scales for $K_{\parallel}$ and $K_{\perp}$. The inset is a plot of $K_{\parallel}$ vs $K_{\perp}$.

$YBa_2Cu_3O_7$ (Y123) [59]. This linear relation will be discussed later as evidence supporting the single-spin component picture.

4.1.3.2 Nuclear Spin-Lattice relaxation rate (NSLR, T_1^{-1})

The ^{199}Hg nuclear magnetization recovery was found to obey a single exponential law in the whole temperature range investigated. The results for NSLR, T_1^{-1} are shown in Fig. 4.5 as a plot of $(T_1T)^{-1}$ vs T for both orientations of the external magnetic field with respect to the tetragonal c axis. The Korringa behavior, $(T_1T)^{-1} = 0.1$ sec^{-1} K^{-1}, in the normal state and the sharp decrease of $(T_1T)^{-1}$ below T_c were observed. The absence of a measurable orientation dependence of T_1^{-1} in the normal state is an important result considering the large anisotropy of K. The measurements reported here are more accurate than the previous powder measurements [55] and allow one to measure a small but detectable deviation from a constant $(T_1T)^{-1}$ starting about 10 K above T_c.

Below T_c the NSLR drops rapidly without any sign of a coherence peak, a common trend in HTSC. An anomalous enhancement of $(T_1T)^{-1}$ can be observed around 30 K for $\boldsymbol{H} \parallel \boldsymbol{c}$. The anomaly is probably to be explained by an additional relaxation mechanism due to the thermally activated flux motion [7]. A systematic investigation of this effect with measurements at different applied magnetic fields will be discussed in chapter 5. The anomalous enhancement is not present for $\boldsymbol{H} \perp \boldsymbol{c}$ since for this field orientation the flux lines are not defined in these highly anisotropic systems [60].

4.1.3.3 Nuclear Spin-Spin Relaxation Rate (T_2^{-1})

The relaxation of the transverse magnetization which is characterized by the spin-spin relaxation rate, T_2^{-1}, shows an unusual temperature dependence. Above T_c the decay of the transverse nuclear magnetization, $M(t)$, in a two-pulse spin echo (TPSE) experiment follows a Gaussian law. Below T_c the decay progressively approaches an exponential time dependence. Some typical decays of the echo amplitude are shown in Fig. 4.6(a) for the purpose of illustration of the effect. In order to analyze the data we utilized two different

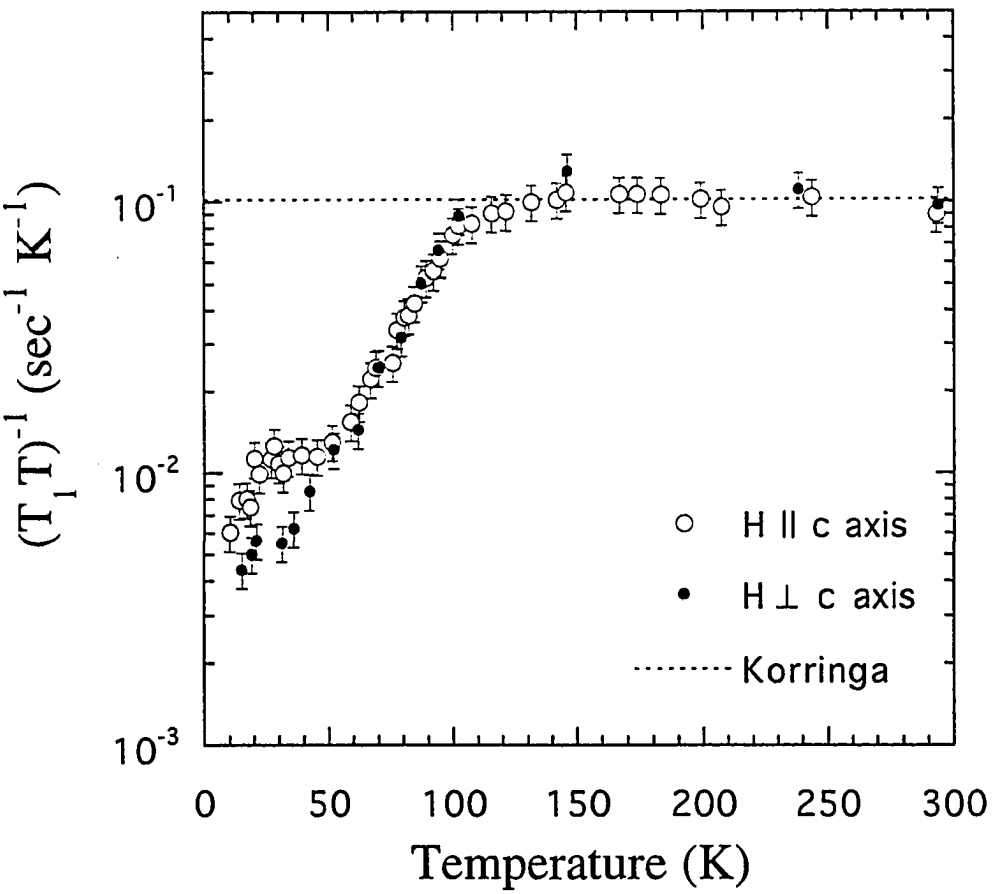

Fig. 4.5 Temperature dependence of $(T_1T)^{-1}$ of ^{199}Hg for both orientations of the external magnetic field: (o) $\boldsymbol{H} \parallel \boldsymbol{c}$, and (•) $\boldsymbol{H} \perp \boldsymbol{c}$. The dashed line is a fit to a Korringa behavior; $(T_1T)^{-1} = 0.1$ sec^{-1} K^{-1}.

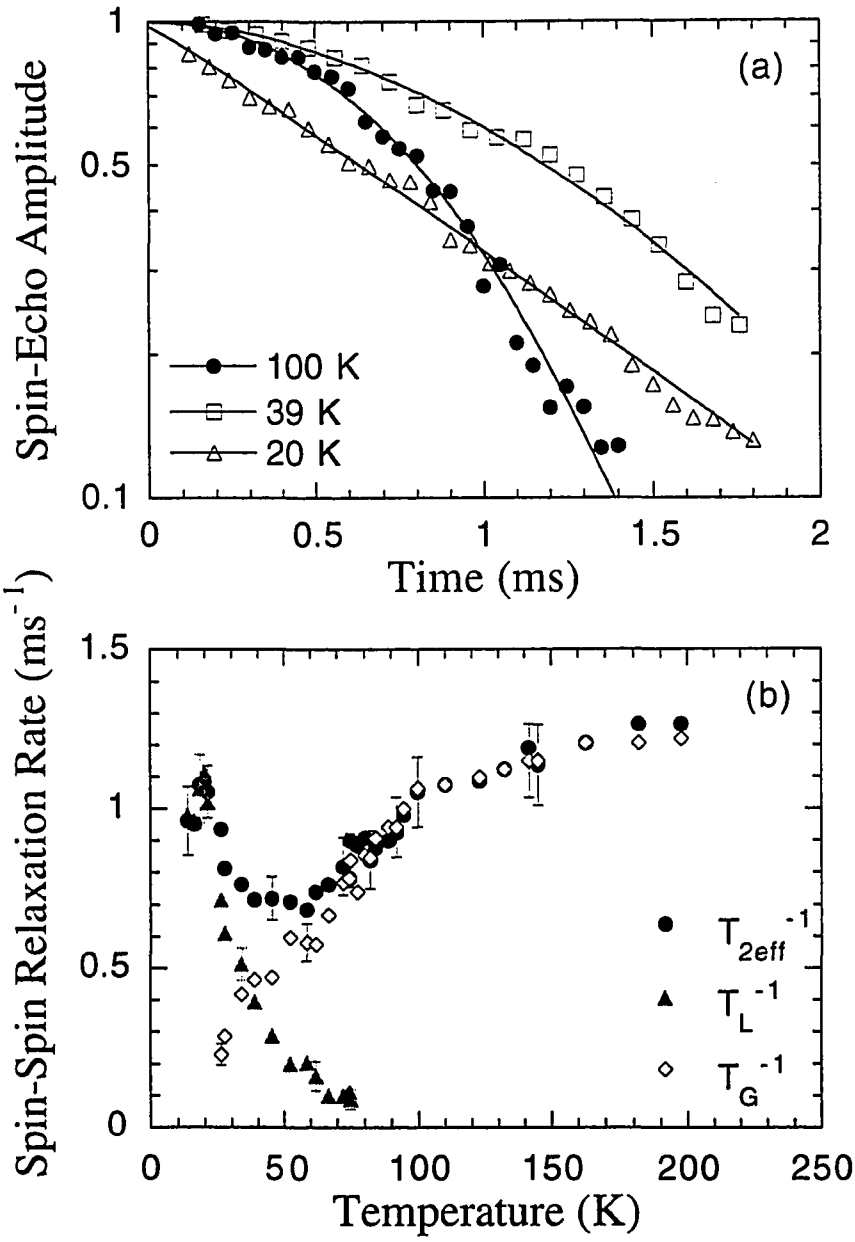

Fig. 4.6 (a) Representative decays of the spin-echo amplitude as a function of the pulse separation, $t = 2\tau$, in a two-pulse spin echo experiment. (b) Temperature dependence of the different parameters extracted from the fit of the spin-echo decay: (•) T_{2eff}^{-1}, (▲) T_L^{-1} and (◊) T_G^{-1} (see the text for details).

methods: the simplest is to define an effective T_{2eff} from the condition $M(T_{2eff})/M(0) = 1/e$; the second method is to fit the spin-echo decay using the expression [15]:

$$M(t) = M(0)\exp\left(-\frac{t}{T_L}\right)\exp\left[-\left(\frac{t}{T_G}\right)^2\right]. \qquad (4.1)$$

The temperature dependence of both T_{2eff}^{-1} and the two components, T_L^{-1} and T_G^{-1}, of the spin-echo decay are plotted in Fig. 4.6(b) for ^{199}Hg in Hg1201 for $\boldsymbol{H} \parallel \boldsymbol{c}$.

An interesting observation is the anomalous enhancement of T_L^{-1} which has a peak around 20 K. Similar anomalies of T_2^{-1} were already reported for ^{89}Y in Y123 [31], discussed in chapter 5, and ^{205}Tl in $Tl_2Ba_2Ca_2Cu_3O_{10+\delta}$ [61] and explained by the effect of thermally activated flux motion. This effect will be discussed in section 5.2 together with the anomaly of T_1^{-1}. On the other hand, the Gaussian component of the spin-echo decay, i.e. T_G^{-1}, is believed to arise from the ^{199}Hg nuclear magnetic dipolar interaction. Its magnitude and temperature dependence is interpreted in the following paragraph as due to the pseudo-dipolar interaction via the conduction electrons (holes).

4.1.4 Data Analysis and Discussion

4.1.4.1 Anisotropy of the Shift Tensor

The ^{199}Hg NMR shift is very anisotropic as is evident from the spectra in Fig. 4.3. We argue here that the large observed anisotropy originates mostly from the orbital currents induced by the field $\boldsymbol{H}$ in the linear dumbbell configuration of the Hg-O(2) bond.

In fact, the total axial shift, K_{ax}^{tot}, defined in Eq. (2.29) remains almost constant as $T \rightarrow 0$, as shown in Fig. 4.4 and Table 4.1, indicating that K_{ax}^{tot} is not related to the spin susceptibility. Furthermore it is unlikely that the shift anisotropy can originate from an anisotropy of the temperature independent Van Vleck (VV) contribution to the magnetic

susceptibility. Such an anisotropy would be at least partially reflected in the NSLR, T_1^{-1}, behavior which instead is practically isotropic above 50 K as shown in Fig. 4.5. Finally in order to estimate the contribution to the shift anisotropy from the dipolar interaction of the ^{199}Hg nucleus with the localized Cu magnetic moments, the dipolar field at the ^{199}Hg site was calculated by summing over a cube with a side length 30 times the lattice parameter a of the tetragonal Hg1201 crystal and using the expression for the dipolar field, $\vec{h}$, from the Cu at $r = r_j$ [2,3]

$$\vec{h}_j = \frac{3(\langle\vec{\mu}\rangle \cdot \vec{r}_j)\vec{r}_j}{r_j^5} - \frac{\langle\vec{\mu}\rangle}{r_j^3}\,,$$
$$K_{ax}^{dip} = \frac{1}{3}(K_{\parallel}^{dip} - K_{\perp}^{dip}) = \frac{1}{3}\frac{\sum_j h_{\parallel,j} - \sum_j h_{\perp,j}}{H}\,, \tag{4.2}$$

where <μ> is the thermal average of the paramagnetic moment of the Cu ion induced by the applied field $\boldsymbol{H}$. Assuming an isotropic susceptibility per atom $\chi = <\mu>/H = 4 \times 10^{-28}$ emu/Cu atom [55] and from the known Hg-Cu distance, $d = 4.76$ Å [54], one has $K_{ax}^{dip} = 2.4 \times 10^{-3}$ %. This value is almost two orders of magnitude smaller than the measured value and has the opposite sign (see Table 4.1). Thus we conclude the large observed shift anisotropy should be ascribed almost entirely to the anisotropic chemical shift originating from the linear configuration of the Hg-O(2) bond.

The contribution to the anisotropy of the shift, K_{ax}, arising from the spin susceptibility, although small, is not entirely negligible. This can be seen by the fact that K_{ax} is slightly temperature dependent. In order to extract the spin component of K_{ax} we note that from the fit of the data in Fig. 4.4 we find:

$$K_{\parallel}^{tot} = 1.46K_{\perp}^{tot} - 0.57\ (\%)\,. \tag{4.3}$$

By combining Eq. (2.28) and Eq. (4.3) one has:

$$K_{ax}^{tot} = 0.13K_{iso}^{tot} - 0.17\ (\%)\ . \tag{4.4}$$

Here, both K_{iso}^{tot} and K_{ax}^{tot} consist of two components: the spin and the orbital contributions. Based on the notion that the orbital contribution, K_{iso}^{orb} and K_{ax}^{orb} should be independent of temperature, we can write:

$$K_{ax}^{sp}(T) = 0.13K_{iso}^{sp}(T)\ . \tag{4.5}$$

Note, the spin part of the shift tensor K_{iso}^{sp} is derived independently from the total shift in the next paragraph. As for normal metals, the term K_{iso}^{sp} is expected to arise from the contact or transferred hyperfine interaction of the nuclei with the *s*-wave part of the conduction electrons at the Fermi level while the term K_{ax}^{sp} is due to the nucleus-electron dipolar interaction averaged over the non-*s* wave functions of the conduction electrons at the Fermi level [12]. For ^{199}Hg in Hg1201 one expects $K_{ax}^{sp} \neq 0$ since the nucleus sits in a site with local axial symmetry.

The direct proportionality of the two components of the Knight shift tensor, K_{iso}^{sp} and K_{ax}^{sp}, [see Eq. (4.5)] is consistent with a single-spin component model since the oxygen holes and the Cu *d*-electrons have different hyperfine coupling constants with the ^{199}Hg nucleus and thus contribute in a different way to K_{iso}^{sp} and K_{ax}^{sp}. This implies that the generalized susceptibility, $\chi(q,\omega)$, should be viewed as a single *T*-dependent function which can be strongly *q*-dependent due to the enhancement at $q = q_{AF}$ related to the Cu spin AF fluctuations. Most of the NMR studies support the single-spin component model based on the same temperature dependence of ^{63,65}Cu, ^{17}O and ^{89}Y NMR in Y123 and Y124 [62-64] although the issue is not completely settled [65]. A more quantitative analysis of this point in Hg1201 requires NMR measurements on ^{63,65}Cu and ^{17}O nuclei which would be sensitive also to the components of $\chi(q,\omega)$ at $q = q_{AF}$.

Experimental observation of a negligible anisotropy of T_1^{-1}, $1 \leq T_\perp^{-1}/T_\parallel^{-1} \leq 1.1$, in the

normal state (see Fig. 4.5), is consistent with the small value of K_{ax}^{sp}/K_{iso}^{sp} since, according to the Korringa Relation [see Eq. (2.16)], T_1^{-1} scales as K^2 and only the coupling of the nucleus to the spin susceptibility is expected to contribute to the spin-lattice relaxation rate.

4.1.4.2 Knight Shift and NSLR

The observation of Korringa behavior $(T_1T)^{-1}$ = constant $\cong$ 0.1 sec^{-1} K^{-1} and the observation of negligible anisotropy of T_1^{-1} in the normal state suggest that the ^{199}Hg T_1^{-1} probes the Fermi liquid behavior at $q = 0$ through the isotropic contact hyperfine interaction without additional contributions coming from AF fluctuations at $q = q_{AF}$. This is consistent with the point symmetry of the Hg nucleus which implies a filtering of AF fluctuations of the Cu spins for 3D correlation of the spins. The simple Korringa relation [Eq. (2.16)] is valid for a weakly interacting Fermi gas. For a highly correlated Fermi liquid the proportionality of $(T_1T)^{-1}$ to K^2 may still be valid if the NSLR is dominated by the uniform ($q = 0$) generalized susceptibility. In order to verify this point we show in Fig. 4.7 the plot of $K_{\parallel,\perp}$ vs $(T_1T)^{-1/2}$. The K appears to scale linearly to $(T_1T)^{-1/2}$ for a wide temperature range including the superconducting and the normal states (50 K < T < 250 K). The deviation at high temperature (T > 250 K) may be due to a decrease of the filtering effect at the Hg site reflecting the decrease of 3D correlation of the AF fluctuations with increasing temperature or simply due to a sample inhomogeneity. The deviation at low temperature (T < 50 K) can be explained by an additional relaxation mechanism in the vortex state (see chapter 5) which is not an intrinsic property of the normal Fermi liquid. Thus, by assuming $(T_1T)^{-1/2} = K_\alpha^{sp} = K_\alpha(T) - K_\alpha^{orb}$ and K_α^{sp} ($T = 0$) = 0, the temperature independent term K_α^{orb} can be obtained by extrapolation to $(T_1T)^{-1/2} = 0$ as $T \rightarrow 0$. We find $K_\parallel^{orb}$ = -0.28 % and $K_\perp^{orb}$ = +0.21 %. Using the definition of K_{iso} and K_{ax} in Eq. (2.28), one has K_{iso}^{orb} = 0.04 % and K_{ax}^{orb} = -0.16 %. The spin contribution to the Knight shift, $K_{iso,ax}^{sp}$, can be obtained by subtracting the above estimates for $K_{iso,ax}^{orb}$ from the total Knight shift.

In Table 4.1, the values of K^{sp} are shown for representative temperatures. This analysis (especially for K_{ax}^{sp}) may include considerable uncertainties since we obtained the relatively small value of K_{ax}^{sp} by subtracting a large value of K_{ax}^{orb} from the total shift.

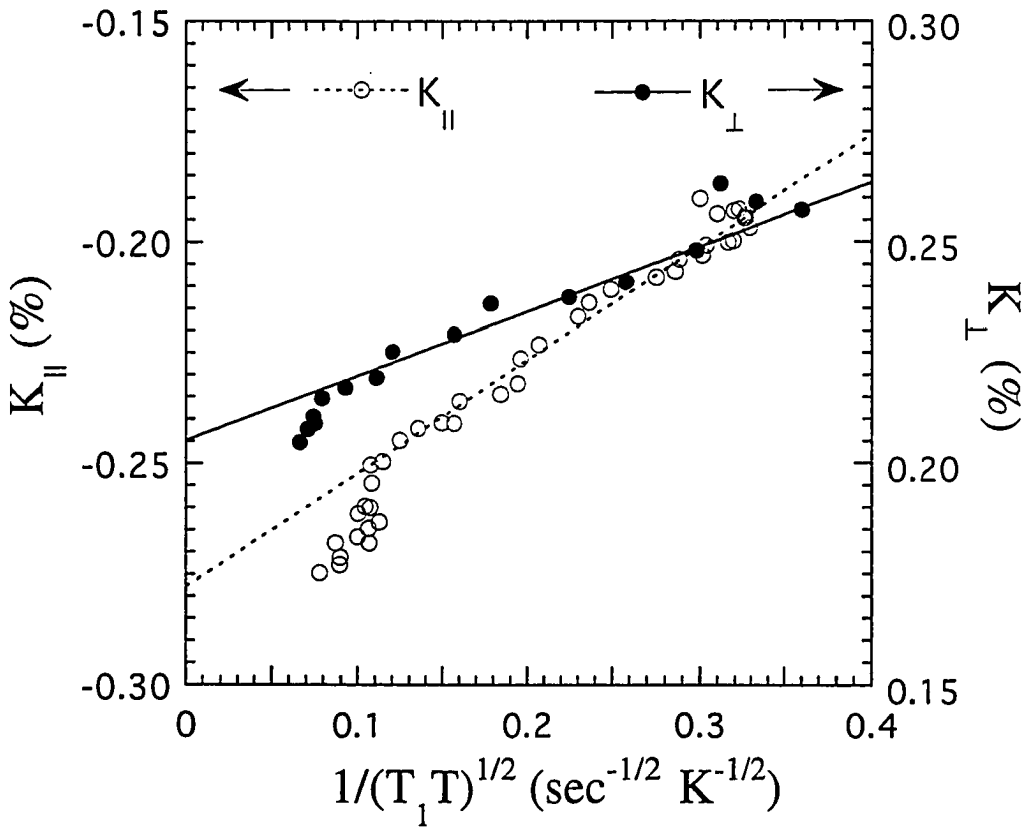

Fig. 4.7 Plots of the ^{199}Hg NMR shifts vs $(T_1T)^{-1/2}$: (o) $K_{\|}$, and (•) $K_{\perp}$. The two lines are fits to find the temperature independent $K_{\|,\perp}^{orb}$ using the Korringa relation; $K_{\|}(T) = -0.28 + 0.26(T_1T)^{-1/2}$ (solid line), and $K_{\perp}(T) = 0.21 + 0.15(T_1T)^{-1/2}$ (dashed line). Note the different scales for $K_{\|}$ and $K_{\perp}$.

Using the estimated K_{iso}^{sp}, one obtains a Korringa value, $K_{iso}^2 T_1 T = 0.51 \times 10^{-5}$ sec K in the temperature range 50 K < T < 250 K and the Korringa ratio [see Eq. (2.17)] $\kappa = 0.61$ for ^{199}Hg in Hg1201. This can be compared with the value of $\kappa = 1.1$ is derived for ^{199}Hg in Hg metal [66]. The Korringa ratio obtained here for ^{199}Hg in Hg1201, $\kappa = 0.61$, is not too far from the values quoted above for the simple Hg metal thus confirming that the ^{199}Hg NSLR is dominated by the coupling with the normal Fermi liquid without additional enhancements due to AF fluctuations. It is noted that the effect of ferromagnetic interactions among conduction electrons which is responsible for the Stoner enhancement of the uniform spin susceptibility would lead to a Korringa ratio greater than one, $\kappa > 1$ [12]. In Hg1201 the deviation of the Korringa ratio is in the opposite direction, i. e. $\kappa < 1$. This can be easily explained by the presence in K_{iso}^{sp} of a small negative term arising from the exchange polarization of *s*-electrons by Cu *d*-electrons [12].

From the data in Table 4.1 one sees that the ratio of the estimated values of the two components of K^{sp} is $K_{ax}^{sp}/K_{iso}^{sp} \cong 0.15$ in the normal state. This ratio is in good agreement with the ratio $K_{\parallel}^{sp}(T)/K_{\perp}^{sp}(T) \cong 0.13$ [see Eq. (4.5)] which is directly derived from the slope of $K_{ax}(T)$ vs $K_{iso}(T)$. We conclude that the ^{199}Hg K and T_1 are related by the Korringa relation with a value of the Korringa ratio close to one as for normal metals. Based on the above conclusion that ^{199}Hg NMR is a good probe to study the behavior of the Fermi liquid in Hg1201, we will discuss the properties of the Fermi liquid both in the normal and in the superconducting state in the following paragraphs.

4.1.4.3 Temperature Dependence of the Spin Susceptibility from K and T_2

As shown in the previous paragraph the analysis of the temperature dependence of $(T_1T)^{-1}$ and of the Knight shift allows one to separate the component related to the uniform spin susceptibility $\chi'(0,0)$ of the Fermi liquid from the total shift. The temperature dependence of $K^{sp}(T)$ which measures the temperature dependence of $\chi'(0,0)$ is shown in Fig. 4.8 and Fig. 4.9 below.

Before discussing the temperature dependence of $K^{sp}(T)$ we would like to reconsider the results of the nuclear spin-spin relaxation rate. As discussed before the echo amplitude decay curve can be fit as the product of a Gaussian decay characterized by a time constant T_G and a exponential one with a time constant T_L. For $T > 50$ K the Gaussian component is dominant as shown in Fig. 4.6. At room temperature $T_G^{-1} = 1.2$ ms^{-1}. This value is considerably larger than the value $(T_G^{-1})_{dip} \sim 10^{-2}$ ms^{-1} which can be estimated from a direct nuclear dipolar interaction among ^{199}Hg nuclei. We stress that only the homonuclear dipolar interaction contributes to the spin-echo decay in an ordinary echo sequence, $\pi/2$ - τ - π, as discussed in section 2.2. Thus we argue that the echo decay is dominated by an indirect nuclear interaction. This is not surprising since ^{199}Hg has a very large hyperfine coupling constant. The indirect nuclear interaction can be either a pseudo-exchange interaction of the form $A_{12}\vec{I}_1 \cdot \vec{I}_2$ or a pseudo-dipolar interaction of the form $B_{12}[\vec{I}_1 \cdot \vec{I}_2 - 3(\vec{I}_1 \cdot \vec{R}_{12})(\vec{I}_2 \cdot \vec{R}_{12}) / R_{12}^2]$ [3]. The importance of these indirect interactions in heavy metals and insulators was well documented in the pioneering works by Bloembergen and Rowland [67] and Ruderman and Kittel [68].

In the present case the indirect interaction of the ^{199}Hg nuclei is mediated by the Fermi liquid of oxygen holes and is expected to be equivalent to the pseudo-dipolar interaction in Tl and Hg metals [12]. In simple metals one expects that the pseudo-exchange interaction constant A_{12} behaves as a function of internuclear distant R as $(\sin 2k_F R - 2k_F R \cos 2k_F R)/R^4$ where k_F is the conduction electron wave vector at the Fermi level [3]. The expression for the pseudo-dipolar interaction B_{12} is more complicated and is related to the non-s components of the wave function of the conduction electrons [67]. In Fig. 4.8 we show that the spin component of the Knight shift appears to be directly proportional to T_G^{-1}. This observation suggests that the indirect pseudo-exchange and/or pseudo-dipolar interaction is simply proportional to the uniform spin susceptibility $\chi'(0,0)$. This conclusion is not surprising since the form of the indirect interaction discussed above is asymptotically (for large distances) proportional to k_F and hence to $\chi'(0,0)$.

It should be emphasized that the Gaussian component in the spin-echo decay of

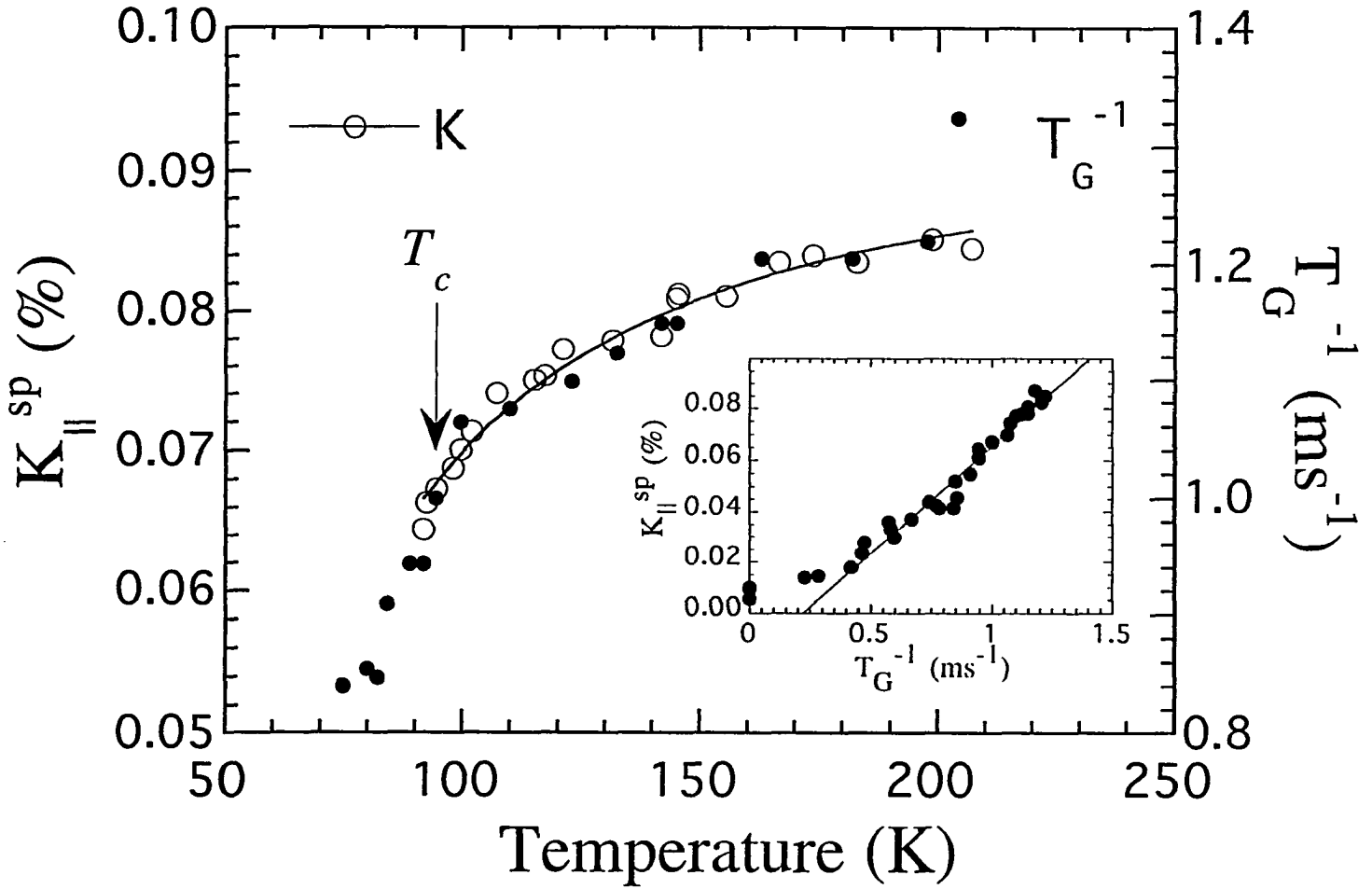

Fig. 4.8 Temperature dependence of the ^{199}Hg Knight shift and of the Gaussian component of the spin-spin relaxation rate: (o) $K_{\|}^{sp}$, and (•)T_G^{-1}. The solid line is a fit of $K_{\|}^{sp}$ by Eq. (4.6) in the text with the fitting parameters; K_o = 0.09 % and Δ_{sp} = 106 K. The inset is a plot $K_{\|}^{sp}$ vs T_G^{-1}.

^{63,65}Cu in Y123 and other HTSC first discussed by Pennington and Slichter [17] has the same origin as the pseudo-exchange interaction discussed above as implicitly recognized in a later work by Imai et al. [18]. While for ^{63,65}Cu the indirect nuclear interaction is proportional to the generalized susceptibility at $q = q_{AF}$ as a consequence of the enhancement of $\chi'(q_{AF},0)$ due to AF fluctuations and of the form of the filtering factors $A(q)$ [see Eq. (2.20)], for ^{199}Hg the indirect nuclear coupling is proportional to $\chi'(0,0)$ making the ^{199}Hg nucleus an ideal probe of the Fermi liquid behavior.

As shown in Fig. 4.8 both $K_{\parallel}^{sp}$ and T_G^{-1} decrease with decreasing temperature starting well above T_c. The effects on both T_G^{-1} and on K must arise from a decrease of the spin susceptibility, χ^{sp}. The decrease of χ^{sp} as evidenced by K^{sp} is a rather common phenomenon in HTSC except for the over-doped Y123 and has been attributed to the opening of a gap in the spin excitation spectrum, a so-called spin pseudo-gap. Although the origin of the pseudo-spin gap is still under debate [5,19,69], the phenomenological description of the temperature dependence for both the static and dynamic spin susceptibility seems to have a common ground [4]. Thus we tried to fit the ^{199}Hg NMR Knight shift data to the phenomenological expression given by

$$K(T) = K_o\left[1 - \tanh^2\left(\frac{\Delta_{sp}}{2T}\right)\right], \tag{4.6}$$

where the fitting parameter Δ_{sp} is the apparent spin gap energy at $q = 0$ and K_o is the constant value at high temperature. As shown in Fig. 4.8, the experimental K^{sp} values are found to fit well to Eq. (4.6) and the fitting value $\Delta_{sp} = 106$ K is close to the temperature at which $(T_1T)^{-1}$ starts to decrease (see Fig. 4.5).

One can envisage two possible explanations for the decrease of $\chi'(0,0)$ above T_c. The decrease can be the consequence of the transfer of spectral weight of the excitations from low frequency to high frequency. This is the dynamical spin pseudo-gap at $q = 0$ discussed in the literature. On the other hand a decrease of $\chi'(0,0)$ could be simply the consequence

of the transfer of intensity in the generalized susceptibility $\chi'(q,0)$ from $q = 0$ to $q = q_{AF}$ as a result of the enhancement of AF fluctuations, provided that the sum rule $\Sigma_q \chi'(q,0) = \text{const}$ is valid even for a system of delocalized magnetic moments [70]. The issue of the opening of a spin pseudo-gap in our sample appears to be of relevance since the Hg1201 used here is optimally doped ($T_c = 96$ K) and no decrease of $\chi'(0,0)$ above T_c was observed in optimally doped Y123. In order to clarify this point more measurements are needed on ^{63,65}Cu NMR which can probe the generalized susceptibility at q close to the AF wave vector q_{AF}.

4.1.4.4 Symmetry of the Pairing State

Here we analyze the Knight shift and NSLR data by comparing their temperature dependence below T_c with theoretical predictions obtained for both *s*-wave and *d*-wave gaps [71]. In Fig. 4.9 we plot the normalized value of the spin contribution to the Knight shift which should be a direct measure of the normalized spin susceptibility, i. e. $\chi_s^{sp}(0,0)/\chi_n^{sp}(0,0)$ where the subscripts *s* and *n* refer to the superconducting and normal state respectively. The decrease of $K(T)$ below T_c depends mainly on the size of the superconducting gap $\Delta(T)$ and on the symmetry of the pairing state. However, as has been shown recently by Sudbø et al. [72] the temperature dependence of K is influenced by details of the Fermi liquid theory thus making the conclusions of the analysis of the NMR data less straightforward.

In spite of the shortcomings we would like to point out some features of our ^{199}Hg NMR data which seem to support *d*-wave symmetry for the pairing state. Since no detailed calculations are available for our Hg1201 system we utilize the calculations performed for Y123 by Bulut and Scalapino [73] with a BCS value for the gap parameter $2\Delta_0 = 3.5 k_B T_c$ chosen to agree with recent electron tunneling measurements at $T = 4.2$ K [74]. As shown in Fig. 4.9 the experimental data are in much better agreement with the slower decrease of $K(T)$ with decreasing temperature predicted for a *d*-wave gap. However, the tunneling measurements in polycrystalline Hg1201 [74] yielded a range of gaps Δ from ~5 to 20

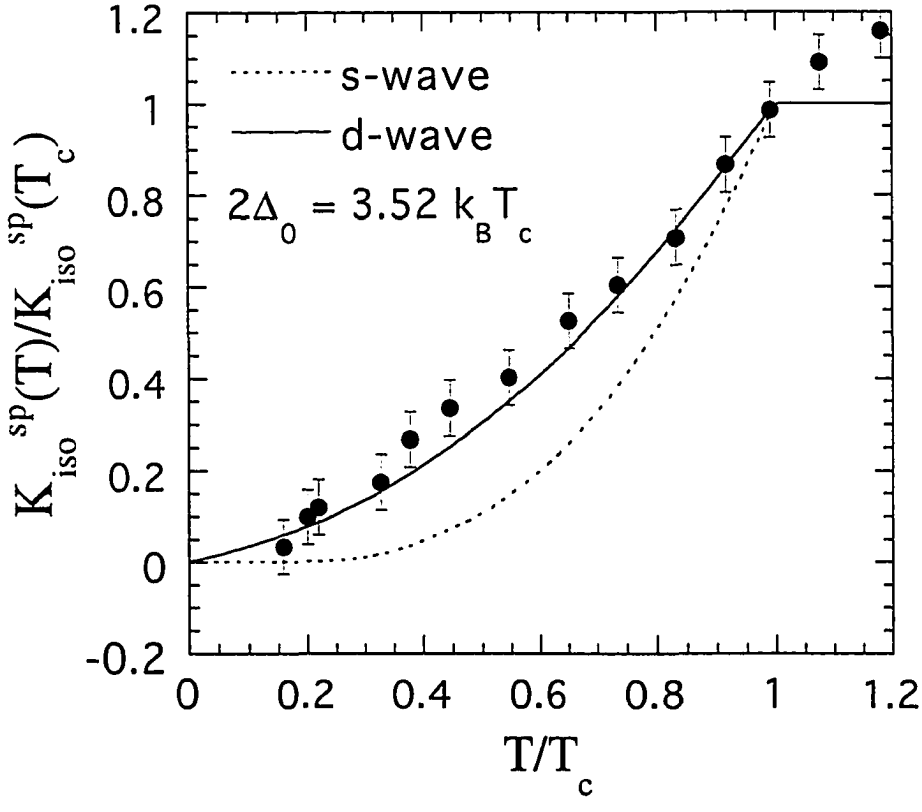

Fig. 4.9 Plot of the normalized ^{199}Hg K_{iso}^{sp} in the superconducting state: $K_{iso}^{sp}(T)/K_{iso}^{sp}(T_c)$ vs reduced T/T_c. The lines are theoretical behaviors predicted for *s*-wave pairing (dashed line) and *d*-wave pairing (solid line) with the same superconducting gap parameter $2\Delta_0 = 3.5k_BT_c$ [73].

meV, the origin of the spread being unknown. Thus it is conceivable that our Knight shift data could also be found to be consistent with an anisotropic *s*-wave gap in the *ab*-plane as shown for the NMR data in Y123 [72]. In the above discussion, the Knight shift data are not corrected for the local field due to diamagnetic magnetization and flux-lattice in the superconducting state. The amount of the correction is difficult to estimate due to lack of measurements of the magnetization M in high magnetic fields and to the uncertainty in the demagnetizing factors. It should be noted that correction, which is proportional to M, should be negligible for $\boldsymbol{H} \perp \boldsymbol{c}$ since for this orientation of the field the diamagnetic magnetization is small in these highly anisotropic superconductors. For $\boldsymbol{H} \parallel \boldsymbol{c}$, the correction would diminish the rate of decrease of K at low temperature, thus it should not affect the conclusions in favor of a *d*-wave pairing superconducting state.

The temperature dependence of the spin-lattice relaxation rate, T_1^{-1}, shown in Fig. 4.10, is also consistent with the *d*-wave pairing which predicts a T^3 temperature dependence of the NSLR below T_c [75]. As for the case of K discussed above, the conclusion for T_1^{-1} is also somewhat ambiguous due to the narrow temperature range in which the T^3 dependence is observed. The deviation from the T^3 dependence for $T < 40$ K and $\boldsymbol{H} \parallel \boldsymbol{c}$ is due to an extra contribution due to the vortex thermal motions not present for $\boldsymbol{H} \perp \boldsymbol{c}$ [see chapter 5]. The deviations from the T^3 dependence for $T < 20$ K and $\boldsymbol{H} \perp \boldsymbol{c}$ could be due to a non-zero residual density of states associated with lines of nodes in the gap function [76,77].

4.1.5 Summary and Conclusions

We have presented the ^{199}Hg NMR shift and relaxation rate data for a superconducting Hg1201 oriented powder sample. The main results are: (i) the very large anisotropic shift which is a consequence of the linear dumbbell Hg-O(2) bonding configuration, (ii) the linear relation between K_{iso}^{sp} and K_{ax}^{sp} supporting the single-spin

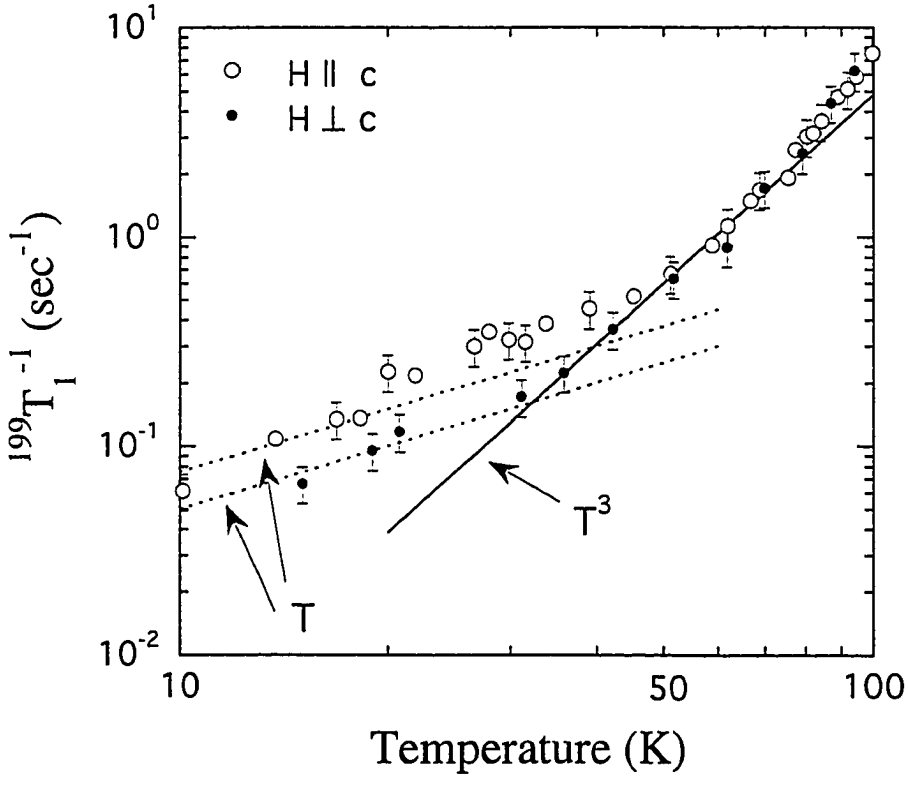

Fig. 4.10 Log-log plot of ^{199}Hg T_1^{-1} vs T in the superconducting state for two magnetic-field orientations: (o) $\boldsymbol{H} \parallel \boldsymbol{c}$ and (•) $\boldsymbol{H} \perp \boldsymbol{c}$. Lines are fits for T^3 dependence (solid line) and linear T dependence (dashed lines).

fluid picture, (iii) the normal Korringa relation between K^{sp} and T_1 which is valid in a wide temperature range including the superconducting region, and (iv) the same temperature dependence of K^{sp} and T_G^{-1}, suggesting that the indirect nuclear pseudo-dipolar or pseudo-exchange interaction is directly proportional to the uniform spin susceptibility.

Based on the above results which indicate that ^{199}Hg in Hg1201 is a good probe to study the Fermi liquid behavior, the electronic properties of Hg1201 have been investigated in both the normal and the superconducting state. The normal state is characterized by a decrease of the uniform spin susceptibility, $\chi'(0,0)$, with decreasing temperature starting above T_c. This normally signifies the opening of a spin pseudo-gap at $q = 0$. Both the temperature dependence of the Knight shift and of the NSLR below T_c are consistent with a superconducting state characterized by d-wave pairing with a gap parameter close to the BCS value, i.e. $2\Delta_0 = 3.5k_BT_c$.

The important conclusion here is that the ^{199}Hg NMR is found to be dominated by the interaction with the Fermi liquid, suggesting that the ^{199}Hg NMR in Hg-based HTSC can give direct information on the conduction carriers such as the density of states at the Fermi level. In this respect it is relevant to our finding that the Gaussian component in the spin-echo decay yields a parameter, T_G^{-1}, which appears to be due to an indirect nuclear interaction via the charge carriers. Thus T_G^{-1} can be used to measure directly the uniform spin susceptibility, $\chi'(0,0)$, of the Fermi liquid. Considering that all Hg-based compounds, $HgBa_2Ca_{n-1}Cu_nO_{2n+2+\delta}$, have only one Hg site and that the critical temperature, T_c, is very sensitive to the number of the CuO_2 layers and to the oxygen content (δ), the fact that ^{199}Hg is a good probe to study the Fermi liquid behavior encourages one to extend the ^{199}Hg NMR study systematically in Hg-based HTSC with different numbers of CuO_2 layers and oxygen contents δ [57].

4.2 Electronic and Magnetic Properties of YNi_2B_2C from ^{11}B and ^{89}Y NMR and Magnetic Susceptibility Measurements in Single Crystals

4.2.1 Introduction

The recently discovered superconductors, in the class of the quaternary intermetallic compounds RNi_2B_2C (R = Sc, Y, Th or a rare-earth element) [78-82], have received great attention due to their high superconducting transition temperature T_c (e.g. T_c = 16.6 K for R = Lu) compared with most other intermetallic compounds and due to the coexistence of superconductivity and magnetic ordering below T_c for the compounds containing a magnetic rare earth element R = Ho, Er, Tm [79] or Dy [82].

In addition, the relatively high T_c together with the structure [83] consisting Ni_2B_2 layer blocks similar to the CuO_2 units in HTSC has raised the possibility of comparing the role of the transition metal ion in both kinds of superconductors. Since Ni metal is an itinerant ferromagnet in elemental form, one wonders whether the Ni layers have magnetic character similar to the Cu layer in HTSC. In fact, several NMR experiments [84-87] have been reported, which claim the possible existence of localized or itinerant electron spin fluctuations/correlations in the compounds YNi_2B_2C and $LuNi_2B_2C$ although electronic band calculations [88-90] indicate that these compounds are characterized as conventional BCS-type superconductors.

In order to clarify the existence of magnetic character on Ni sublattice, and if so, its role in this system, we have performed a careful NMR measurement in high quality YNi_2B_2C samples prepared at Ames Laboratory by B. K. Cho and P. C. Canfield [91,92]. In this chapter, we present the ^{11}B and ^{89}Y NMR and relaxation measurements both in a powder sample and in single crystals. Magnetization measurements have been also performed by B. K. Cho to obtain macroscopic information on the magnetic susceptibility

and the results are compared with the Knight shifts. A theoretical calculation (performed at Ames Laboratory by J. Y. Rhee) of the Van Vleck susceptibility which is in agreement with our experimental results is also presented.

We would like to emphasize that the ^{11}B Knight shift and/or relaxation rates measurements are particularly suitable to investigate the role of the Ni ion in the electronic and magnetic properties due to the local symmetry of the boron site in the crystal structure and the short distance between Ni and B [83].

4.2.2 Experimental Details

The quaternary intermetallic compound samples with $T_c = 15.5$ K were prepared at Ames Laboratory by B. K. Cho and P. C. Canfield using the method described in detail elsewhere [91,92]. ^{11}B and ^{89}Y NMR measurements were performed in a powder and a stack of single-crystal plates of YNi_2B_2C with an approximate total volume of 10×4×1 mm^3. The typical size of a single plate in the stack was approximately 3.5×3.5×0.3 mm^3. The measurements were performed both in the normal and in the superconducting state with a pulse Fourier transform (FT) spectrometer in external fields of 1.2 T, 2.4 T and 8.2 T. In particular, an accurate investigation of the normal state was made on the single crystals in an Oxford Instruments superconducting magnet of 8.2 Tesla with field inhomogeneity less than 0.1 Gauss over the sample dimension operating at 112 MHz and 17.1 MHz for ^{11}B and ^{89}Y, respectively. The ^{11}B ($I = 3/2$) NMR shifts of the central line were measured on two orientations of magnetic field, $\boldsymbol{H} \parallel \boldsymbol{c}$ and $\boldsymbol{H} \perp \boldsymbol{c}$, with respect to the resonance frequency in H_3BO_3 aqueous solution. The ^{11}B nuclear spin-lattice relaxation rates (NSLR's) were measured using a single-pulse saturation method, described in section 2.2. The ^{89}Y ($I = 1/2$) Knight shifts measurements were performed on the single crystals with respect to a YCl_3 aqueous solution for the two orientations of the magnetic field with respect to the crystal axes. On the other hand, the ^{89}Y NSLR's were measured only in the

powder sample with irradiation at the resonance frequency of the singularity corresponding to the resonance for the condition $\boldsymbol{H} \perp \boldsymbol{c}$. This choice is dictated by the poor signal to noise ratio in the stacked single crystals due to the limited penetration of the radio frequency in the bulk of the sample and the small filling factor of the single-crystal plates.

Magnetization measurements on a single crystal were carried out (by B. K. Cho) using a Quantum Design SQUID magnetometer for both field orientations in the normal state. Non-vanishing magnetization $M_0(T)$ at $H = 0$ was obtained from the extrapolation of the linear $M(H)$ data for $1\text{T} \leq H \leq 5\text{T}$ to $H = 0$ at each temperature, tentatively attributed to ferromagnetic impurities and equivalent to ≈6.5 at. ppm of iron metal impurities with respect to Ni; the data in Fig. 4.14 below are corrected for this contribution.

4.2.3 Experimental Results

4.2.3.1 ^{11}B and ^{89}Y NMR Spectra

The ^{11}B NMR spectrum is shown in Fig. 4.11 at room temperature measured both in a powder sample and single crystals. As shown in Fig. 4.11(b) both the central line (+1/2 ↔ -1/2 transition) and the satellite transitions (+3/2 ↔ +1/2 and -3/2 ↔ -1/2 transitions) are relatively narrow (about 6 kHz) for both orientations of the magnetic field, $\boldsymbol{H} \parallel \boldsymbol{c}$ and $\boldsymbol{H} \perp \boldsymbol{c}$. This circumstance indicates that the single crystals are free of structural defects and that the alignment of the different crystals stacked with a common crystallite c axis is very good.

The separation of the satellite transitions in first order perturbation theory obeys the simple relation derived from Eq. (2.11):

$$\Delta\nu = \frac{\nu_Q}{2}\left[3\cos^2(\theta) - 1\right], \tag{4.7}$$

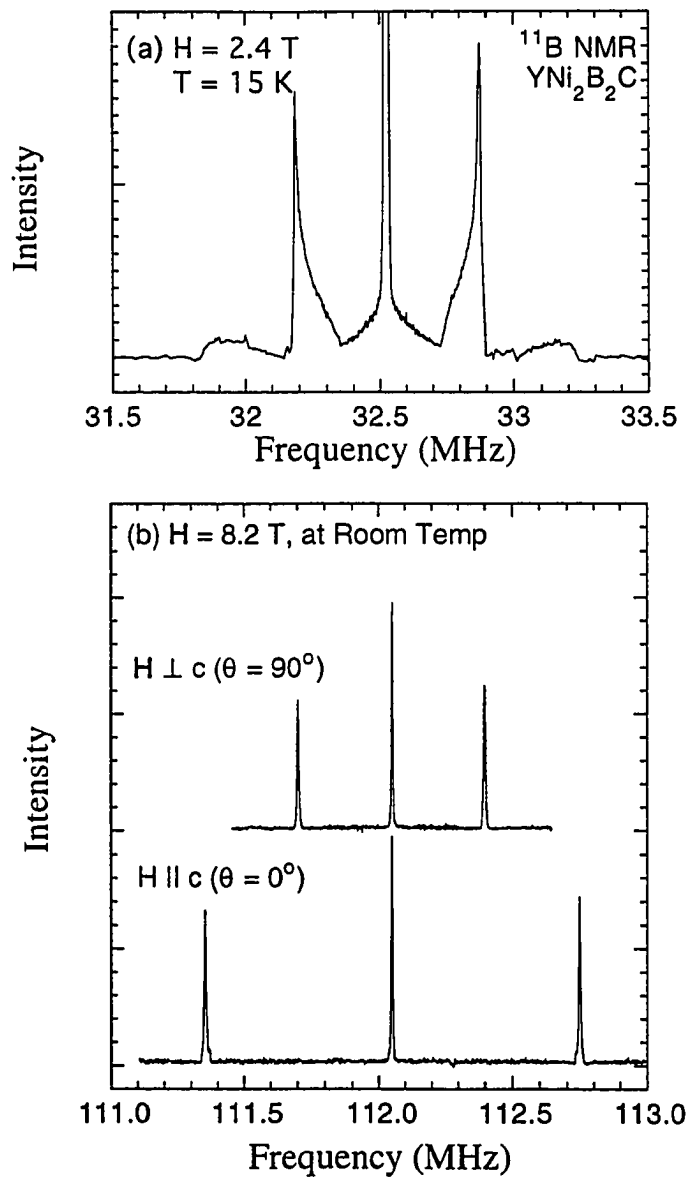

Fig. 4.11 Representative ^{11}B NMR spectra in YNi_2B_2C: (a) in a powder sample, and (b) in stacked single crystals.

where the quadrupole coupling frequency is defined as $\nu_Q = e^2qQ/2h$ in terms of the nuclear quadrupole moment Q and of the largest component q of the axially symmetric electric field gradient. From the spectrum in Fig. 4.11 one derives $\nu_Q = 698\pm1$ kHz at room temperature. No measurable change of the quadrupole interaction could be observed from 300 K down to 15 K, indicating the absence of structural changes in this temperature range. It is noted that for $\boldsymbol{H} \parallel \boldsymbol{c}$ the position of the central line is not affected by quadrupole interactions while for $\boldsymbol{H} \perp \boldsymbol{c}$ the position of the central line is shifted by second order quadrupole effects as: $\nu_\perp = \nu_0 + 3\nu_Q^2/16$, where ν_L is the Larmor frequency in Hz. Thus in order to measure the Knight shift at $H = 8.2$ Tesla ($\nu_L = 112$ MHz) for the perpendicular orientation, $\boldsymbol{H} \perp \boldsymbol{c}$, we subtracted 815 Hz from the observed resonance frequency.

The full width at half maximum of the central line is plotted in Fig. 4.12 as a function of temperature for the two field orientations. At room temperature the NMR is inhomogeneously broadened as indicated by the presence of a spin echo following a $\pi/2$ - π pulse sequence. The temperature dependence, which becomes pronounced below 100 K, is a clear indication of a broadening mechanism associated with a random distribution of localized magnetic moments. The effect will be discussed further on in connection with the susceptibility measurements.

The ^{89}Y NMR spectrum at room temperature is shown in Fig. 4.13. The upper trace represents the powder pattern in a polycrystalline sample with the singularity corresponding to crystallites oriented with $\boldsymbol{H} \perp \boldsymbol{c}$ and the step corresponding to $\boldsymbol{H} \parallel \boldsymbol{c}$. The lower trace represents the NMR spectra in the single crystal for the two orientations of the magnetic field with respect to the c axis. The excellent correspondence on the frequency scale of the single crystal signal and of the singularities in the powder pattern is remarkable.

4.2.3.2 Magnetic Susceptibility Measurements

The experimental data for the magnetic susceptibility χ as functions of temperature and field orientation are shown in Fig. 4.14(a) where the data are corrected for the tentative contribution of small amount of ferromagnetic impurities (equivalent to about 6.5 at. ppm

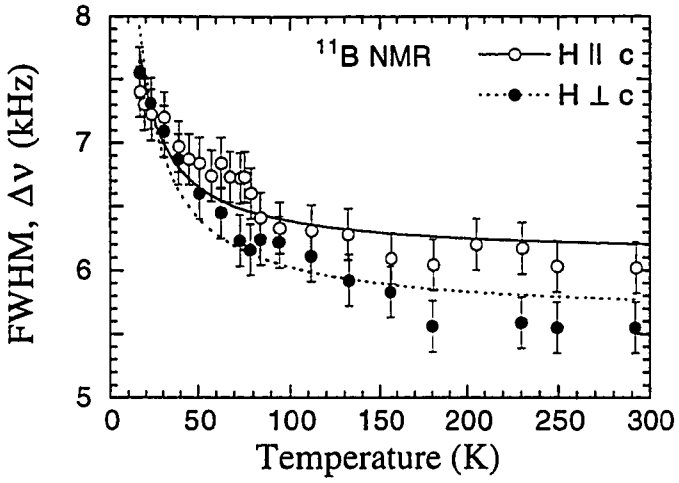

Fig. 4.12 ^{11}B NMR linewidth, $\Delta\nu$, of the central lines vs temperature in YNi_2B_2C for two magnetic fields orientation with respect to the crystal c axis for $H = 8.2$ T. The curves are fits according to $\Delta\nu = \Delta\nu_0 + P\,\chi^{imp}$ (see the text for details).

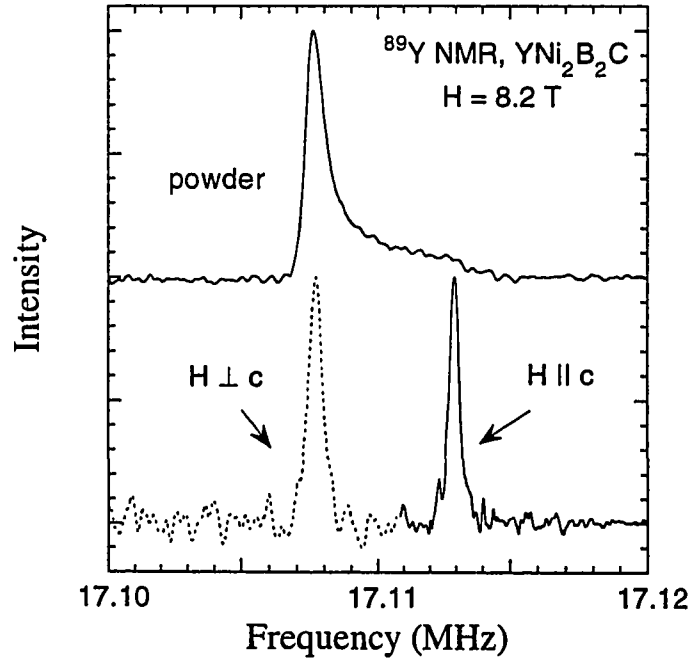

Fig. 4.13 ^{89}Y NMR spectra in YNi_2B_2C for $H = 8.2$ T: The upper trace is the spectrum in a powder and the lower traces are the spectra in stacked single crystals.

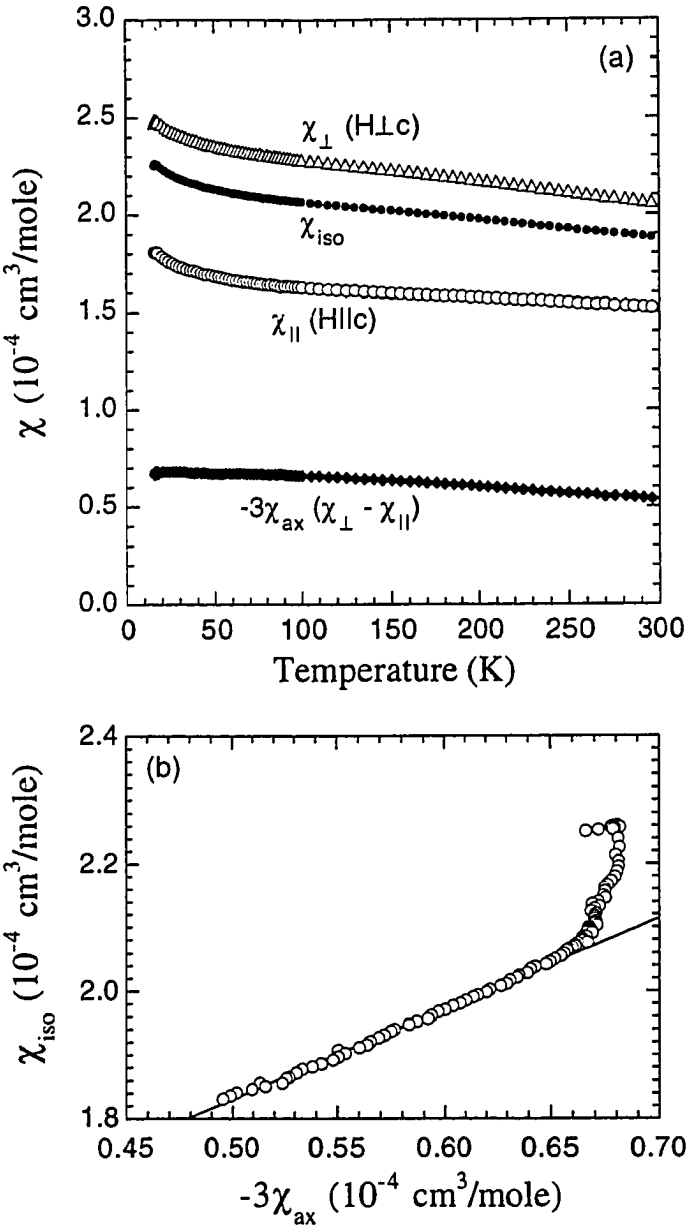

Fig. 4.14 (a) Magnetic susceptibility, χ, vs temperature in a YNi_2B_2C single crystal for two magnetic field orientations. (b) The isotropic component (χ_{iso}), vs the anisotropic component ($-3\chi_{ax} \equiv \chi_\perp - \chi_{||}$) of the susceptibility. (Courtesy of B. K. Cho)

of metallic Fe with respect to Ni). The main features are the quite large anisotropy of the susceptibility, $\chi_{\perp} - \chi_{\parallel}$ (= $-3\chi_{ax}$), and the considerable temperature dependence of both the isotropic component $\chi_{iso} = (\chi_{\parallel} + 2\chi_{\perp})/3$ and the anisotropic component, $-3\chi_{ax} = \chi_{\perp} - \chi_{\parallel}$. A weak Curie-type increase at low temperature (< 50 K) is observed for χ_{iso} but not for χ_{ax}. This effect is tentatively attributed to a small amount of localized magnetic moments which could be paramagnetic impurities. The separation of the different terms contributing to the total susceptibility, i.e. the spin susceptibility of the conduction electrons, the orbital and diamagnetic contributions and a possible contribution from a small amount of localized magnetic moments, will be attempted in section 4.2.4 by an analysis of the susceptibility data combined with the ^{11}B Knight shift data.

4.2.3.3 ^{89}Y Knight Shifts and Nuclear Spin-Lattice Relaxation Rates (NSLR's)

The temperature dependences of the ^{89}Y Knight shifts in stacked single crystals and a powder sample are shown in Fig. 4.15 for the two orientations of the external magnetic field with respect to the tetragonal *c* axis. The data are not corrected for the demagnetization effects. The difference between the $K_{\perp}$'s in stacked single crystals and the powder sample indicates the demagnetization effects are not negligible. Since the shifts are relatively small the correction due to demagnetization effects is not negligible and will be applied by writing [12]:

$$K^m(T) \equiv \frac{\nu_m - \nu_L}{\nu_L} = K(T) + 4\pi\left(\frac{1}{3} - D\right)\chi, \qquad (4.8)$$

where D is the demagnetization factor and χ is the measured magnetic susceptibility. $K^m(T)$ is the measured shift shown in Fig. 4.15 while $K(T)$ is the correct Knight shift value. It is noted that χ in Eq. (4.8) is in dimensionless volume units and is obtained from the molar susceptibility data in Fig. 4.14 by multiplying by d/M with M = 239.9 g/mole being the molar mass and d = 6.09 g/cm^3 the mass density of YNi_2B_2C.

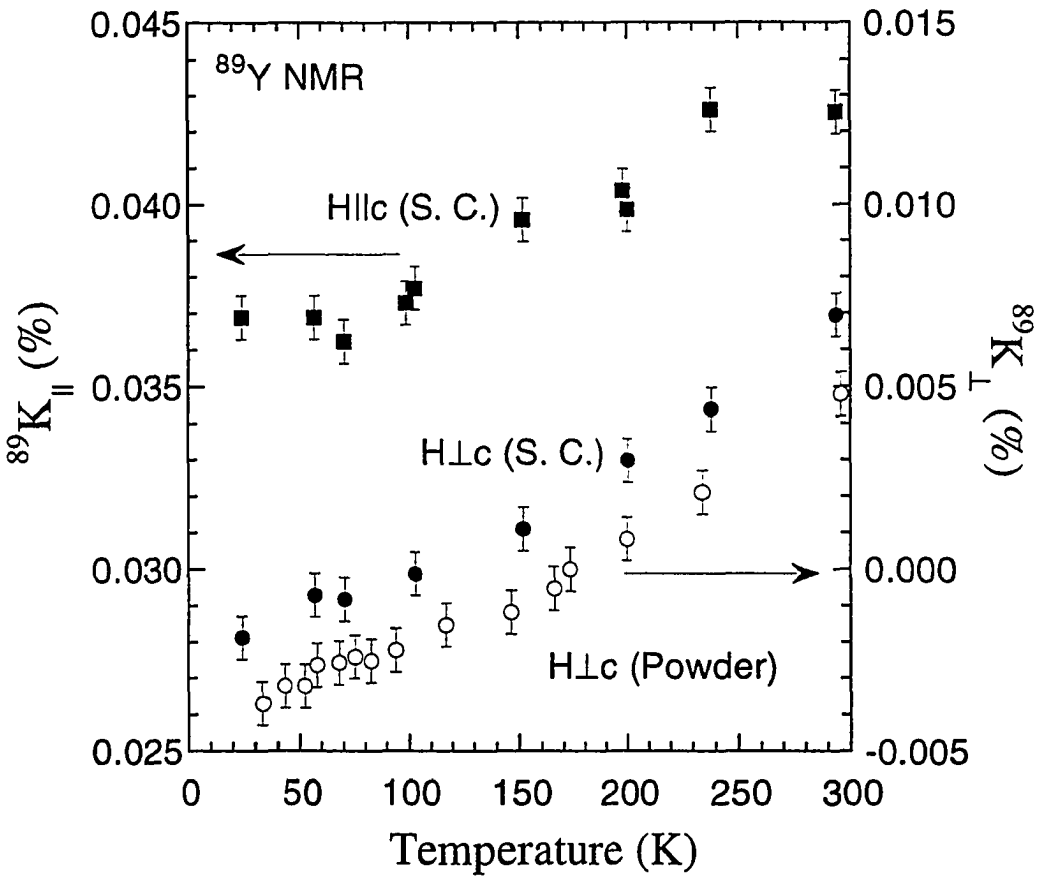

Fig. 4.15 ^{89}Y Knight shift, ^{89}K, vs temperature in YNi_2B_2C: Solid symbols denote (■) $^{89}K_{||}$ ($\boldsymbol{H} \parallel \boldsymbol{c}$) and (•) $^{89}K_{\perp}$ ($\boldsymbol{H} \perp \boldsymbol{c}$), respectively in stacked single crystals. Open circle (o) denotes the shift of the resonance frequency of the singularity in the spectrum of the powder sample (see Fig. 4.13). The singularity is from the grains in a powder whose crystal orientation satisfies the condition, $\boldsymbol{H} \perp \boldsymbol{c}$.

By using the values of the volume susceptibility χ and assuming $D_\perp = 1/3$ for a powder sample, we find the average value of $D_\perp = 0.06 \pm 0.02$ to match the $K_\perp$'s in single crystals and in a powder sample. This value is in good agreement with the estimated value of $D_\perp = 0.054$ from the ellipsoidal approximation [93] of the average dimensions $3.5 \times 3.5 \times 0.3$ mm^3 of the single crystal plate. Assuming $D_a = D_b = D_\perp$ and using the relation $D_a + D_b + D_c = 1$, we extract $D_\parallel = D_c = 0.88$. Here the factors of 0.88 and 0.06 take into account the deviations from the ideal thin slab geometry of our samples. The Knight shifts, corrected according to Eq. (4.8) using the experimental values of the volume magnetic susceptibility are shown in Fig. 4.16(a). The quantities plotted in Fig. 4.16(b) are the isotropic (K_{iso}) and anisotropic (K_{ax}) components of the Knight shift tensor as defined in section 2.2. It is worth noting that the anisotropic part of the Knight shift is temperature independent and the isotropic part decreases with decreasing temperature.

The ^{89}Y NSLR results are shown in Fig. 4.17. Since the measurements had to be performed in the powder sample, no firm information about the anisotropy of the relaxation is available. The data in Fig. 4.17 were collected by irradiating at the frequency of the singularity in the NMR powder spectrum of Fig. 4.13 and thus refer mainly to the condition $\boldsymbol{H} \perp \boldsymbol{c}$. However, since the spectral width of the radio frequency pulse also partly covers nuclei in crystallites with different orientations, one would expect to see some non-exponentiality in the recovery of the nuclear magnetization if the NSLR were strongly anisotropic. Since the recovery was found to be exponential one can deduce that the anisotropy of the NSLR, if present at all, should be small relative to the isotropic component.

4.2.3.4 ^{11}B Knight Shift and Nuclear Spin-Lattice Relaxation Rates (NSLR)

The ^{11}B Knight shift results are shown as a function of temperature and orientation of the external magnetic field in Figs. 4.18(a)-(c) where the corrections for the 2nd order quadrupole effect for $\boldsymbol{H} \perp \boldsymbol{c}$ and for the demagnetization effects have been done in the same way as described above for the ^{89}Y Knight shift. It is noted that, contrary to the results for

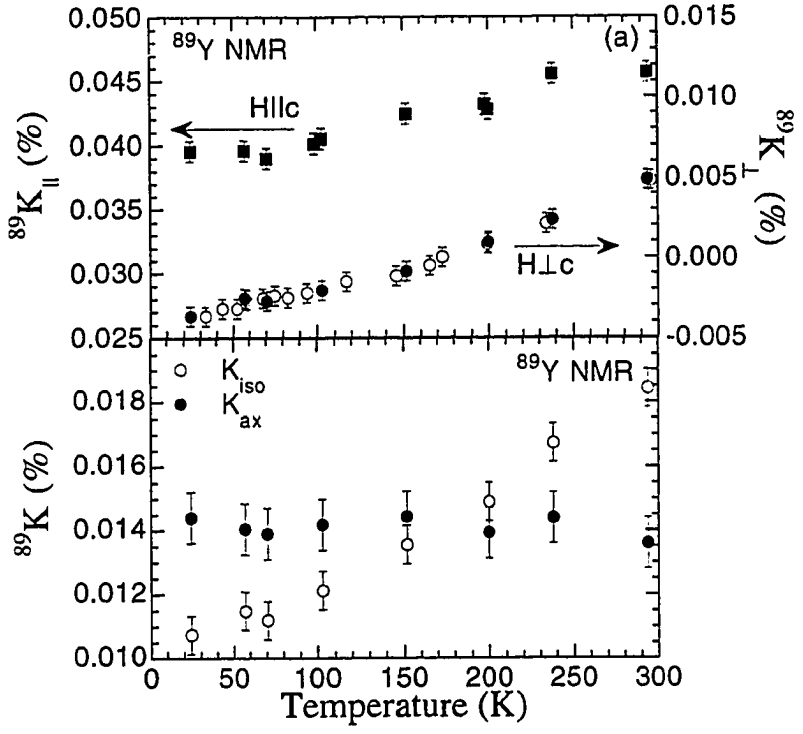

Fig. 4.16 Plots of the ^{89}Y Knight shift components in YNi_2B_2C: (a) $^{89}K_{\parallel}$ ($H \parallel c$) and $^{89}K_{\perp}$ ($H \perp c$) vs T, and (b) $^{89}K_{iso}$ and $^{89}K_{ax}$ vs T. The data are corrected for the demagnetization effects (see the text).

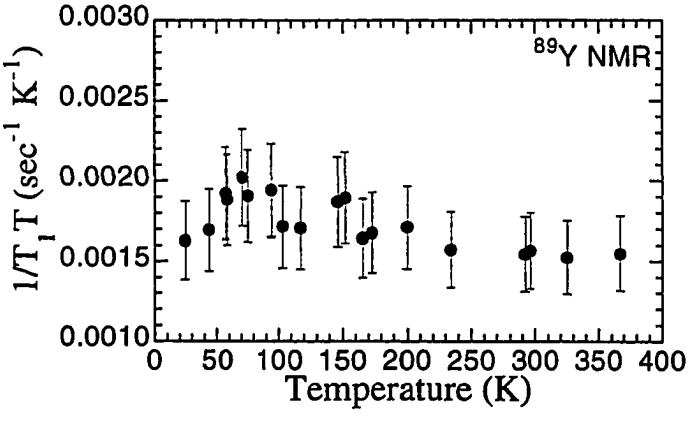

Fig. 4.17 Temperature dependence of $(T_1T)^{-1}$ of ^{89}Y in YNi_2B_2C powder.

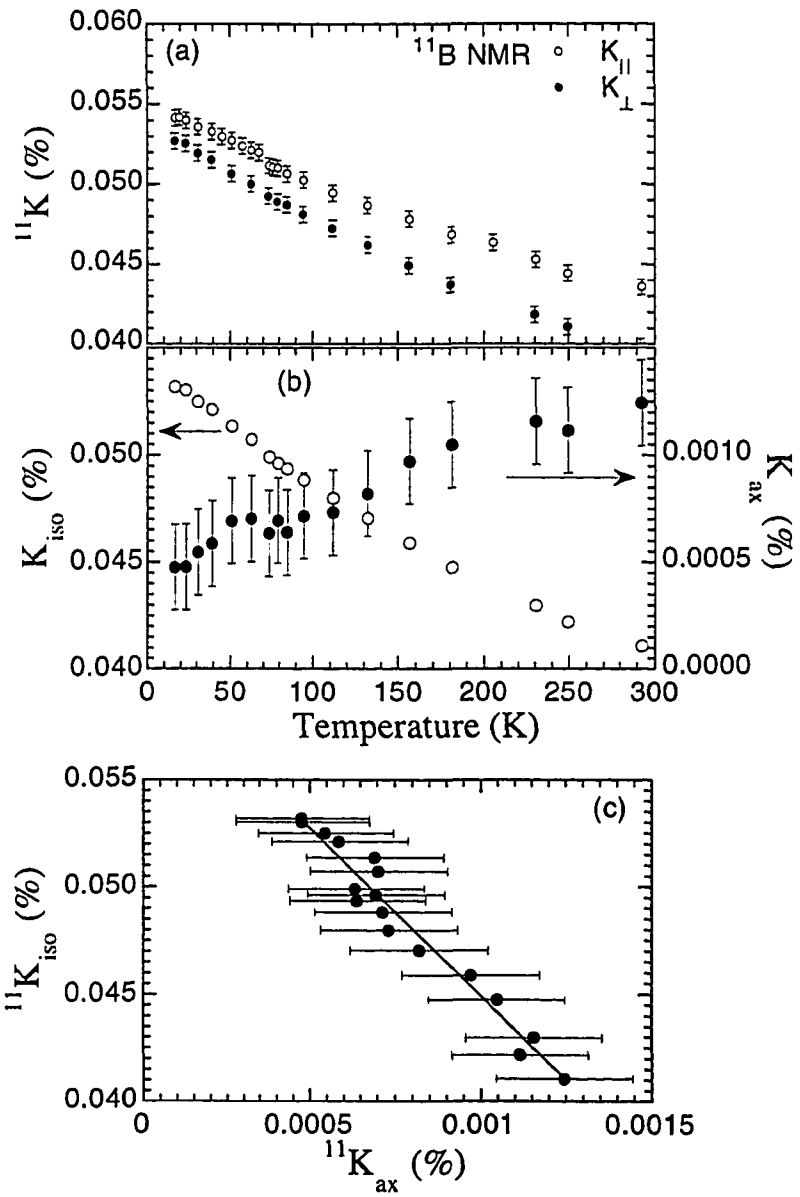

Fig. 4.18 Plots of the ^{11}B Knight shift components of the central line in stacked YNi_2B_2C single crystals: (a) $^{11}K_{\|}$ ($H \| c$) and $^{11}K_{\perp}$ ($H \perp c$) vs T, (b) $^{11}K_{iso}$ and $^{11}K_{ax}$ vs T, and (c) $^{11}K_{iso}$ vs $^{11}K_{ax}$. The data are corrected for the 2nd order quadrupole and the demagnetization effects (see the text).

^{89}Y shown in Fig. 4.16(b), the anisotropic part of the ^{11}B Knight shift is more than one order of magnitude smaller than the isotropic part and both display a sizable temperature dependence. In addition, contrary to the relation between χ_{iso} and $-3\chi_{ax}$ in Fig. 4.14(b), a linear relation between the $^{11}K_{iso}$ and $^{11}K_{ax}$ in whole temperature range investigated was found as shown in Fig. 4.18(c).

The ^{11}B NSLR's are shown in Fig. 4.19 as a function of temperature and for the two orientations of the external magnetic field with respect to the tetragonal *c* axis. The remarkable feature is that no measurable anisotropy of the NSLR is present, in contrast with both the susceptibility and the Knight shift results shown in Figs. 4.14 and 4.18, respectively.

4.2.4 Discussion

4.2.4.1 Knight Shift and Spin Susceptibility

The anisotropic and temperature dependent data for the ^{11}B Knight shift can be analyzed in conjunction with the susceptibility measurements to extract, under reasonable assumptions, the magnitude, anisotropy and temperature dependence of the uniform spin susceptibility of the Fermi liquid in the normal state of YNi_2B_2C.

The measured susceptibility χ^{meas} can be partitioned into spin (χ^{sp}) and orbital (χ^{orbit}) terms as:

$$\chi^{meas} = \chi^{sp} + \chi^{orbit} = \chi^{sp} + \chi^{Landau} + \chi^{core} + \chi^{VV}, \qquad (4.9)$$

where χ^{VV} is the paramagnetic Van Vleck orbital contribution and χ^{Landau} is the diamagnetic Landau orbital contribution due to conduction electrons, both assumed to be temperature independent, while the Pauli spin susceptibility, χ^{sp}, can be temperature

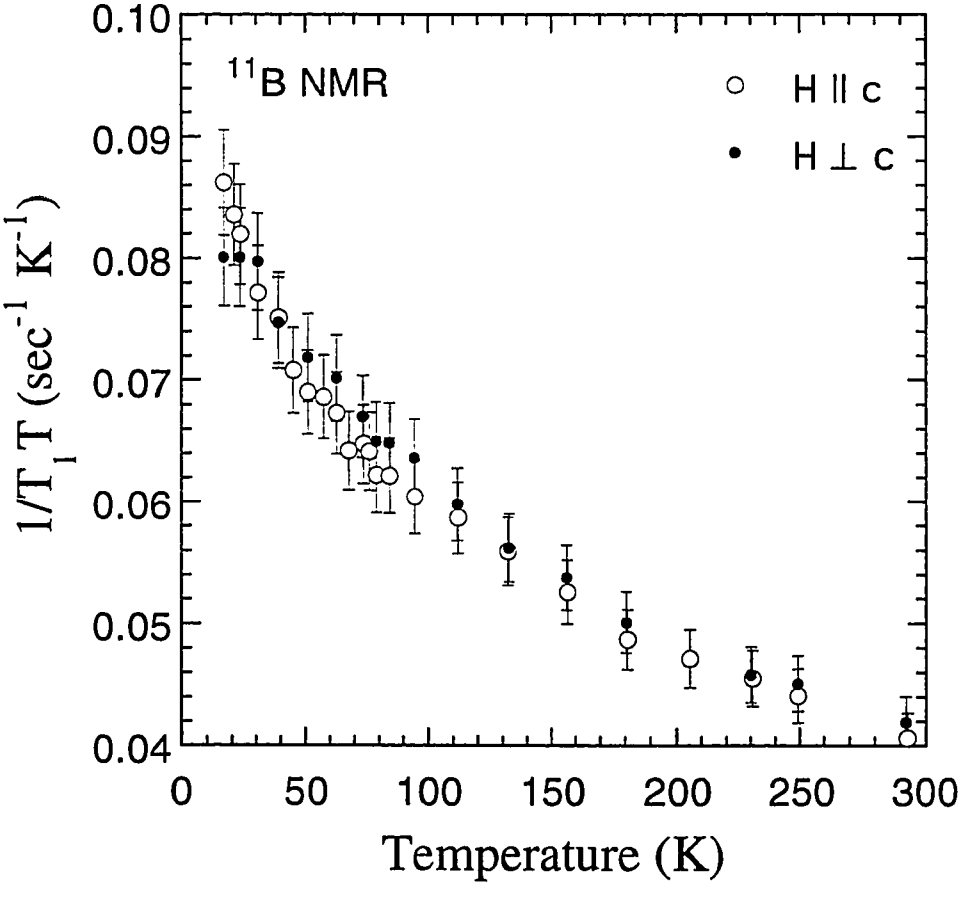

Fig. 4.19 Temperature dependence of $(T_1T)^{-1}$ of ^{11}B in stacked YNi_2B_2C single crystals for $H = 8.2$ T for two magnetic field orientations.

dependent in case of a narrow *d*-band [12]. The contribution to the core diamagnetism by the various ions can be estimated (in cm^3/mole) as [94]:

$$\chi^{core}(Y^{3+}) = -12\times10^{-6}; \qquad \chi^{core}(Ni^{2+}) = -12\times10^{-6};$$
$$\chi^{core}(B^{3+}) = -0.2\times10^{-6}; \qquad \chi^{core}(C^{4+}) = -0.1\times10^{-6}. \tag{4.10}$$

In a similar way we partition the Knight shift as:

$$K = K^{sp} + K^{orbit} = A\chi^{sp} + B\chi^{VV}, \tag{4.11}$$

where the term $A\chi^{sp}$ can contain different contributions: an isotropic contribution from the contact hyperfine interaction averaged over the *s*-wave function of the conduction electrons at the Fermi level, an anisotropic contribution from the dipolar interaction mediated by *p*-like and *d*-like wave functions of the conduction electrons and an isotropic core polarization term due to the interaction of core *s*-electrons with polarized *d*-like conduction electrons.

First we argue that the measured susceptibility must include a small contribution from randomly distributed localized moments. This could arise either from paramagnetic impurities in the sample or from a small percentage of localized Ni moments in the proximity of defects. The conclusion is based on the increase of the ^{11}B inhomogeneous linewidth below 100 K (see Fig. 4.12) and the corresponding upturn of the susceptibility shown in Fig. 4.14. Also the deviation at low temperature from the linear relationship of the χ_{iso} vs $3\chi_{ax}$ plot in Fig. 4.14(b) is a clear indication of an paramagnetic term which contributes to χ_{iso} but not to $3\chi_{ax}$. On the other hand the Knight shift shown in Fig. 4.18(a) does not track the linewidths (Fig. 4.12) and the susceptibilities [Fig. 4.14(a)] below 100 K as expected; a random distribution of paramagnetic moments is expected to broaden the line without affecting the shift of the center of the line, as observed. It is noted that we can rule out the possibility that the anomalous increase in χ_{iso} below $\approx$ 50 K could arise from a

small magnetic moment localized at each Ni site. In such a case one would expect a dipolar contribution to the ^{11}B Knight shift through K_{ax} but not K_{iso} (for the symmetry location of B with respect to Ni), contrary to the experimental observation that $^{11}K_{iso}$ and $^{11}K_{ax}$ scale linearly with each other in the whole temperature range investigated as seen in Fig. 4.18(c).

In order to determine the small contribution χ^{imp} due to paramagnetic impurities, we have plotted in Fig. 4.20 the difference between the experimental data and the large background intrinsic susceptibility of the isotropic component χ_{iso}. The intrinsic background susceptibility was obtained by extrapolating the linear relation between χ_{iso} and $-3\chi_{ax}$ ($= \chi_{\perp} - \chi_{\parallel}$) obtained from the data above 150 K [see Fig. 4.14(b)]. Thus the data in Fig. 4.20 should represent the contribution from paramagnetic impurities. The impurity contribution to the total susceptibility determined with the above procedure is:

$$\chi^{imp} \cong \frac{3.1\ (10^{-4}\ \mathrm{cm^3 K / mole})}{T(\mathrm{K}) + 0.5\ \mathrm{K}} \quad . \tag{4.12}$$

Only the data below 50 K, where the impurity contribution becomes important, were utilized to obtain the result (4.12). It is noted that the broadening of the ^{11}B NMR line shown in Fig. 4.12 is consistent with the presence in the susceptibility of the Curie-Weiss term of Eq. (4.12) due to randomly distributed paramagnetic moments. In fact, if we write for the linewidth $\Delta\nu = \Delta\nu_0 + P\chi^{imp}$ we get good fits of the data in Figure 4.12 with $\Delta\nu_0 =$ 6.1 kHz and $P = 0.9\times10^5$ kHz mole/cm^3 for $\boldsymbol{H} \parallel \boldsymbol{c}$ and $\Delta\nu_0 = 5.6$ kHz and $P = 1.3\times10^5$ kHz mole/cm^3 for $\boldsymbol{H} \perp \boldsymbol{c}$, respectively

The ^{11}B Knight shift is plotted in Fig. 4.21 as a function of χ^{core}, the susceptibility corrected by subtracting the impurity contribution given by Eq. (4.12). Since the temperature dependence of K must arise entirely from the temperature dependence of the spin susceptibility one obtains the hyperfine constant A in Eq. (4.11) directly from the slope of the linear plot of $K(T)$ vs χ^{corr} [see Figs. 4.21(a), (b)]:

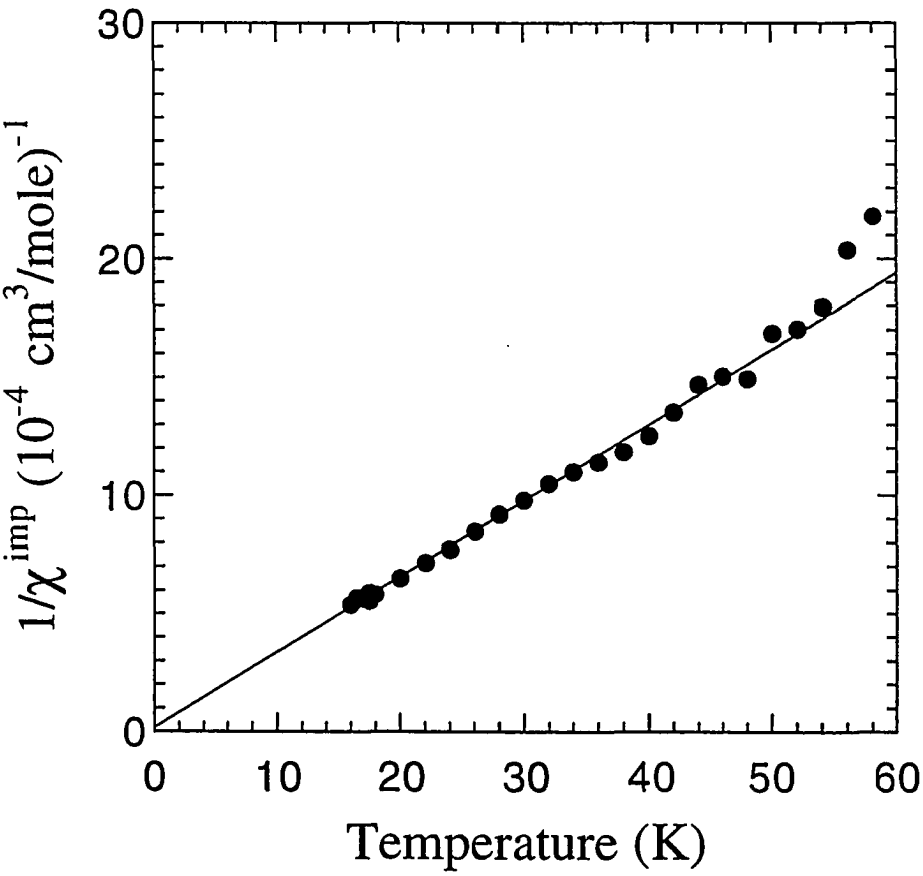

Fig. 4.20 Contribution of paramagnetic impurities to the susceptibility: $(\chi_{imp})^{-1}$ vs T.

$$^{11}A_{\parallel} = (9.3 \pm 0.7)\ \text{mole/cm}^3; \qquad ^{11}A_{\perp} = (6.8 \pm 0.7)\ \text{mole/cm}^3. \qquad (4.13)$$

Since ^{11}B is a light nucleus without *d*-electrons in the core of the atom it is reasonable to neglect the orbital contribution to the Knight shift from the Van Vleck susceptibility [B = 0 in Eq. (4.11)] and any core polarization contribution from the spin susceptibility [12]. Thus we can use the experimental Knight shift data in Fig. 4.18(a) with the above hyperfine constants to evaluate the spin susceptibility according to Eq. (4.11). The results are plotted in Fig. 4.22. The average spin susceptibility extrapolated to the zero temperature is $\chi_{iso} = (\chi_{\parallel} + 2\chi_{\perp})/3 = 0.74\times10^{-4}$ cm^3/mole. This value can be compared with the value estimated theoretically from electronic band structure calculations performed by Rhee (see below): $\chi^{theory} = 1.25\times10^{-4}$ cm^3/mole [$N(E_F)$ = 3.95 states/eV f.u., where "f.u." is a fomular unit of YNi_2B_2C]. The anisotropy of the spin susceptibility is a significant fraction of the total anisotropy in Fig. 4.14(a) and is temperature dependent. The remaining temperature independent anisotropy must arise from χ^{VV} in Eq. (4.9), discussed below. Since the theoretical value for the spin susceptibility appears well founded and obtained by different authors, we have to address the problem that our experimental estimate is $\cong$ 40 % smaller than the theoretical value. Since the Stoner enhancement factor, when included, can only raise the theoretical estimate one is left with possibility that our experimental estimate is too small. One possible reason for underestimating the spin susceptibility from our Knight shift results is following. In Eq. (4.11) we have assumed that the Knight shift of ^{11}B in YNi_2B_2C reflects the total spin susceptibility. This may not be the case here since most of the spin susceptibility comes from the *d*-electron spins at Ni sites. (In fact we found that the ^{11}B K in YNi_2B_2C reflects only the spin susceptibility due to the *s*-electron spins at B sites, we added a note in the end of this section for more detail explanations.)

We turn now to the ^{89}Y Knight shift. From the data in Fig. 4.16 one can see that the anisotropic part of the Knight shift, K_{ax}, is temperature independent to within experimental error of $\approx \pm$ 7 %. Since the anisotropy in the spin susceptibility in Fig. 4.22 varies by a

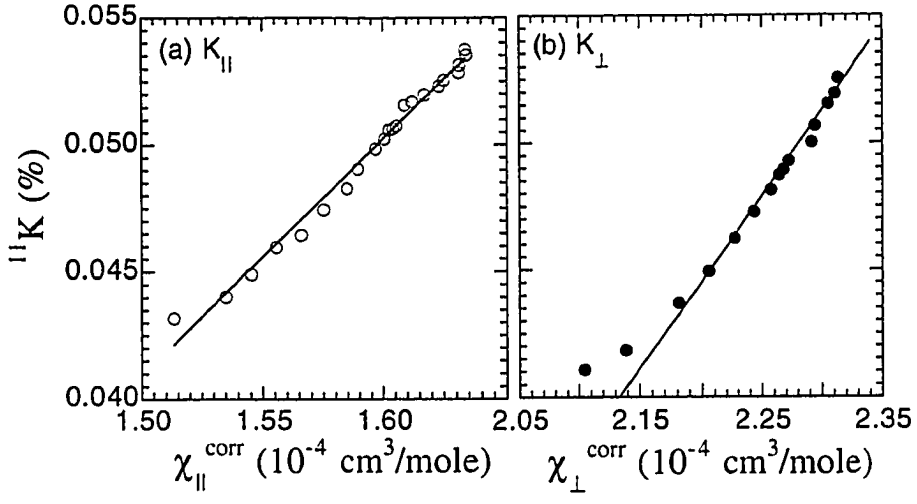

Fig. 4.21 ^{11}B K vs the magnetic susceptibility, χ^{corr}, corrected for the effects of paramagnetic impurities (see the text): (a) for $H \parallel c$ and (b) for $H \perp c$. The lines are fits using Eq. (4.10), yielding $^{11}A_{||} = 9.3 \pm 0.7$ cm^{-3} and $^{11}A_{\perp} = 6.8 \pm 0.7$ cm^{-3}.

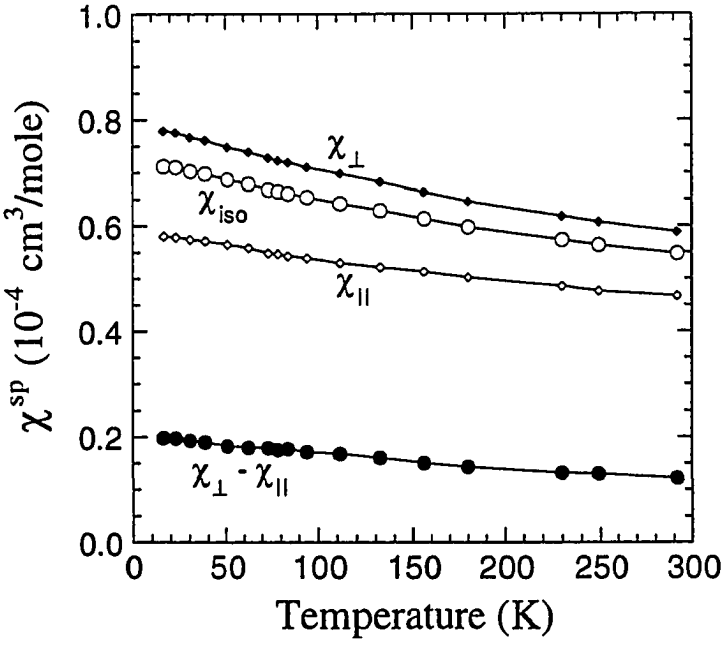

Fig. 4.22 Plots of the spin-susceptibility components vs T in YNi_2B_2C single crystal.

factor of two between 300 K and 16 K, we may ascribe the anisotropy entirely to the orbital contribution in Eq. (4.11), i.e.

$$3(K^{orb})_{ax} = K_{\parallel}^{orb} - K_{\perp}^{orb} \cong 0.042\ \%\ . \tag{4.14}$$

In order to separate the isotropic contribution to the shift coming from the orbital and spin susceptibilities we plot in Fig. 4.23 the measured $^{89}K_{iso}$ in Fig. 4.16(b) as a function of the isotropic spin susceptibility χ_{iso} derived previously from the ^{11}B Knight shift data. Then by assuming

$$K_{iso} = K_{iso}^{orb} + {}^{89}A\chi_{iso}(T)\ , \tag{4.15}$$

we derive from the plot in Fig. 4.23:

$$K_{iso}^{orb} = 0.043 \pm 0.01\ \%; \qquad {}^{89}A = -4.7 \pm 0.8\ \text{cm}^{-3}\ , \tag{4.16}$$

where the large uncertainties are due to the weak signal to noise ratio of the ^{89}Y NMR.

4.2.4.2 Separation of the Magnetic Susceptibility into Different Contributions

The different contributions to the measured susceptibility according to Eq. (4.9) are summarized in Fig. 4.24 for both orientations of the external magnetic field. The spin contribution, χ^{sp}, and the paramagnetic-impurities term, χ^{imp}, were obtained in the above Fig. 4.22 and Eq. (4.12), respectively. The orbital contribution includes different terms:

$$\chi^{orbit} = \chi^{Landau} + \chi^{core} + \chi^{VV}. \tag{4.17}$$

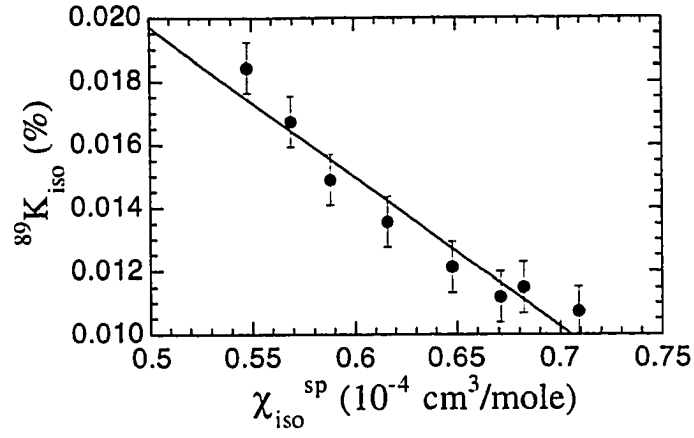

Fig. 4.23 ^{89}Y K_{iso} vs χ_{iso}^{sp} in YNi_2B_2C. The line is a linear fit using Eq. (4.12), yielding ^{89}A = -4.7 ± 0.8 cm^{-3} and $^{89}K_{iso}^{orb}$ = 0.043 ± 0.01 %.

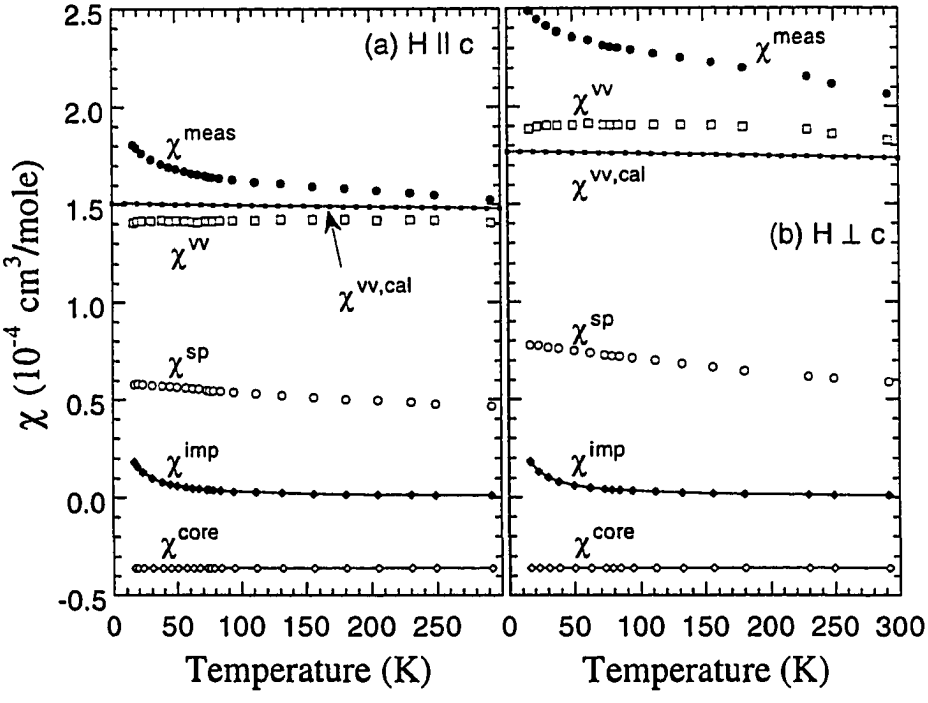

Fig. 4.24 Separation of the measured magnetic susceptibility in different contributions in YNi_2B_2C single crystal: Estimated value of each contribution is plotted as a function of temperature for two orientations. The calculated values of the Van Vleck susceptibility, $\chi^{vv,cal}$, for two orientations are also plotted.

The total contribution due to the core diamagnetism is estimated using Eq. (4.11) to be χ^{core} = -0.36×10^{-4} cm^3/mole. The Landau contribution due to the orbital motion of the conduction electrons is:

$$\chi^{Landau} = -\frac{1}{3}\left(\frac{m}{m^*}\right)^2 \chi^{sp}(1-\alpha)\,, \tag{4.18}$$

where χ^{sp} is the Pauli spin susceptibility of the conduction electrons. For free electrons the Landau term is -1/3 of the Pauli term. Here, although we don't have an exact estimate of the effective mass m^* and of the Stoner enhancement factor (1 - α) we can assume $(m/m^*)^2(1 - \alpha) << 1$ since the conduction electrons are certainly far from being free electrons [12]. Thus we can neglect the Landau contribution in Eq. (4.17). The Van Vleck contribution is then given by $\chi^{VV} = \chi^{meas} - \chi^{sp} - \chi^{imp} - \chi^{core}$, as shown in Fig. 4.24. The results indicate that the anisotropy of the total susceptibility mostly comes from the anisotropy of the Van Vleck contribution, although the contribution to the anisotropy from the spin susceptibility is not negligible. It is noted that if we assume the presence of a diamagnetic contribution to the ^{11}B NMR shift as discussed above the estimate of the spin susceptibility would increase and the Van Vleck contribution would decrease.

4.2.4.3 Calculation of the Van Vleck Susceptibility

The occurrence of temperature dependence in the spin susceptibility is not surprising for this narrow *d*-band metal with sharp features in the density of states near the Fermi energy as shown by band calculations [88-90]. However, the anisotropy of the spin susceptibility is rather surprising for this system with a three-dimensional electronic band structure [88-90]. In order to confirm our experimental results the Van Vleck susceptibility was calculated theoretically (by J. Y. Rhee) since the Van Vleck term is expected to be a main contribution to the anisotropy of the total susceptibility.

We calculated the energy band structure using the scalar-relativistic, tight-binding, atomic-sphere-approximation, linear-muffin-tin orbital method. The exchange-correlation effects were included within the local density approximation. 352 irreducible **k**-points were used to obtain the self-consistent potential and charge. The muffin-tin radii used for the calculation were 3.628, 2.775, 1.714 and 1.715 a.u. for Y, Ni, B and C, respectively. The resultant band structure was in good agreement with the result of Lee et al. [90]. The density of states at the Fermi level was found to be 3.95 states/eV f.u.. The Van Vleck susceptibility is given by [95]

$$\chi^{VV,cal} = \frac{2}{V}\mu_B^2 \sum_{i,f,k} \frac{f_{FD}(E_i)\left[1 - f_{FD}(E_f)\right]\left|\langle f|\boldsymbol{L}|i\rangle\right|^2}{E_f - E_i}, \tag{4.19}$$

where V is the unit cell volume, μ_B is the Bohr magneton, E_f and E_i are the energies of final (empty) and initial (occupied) states, respectively, and $f_{FD}(E)$ is the Fermi-Dirac distribution function. We used the linear tetrahedron method for **k** space integration for 10,125 tetrahedra in 1/16 of the Brillouin zone. The detailed method of calculation is explained in Ref. [96]. The calculated value of χ^{VV}, $\chi^{VV,cal}$ is 1.77×10^{-4} cm^3/mole and 1.51×10^{-4} cm^3/mole at $T = 0$ for $\boldsymbol{H} \parallel \boldsymbol{c}$ and $\boldsymbol{H} \perp \boldsymbol{c}$, respectively. We also calculated the temperature dependence of χ^{VV} by employing a finite temperature Fermi-Dirac distribution function when the **k** space integration was performed. It showed a small temperature dependence, i.e. about a 2 % decrease in magnitude when going from 0 K to 300 K.

The $\chi^{VV,cal}(T)$ results are shown in Fig. 4.24 together with the experimental results. As shown in Fig. 4.24, the experimental results are in excellent agreement with the theoretical calculation in view of both the magnitude and the sign of the anisotropy of χ^{VV}. Furthermore, the small temperature dependence of χ^{VV} obtained by the calculation indicates strongly that the anisotropy of χ^{VV} does not explain the whole anisotropy of the total susceptibility which is instead more temperature dependent. This confirms our conclusion that the spin susceptibility χ^{sp} is anisotropic and temperature dependent.

4.2.4.4 ^{11}B and ^{89}Y Hyperfine Coupling Constants

From the analysis of the Knight shifts discussed before we were able to derive an estimated value of the hyperfine coupling constants [see Eq. (4.13)]. For ^{11}B the isotropic hyperfine constant is very small: $A_{iso} = (A_{\parallel} + 2A_{\perp})/3 = 7.6$ mole $YNi_2B_2C/cm^3 = 3.8$ mole B/cm^3. This value, which pertains to the contact interaction of *s*-electrons at the Fermi level, is very small when compared with the atomic hyperfine constant for the 2*s* electrons of the boron atom [12]:

$$A_s^{at} = 10^6 \text{ Gauss}/N_A \mu_B = 179 \text{ mole B/cm}^3 . \qquad (4.20)$$

One may conclude that the amount of *s*-character of the wave function of the conduction electrons at the Fermi level at the B site in YNi_2B_2C is very small. It is noted that the small fraction of *s*-character of the wavefunction at the Fermi level derived here from the ratio $A_{iso}/A_s^{at} = 3.8/179 = 0.021$ is consistent with the small value calculated for the density of *s*-states at the Fermi level at B site: $N_s(E_F) = 0.04$ states/eV B atom [90].

On the other hand the anisotropic part of the hyperfine interaction is relatively large: $3A_{ax} = A_{\parallel} - A_{\perp} = 2.5$ mole YNi_2B_2C/cm^3. The result is consistent with a *p*-character of the conduction electrons at the Fermi level and at the boron site. For an axial symmetry of the electronic cloud around the boron site one expects [8]:

$$N_A A_{ax} = \left\langle \int_{\text{atomic volume}} \Psi_k^*(r) \left[\frac{3\cos^2\theta_k - 1}{r^3} \right] \Psi_k(r) d^3r \right\rangle_F , \qquad (4.21)$$

where the dipolar interaction of the ^{11}B nucleus with the electronic moment is averaged over the wave function of the conduction electrons at the Fermi level, θ_k being the angle between the *c* axis and the vector joining the nucleus and the electron. From Eq. (4.21) one has $\langle 1/r^3 \rangle_F = 2N_A A_{ax} = 1.0\times10^{24}$ cm^{-3} where the average is over the unit cell for electrons at

the Fermi level and the factor 2 was introduced to account for the two boron atoms in the formula unit. This value for $<1/r^3>_F$ is about 20 % of the value $<1/r^3>_{at} = 5.45\times10^{24}$ cm^{-3} which can be derived for the average over the 2*p* atomic electrons of boron from the hyperfine structure of molecular beam spectra [97]. This value of 20 % is also consistent with the calculated value of the density of p-states at the Fermi level at B site: $Np(E_F)$ = 0.18 states/eV B atom [90].

In the case of ^{89}Y the dominant term in the Knight shift arises from the orbital moment induced, in second order perturbation theory, in occupied electron states by the applied magnetic field. The orbital Knight shift K^{orb} is proportional to the orbital contribution to the total susceptibility. It is noted that the positive sign of the K_{ax}^{orb} in Eq. (4.14) is opposite to the sign of the anisotropy of the orbital contribution to the susceptibility. This implies that the sign of K_{ax}^{orb} is determined by the anisotropy of the orbital hyperfine coupling constant.

The term in the Knight shift in Eq. (4.11) proportional to the spin susceptibility yields a negative hyperfine coupling constant [see Eq. (4.16)]. This implies that the dominant contact interaction for ^{89}Y is via polarization of the core *s*-electrons by the *d*-electrons in the conduction band, a situation common in transition metals [12]. This circumstance is consistent with a temperature dependent spin susceptibility dominated by the contribution of a narrow *d*-band.

4.2.4.5 NSLR and Antiferromagnetic Fluctuations

The ^{11}B NSLR data in Fig. 4.19 show a deviation from the Korringa behavior, $(T_1T)^{-1}$ = constant. This result was previously [84] interpreted tentatively as an indication of the presence of an enhancement of the relaxation due to antiferromagnetic fluctuations as commonly found in Cu-based high-T_c superconductors. However, most of the temperature dependence of $(T_1T)^{-1}$ is found to track the temperature dependence of the Knight shift. This is shown in Fig. 4.25 where we plot vs T the Korringa ratio: $\kappa = T_1TK^2/S$ where $S = (\gamma_e/\gamma_N)^2(h/8\pi^2k_B) = 2.5\times10^{-6}$ (sec K) for the ^{11}B nucleus and $K \equiv {}^{11}K_{iso}$. As can be seen from Fig. 4.25, the Korringa ratio is close to the value of $\approx$ 1.6 found for simple metals like Li,

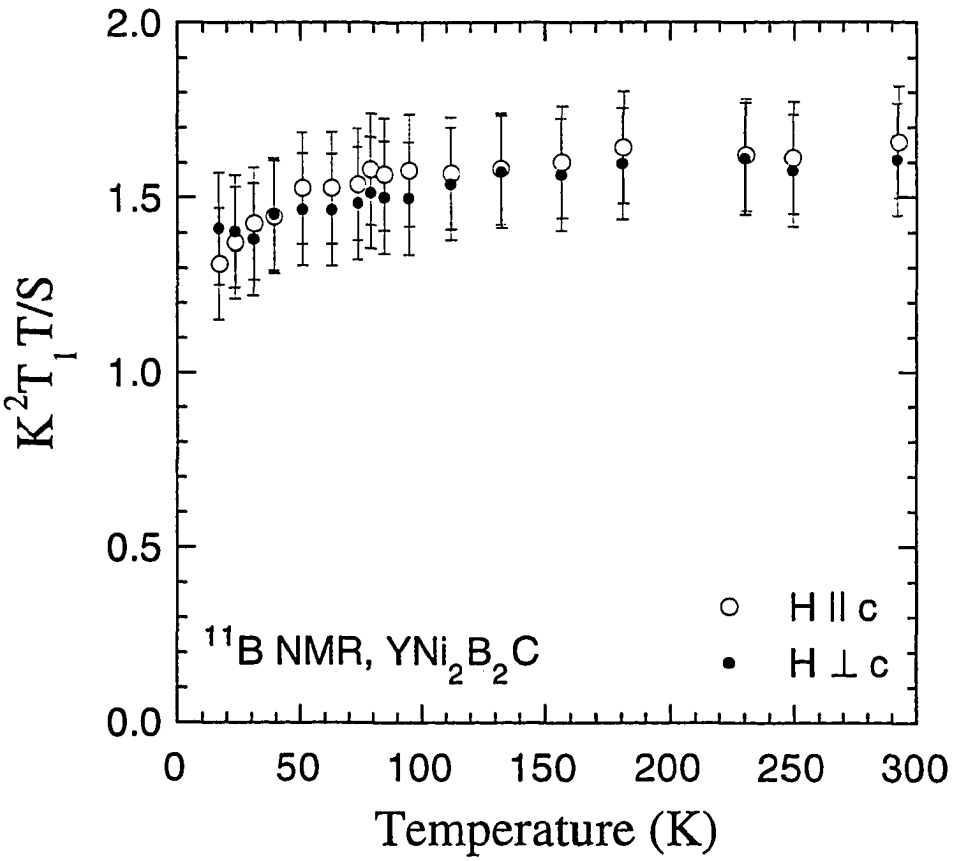

Fig. 4.25 Plot of the Korringa ratio, $(K^2T_1T)/S$ for ^{11}B NMR vs temperature in stacked YNi_2B_2C single crystals for $H = 8.2$ T and for two orientations of the external field.

Na and Al [12]. Since the ^{11}B nucleus occupies a symmetry site in the lattice where it should be sensitive to AF fluctuations of the Ni moment one should conclude that, with the possible exception of the lowest temperatures ($T < 50$ K), no measurable AF fluctuations of the Ni moment are present. It is noted that the small decrease of the Korringa ratio at low temperature in Fig. 4.25 could be an artifact due to the presence of the paramagnetic impurities. The randomly distributed paramagnetic centers contribute to the NSLR but not to the Knight shift and the contribution to the NSLR is temperature independent. Thus the paramagnetic contribution becomes more important with lowering temperature. If one modifies the estimate of the spin susceptibility by assuming the presence of negative contribution to the ^{11}B Knight shift, as discussed above, the Korringa ratio plotted in Fig. 4.25 would maintain the same temperature dependence but the whole curve would be shifted to higher values. A value of the Korringa ratio greater than 1 is a common feature of *d*-band transition metals and alloys [12].

The ^{89}Y NSLR data in Fig. 4.17 show an almost constant behavior of $(T_1T)^{-1}$. Since the ^{89}Y Knight shift is the sum of an orbital and a spin contribution [see Eq. (4.15)] it is reasonable to also expect two contributions to the NSLR:

$$S(T_1T)^{-1} = [K^d(T)]^2 + R^{orb} \tag{4.22}$$

where $K^d(T)$ is the core polarization contribution to the Knight shift, which was written in Eq. (4.15) as $^{89}A\chi_{iso}(T)$, and R^{orb} is the orbital contribution to the NSLR which, however, is not proportional to the orbital Knight shift, $K_{iso}{}^{orb}$, in Eq. (4.15). The coefficient S is $S = (\gamma_e/\gamma_n)^2\ (h/8\pi^2k_B) = 1.09\times10^{-4}$ (sec K) for the ^{89}Y nucleus. Unfortunately there is no simple way to separate the two contributions to the NSLR in Eq. (4.22). Since from Fig. 4.17 it appears that $(T_1T)^{-1}$ is practically temperature independent while $K^d(T)$ in Eq. (4.22) has the temperature dependence of the spin susceptibility (Fig. 4.24) one could tentatively conclude that the NSLR of ^{89}Y has a sizable contribution from the T-independent orbital term in Eq.

(4.22). In any case there is no evidence for any contribution due to AF fluctuations of the Ni moments.

4.2.4.6 ^{11}B NSLR in the Superconducting State

Figure 4.26 shows the ^{11}B NSLR in a powder sample at 1.2 and 2.4 Tesla both in the normal and in the superconducting state. The isotropic ^{11}B NSLR in the normal state displays the enhancement with lowering temperature as discussed already, and here the enhancement is shown to be field independent. In the superconducting state, the Hebel-Slichter (HS) peak which is expected to appear just below T_c for a conventional superconductor [98] was not observed. This may be due to the quenching of the HS peak in the 1.2 and 2.4 T applied fields. The relaxation rate values T_1^{-1} for 1.2 T can be fit using the BCS theory given by [99]

$$\frac{1}{T_1} \propto \exp\left(-\frac{\Delta_0}{k_B T}\right), \tag{4.23}$$

with $\Delta_0/k_B = 18.6 \pm 0.7$ K, where Δ_0 is the superconducting gap parameter, as shown by the solid curve in Fig. 4.26. The superconducting transition temperature T_c was measured from the initial detuning of the NMR tank circuit, which is equivalent to measuring the change of the inductance of the system, and the result is $T_c = 11 \pm 1$ K at 1.2 T. Using $T_c = 11 \pm 1$ K and the above value of Δ_0/k_B, we obtain the value $2\Delta_0 = (3.4 \pm 0.5)k_B T_c$ which is very close to the BCS value, $2\Delta_0 = 3.52 k_B T_c$. It is noted that $(T_1T)^{-1}$ saturates below 5 K [see Fig. 4.26(b)]; this saturation could be an artifact due to the presence of a small temperature independent contribution to the NSLR arising from the paramagnetic centers.

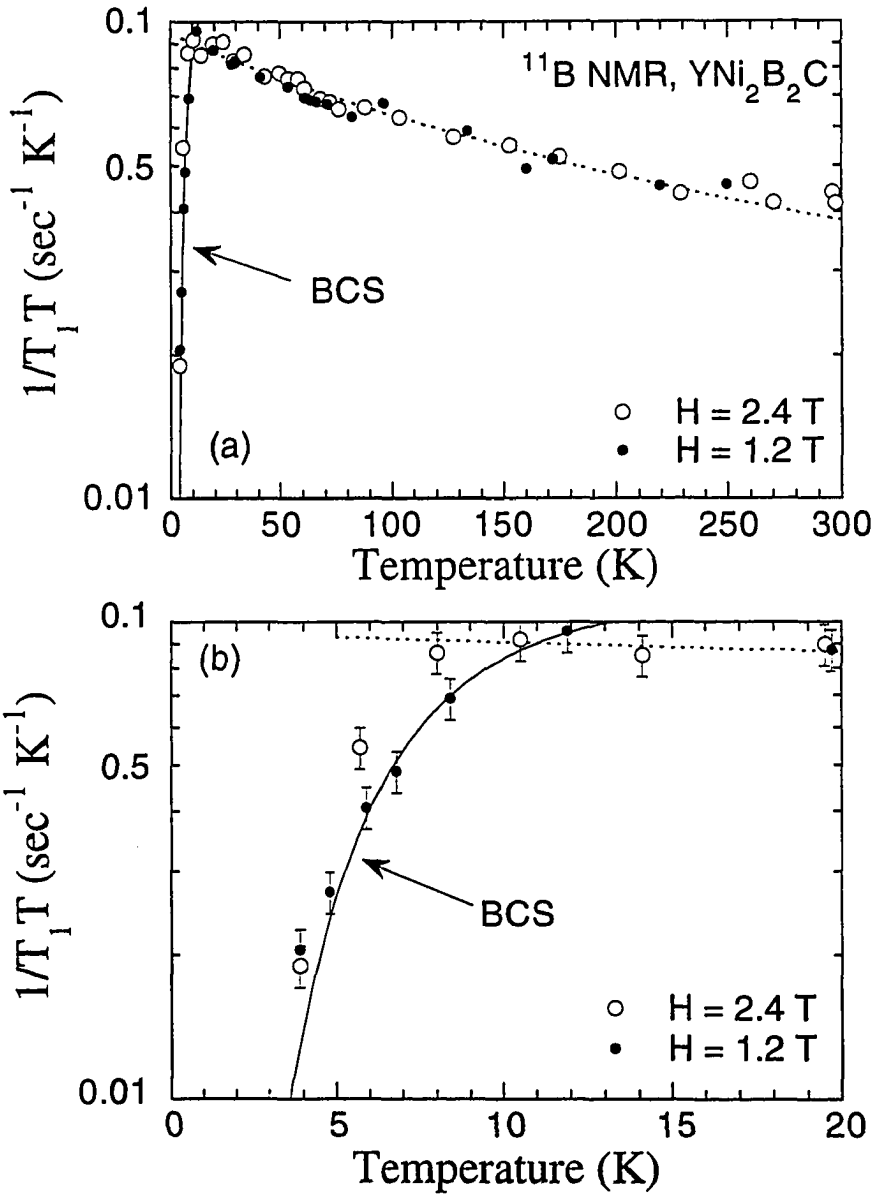

Fig. 4.26 Plots of $(T_1T)^{-1}$ of ^{11}B vs temperature in a YNi_2B_2C powder sample for two magnetic field intensities. The solid line is a fit of the data for $H = 1.2$ T using BCS theory [see Eq. (4.19)] with $\Delta_0/k_B = 18.6 \pm 0.7$ K. (Courtesy of Q. Hu and K. -H. Kim)

4.3.5 Summary and Conclusions

In summary we have reported an accurate NMR measurement to investigate the microscopic electronic properties of YNi_2B_2C. From the analysis of Knight shift and susceptibility we have derived the hyperfine coupling constants and successfully separated the macroscopic susceptibility into different possible contributions. The experimental results are found to be in good agreement with theoretical calculations.

Somewhat to our surprise, we find a temperature-dependent and anisotropic spin susceptibility χ^{sp}. The temperature dependence of χ^{sp} can be explained in terms of a narrow *d*-band with a high density of *d*-states at the Fermi level. The anisotropy of χ^{sp} in this 3-dimensional system is not yet understood, but might be due to asymmetry of the *g*-factor. Most important, by testing the Korringa relation in the normal state, we find that the enhancement in the ^{11}B NSLR with decreasing temperature is simply reflecting the increase of the spin susceptibility with lowering temperature and is not due to any magnetic character on the Ni sublattice such as antiferromagnetic fluctuations of localized and/or itinerant electron spins. Thus we conclude that the quaternary intermetallic compound YNi_2B_2C is different from the cuprate high-T_c superconductors, in this respect.

In the superconducting state, the ^{11}B NSLR is found to fit a BCS behavior with a superconducting gap parameter $2\Delta_0 = (3.4 \pm 0.5)k_BT_c$, as expected from the Fermi liquid normal state properties of the compound.

* Note added in proof: The main argument which led us to the above interpretation of the temperature dependence of the ^{11}B Knight shift is that, normally, the s-band spin susceptibility is temperature independent. However, based on the observation that the theoretical calculations [90] show that there is no contribution of the *d*-band electrons at the boron site and that the density of states of 2*s*-electrons at the boron site has sharp features at the Fermi level, we were forced to change somewhat the analysis of the Knight shift data.

Since there is no *d*-electrons at the boron site [90], one can neglect any contribution to K from core polarization and χ^{VV} [12]. Thus we can write

$$K_{iso}(T) = A_s^{at} \chi_s^{sp} , \tag{4.24}$$

where $\chi_s^{sp}(T)$ is the spin susceptibility contribution of the boron 2*s*-band electrons at the Fermi surface. That is, the ^{11}B Knight shift probes only the local $N_s(E_F)$ at the boron site and, in particular, not the *d*-band contribution of the Ni atoms to $N(E_F)$. The new analysis of the spin susceptibility and the separation of the magnetic susceptibility are presented in detail in Ref. [99a]. It is noted, in this case, the large T-dependence of χ_s^{sp} which can be obtained from the $K_{iso}(T)$ data in Fig. 4.18(b) is evidently a consequence of a strongly varying $N_s(E)$ near E_F. However, since the same contact hyperfine interaction in Eq. (4.24) which is responsible for $^{11}K(T)$ is also responsible for the ^{11}B $T_1^{-1}(T)$, the Korringa relation K^2T_1T = constant should be still satisfied unless there is any other contribution to the ^{11}B T_1^{-1} due to AF fluctuations. Therefore, the main observation of this work that there is no AF fluctuations/correlations on Ni sublattice is still valid. Detailed discussions on the absence of the AF correlations also appear in Ref. [99a].

5. NMR AS A PROBE TO STUDY THE VORTEX DYNAMICS IN HIGH-T_c SUPERCONDUCTORS

In type II superconductors (SC), an applied magnetic field H greater than the lower critical magnetic field H_{c1} penetrates bulk samples in the form of flux lines (FL). The flux lines distribute regularly in such a way as to minimize the energy and we call this distribution of the flux lines a flux lattice (or a vortex lattice) where each flux line carries the flux quantum $\Phi_0 = hc/2e = 2.07\times10^{-7}$ G cm^2.

High-T_c SC (HTSC) are also type II SC and are characterized by a marked anisotropy, largely resulting from their 2D structure and peculiar electronic properties. Appropriate modifications [100] of the Ginzburg-Landau-Abrikosov (GLA) theory which were developed for the isotropic conventional SC are necessary to describe the properties of the flux lattice in the HTSC and, in favorable circumstances, the dynamics of the flux lines [101]. For example, in $YBa_2Cu_3O_7$ (YBCO) and with the magnetic field along the c axis perpendicular to the CuO_2 superconducting planes, each filament of FL has a core radius of the order of the coherence length $\xi_{\|} = 25$ Å and for $H = 8$ T the distance between the FL's is $d \approx (\sqrt{3/2}\Phi_0 / B)^{1/2} \approx 180$ Å. Away from a filament and along a given radial direction, the field decreases in a way related to the London penetration length $\lambda_{\|} = 1400$ Å (for $T << T_c$). Thus the profile of the local field $B(\boldsymbol{r})$ exhibits an amplitude modulation whose second moment is

$$\left\langle \Delta B^2 \right\rangle \cong 0.00371 \frac{\Phi_0^2}{\lambda_{\|}^4}, \tag{5.1}$$

for a triangular vortex lattice [102], corresponding to a peak to peak ripple around the average $\overline{B}$ of about 60 Gauss for YBCO.

In HTSC materials more anisotropic than YBCO, such as the Tl or Hg based compounds, the ratio $\lambda_{\parallel}/\lambda_{\perp}$ can be of the order of 100 to 500. Since $\xi_{\perp}$ is less than the interplane distance one cannot use the GLA approach to describe the FL lattice. The Abrikosov lattice of the FL's can be considered an elastic continuum and it exhibits interesting vibrational and fluctuation properties. In particular, in HTSC, because of the high temperature range and of the marked anisotropy, strong thermal motions of the FL are present.

The dynamical properties of the flux lines have both a fundamental interest and a strong impact on possible applications. When a current flows in the SC, there is a drift of the FL's under the Lorentz-like force. Flux motion induces an electric field, causing dissipation of the current and thus destroying the zero-resistivity state. The applications of the HTSC are hindered by the large mobility of the FL's. It appears very useful to compare the macroscopic-type techniques such as magnetization and transport measurements with microscopic tools, as offered by NMR experiments for the study of the FL dynamics.

NMR is a technique sensitive to the local field inside samples. The local field distribution due to the flux lattice can be characterized by the NMR resonance line profile or the line width ($\Delta\nu$). In addition, when a flux line (FL) in a type II superconductor moves in the lattice, the surrounding nuclei are subject to a modulation of the local internal magnetic field which can affect in various ways the NMR parameters. While the applications in conventional type II superconductors have been limited [99,103], HTSC appear to be more suitable for NMR studies of FL's dynamics. The random thermal motion of the FL's has been detected through the anomalous narrowing of the inhomogeneously broadened NMR line [104-107] and from the recovery of the transverse nuclear magnetization in a spin-echo experiment [31,61]. Also the motion of vortices driven by an electric current or by a change in the applied DC magnetic field has been detected through linewidth [108] and spin-echo measurements [109,110].

In this chapter, we present NMR measurements performed on two typical HTSC compounds YBCO and $HgBa_2CuO_{4+\delta}$ aimed at the investigation of the thermal fluctuations of FL's.

5.1 NMR Investigation of Thermally Activated Flux Motion in $YBa_2Cu_3O_7$ from ^{89}Y Spin-Spin Relaxation

5.1.1 Introduction

In this section, we present a novel NMR approach to investigate FL dynamics based on the measurements of the decay of the echo signal amplitude in an ordinary two-pulse spin-echo (TPSE) experiment. In a TPSE experiment one probes the irreversible dephasing of the transverse nuclear magnetization during the time interval τ between two radio frequency pulses [27,28], discussed in section 2.2. If the vortex core moves even a few lattice spacings in the time interval between the two pulses, the nuclei will experience a dephasing effect due to the change of local magnetic field strength and thus of the Larmor precession frequency. This should result in an observable attenuation of the spin echo amplitude as an additional contribution to the nuclear magnetic relaxation time T_2.

The $I = 1/2$, ^{89}Y nucleus appears to be an ideal probe since ^{89}Y has an intrinsically narrow NMR line, and no complications coming from nuclear electric quadrupole effects, plus a relatively long spin-spin relaxation time T_2. The ^{89}Y NMR data presented below for $YBa_2Cu_3O_7$ (YBCO) appear to confirm the predicted dephasing effect due to flux motion. The observed anomalous decay of the echo amplitude just below T_c is explained quantitatively by a simple theoretical approach based on slow random fluctuations in the local Larmor frequency $\omega(t)$.

Two samples of $YBa_2Cu_3O_7$ with $T_c = 92 \pm 1$ K were prepared and the powder grains of an average diameter 25 to 38 μm were mixed with epoxy resin and oriented in an 8.2 Tesla magnetic field. The detailed alignment procedure is described in section 4.1. The estimated superconducting transition temperature at 8.2 T was $T_c = 87.5 \pm 1$ K for $\boldsymbol{H} \parallel \boldsymbol{c}$ and $T_c = 89 \pm 1$ K for $\boldsymbol{H} \perp \boldsymbol{c}$ corresponding to the irreversibility transition temperature $T_{irr} \approx 78.5 \pm 1$ K for $\boldsymbol{H} \parallel \boldsymbol{c}$ and $T_{irr} \approx 80 \pm 1$ K for $\boldsymbol{H} \perp \boldsymbol{c}$ at 8.2 T as measured from the detuning of the NMR probe. The NMR measurements were performed with a phase coherent pulse Fourier Transform (FT) spectrometer operating at 17.104 MHz in a field strength of 8.2 T. Typical $\pi/2$ pulse lengths for ^{89}Y were 20 to 25 μsec corresponding to an rf magnetic field strength of 60 Gauss. The NMR line width ΔH was determined from the FT of half of the ^{89}Y echo signal. The echo decay rate was monitored with a two-pulse spin-echo sequence $(\pi/2)_x - \tau - (\pi)_y$ with variable τ separation between pulses. All measurements were taken in field cooled conditions with an applied magnetic field of 8.2 T >> H_{c1}. Thus, the flux lattice should be viewed as a regular lattice with the density of vortices greater than that of pinning centers.

5.1.2 Results and Discussions

5.1.2.1 NMR Linewidth and Line Narrowing

Before analyzing the main results, the spin-echo decay in a TPSE experiment, we first present and discuss the NMR linewidth briefly. The vortex lattice for $T << T_c$ can be considered "rigid", namely, the characteristic correlation times τ_c of vortex motions are much longer than the inverse of the intrinsic NMR linewidth. In principle, the NMR line shape should reflect the field distribution, in particular, its singularities and its characteristic symmetry. However, the singularities expected from a regular triangular vortex lattice can be smeared out by the distribution of demagnetizing factors D_i in multigrain powder samples and by the distortion of the flux line due to the pinning effects.

This is the common situation found in YBCO compounds where a practically Gaussian ^{89}Y line has always been observed.

In the vortex state the second moment of the local field $B(r)$ is expressed by Eq. (5.1). If we adopt the well-known temperature dependence of $\lambda(T)$ of the conventional SC [111], we obtain the temperature dependence of $\Delta\nu(T)$ given by

$$\Delta\nu(T) = \Delta\nu(0)\frac{\lambda^2(0)}{\lambda^2(T)} = \Delta\nu(0)\left[1-\left(\frac{T}{T_c}\right)^4\right]. \tag{5.2}$$

On the other hand, if the local field fluctuates in time due to the thermally excited flux motion, an extra motional line narrowing is expected. Quantitative estimates of the correlation time, τ_c, of the flux motion can be obtained by extending the well known theories for the motional narrowing [2] to the case of FID (or half echo) signals $s(t)$ resulting from the distribution of the local fields. Then one has

$$s(t) = \exp\left\{-\gamma^2\tau_c^2\left\langle\Delta B^2\right\rangle\left[\exp\left(-\frac{t}{\tau_c}\right)-1+\frac{t}{\tau_c}\right]\right\}, \tag{5.3}$$

where γ is the nuclear gyromagnetic ratio. The typical ^{89}Y NMR linewidth, $\Delta\nu$, versus temperature in $YBa_2Cu_3O_7$ is shown in Fig. 5.1 where one can see that $\Delta\nu$ follows the temperature dependence expected from Eq. (5.2) except for a small deviation near T_c which can be explained by thermally excited flux motion. This thermally excited flux motion is strongly dependent on the pinning mechanism and/or the anisotropy of the flux lines. Thus, for strongly pinned FL's such as in the optimally doped YBCO we measured, an NMR linewidth measurement is not suitable to obtain the evidence of FL motions. This method is not useful either for the case of strongly anisotropic HTSC as in Tl-based compounds since the NMR line narrowing does not appear consistent with a picture of thermally activated motions [106]. However, in a suitable case such as $YBa_2Cu_4O_8$, which is more

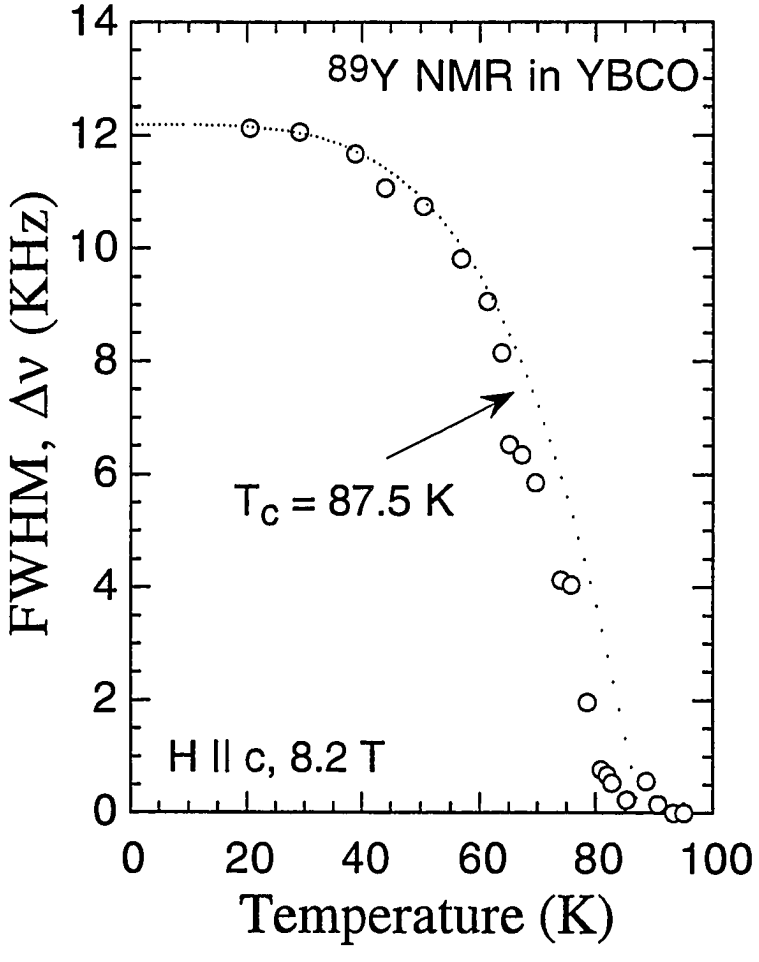

Fig. 5.1 Temperature dependence of the ^{89}Y NMR linewidth, $\Delta\nu$, in an optimally doped $YBa_2Cu_3O_7$ oriented powder for $H = 8.2$ T and $\boldsymbol{H} \parallel \boldsymbol{c}$. The dotted curve is the behavior expected from the temperature dependence of the penetration length, λ, without motional narrowing effects [see Eq. (5.2)].

anisotropic than YBCO, the linewidth measurement can offer a powerful probe to investigate the thermally activated FL motions. An interesting extra motional narrowing in ^{89}Y $\Delta\nu$ in $YBa_2Cu_4O_8$ was reported by Carretta [105]. In his work, the observed anomalous line narrowing was interpreted by the presence of two different motional regimes. For $T \leq$ 35 K the results were fit well with a thermally activated τ_c with an effective activation energy $U \cong 145$ K. On the other hand, for $T \geq 35$ K the data were fit reasonably well assuming a temperature independent $\tau_c \cong 35$ μs. The anomalous changeover of the temperature dependence of τ_c might be considered as the occurrence of a partial melting of the vortex lattice, whereby the vortices are transformed at $T \approx 35$ K from 3D lines to 2D "pancakes" without correlation between adjacent CuO_2 planes [100].

Returning to the case of strongly pinned FL's, it is possible to study very low thermal motion of the vortices in the nearly static FL lattice by measuring the decay of the spin-echo amplitude as discussed next.

5.1.2.2 Spin-Echo Decay and Thermally Activated FL Motion

The typical decay of the transverse nuclear magnetization in a TPSE experiment is shown in Fig. 5.2 for two temperatures, above and below T_c, and for two crystal orientations with respect to the magnetic field, $\boldsymbol{H} \parallel \boldsymbol{c}$ and $\boldsymbol{H} \perp \boldsymbol{c}$. The decay rate is orientation dependent even at room temperature. Part of the anisotropy can be explained in terms of ^{89}Y-^{89}Y dipolar interactions while a small contribution may be related to the anisotropy of the Cu spin susceptibility [104]. The temperature dependence of the decay is of prime interest here. Above T_c the temperature dependence is negligible while below T_c the decay of the nuclear magnetization becomes faster and deviates strongly from an exponential time dependence (see Fig. 5.2). The data were fit with the equation:

$$M(t = 2\tau) = M(0)\exp\left(-\frac{t}{T_2}\right)\exp\left[-\left(\frac{t}{T_{2add}}\right)^3\right]. \qquad (5.4)$$

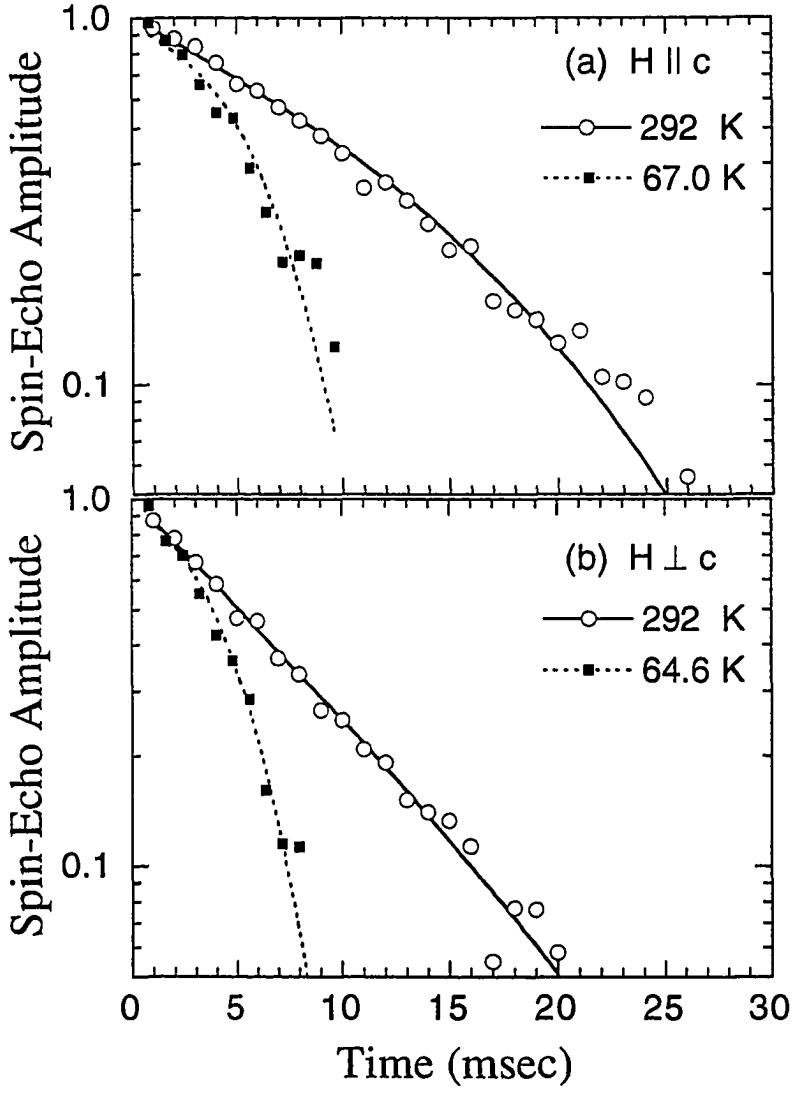

Fig. 5.2 Typical decay of the spin-echo amplitude vs $t = 2\tau$ in a TPSE experiment for ^{89}Y in $YBa_2Cu_3O_7$. The curves are fits using Eq. (5.4) with (a) for $\boldsymbol{H} \parallel \boldsymbol{c}$, $T_2 = 13.5$ msec and $T_{2add} = 23.9$ msec (at $T = 292$ K); $T_{2add} = 7.8$ msec (at $T = 67$ K), and (b) for $\boldsymbol{H} \perp \boldsymbol{c}$, $T_2 = 7.4$ msec and $T_{2add} = 30.8$ msec (at $T = 292$ K); $T_{2add} = 6.8$ msec (at $T = 64.6$ K).

Note that the data could be fit equally well by replacing the $\exp[-(t/T_{2add})^3]$ term with a Gaussian term. Unfortunately, the signal to noise ratio was not sufficient to resolve the weight of the two terms, even with considerable signal averaging. However, above T_c, the Gaussian form yields a slightly better fit while the $\exp[-(t/T_{2add})^3]$ term yields a better fit below T_c indicating the probable presence of both terms.

More relevant for the purpose of the present experiment is a comparison between the TPSE decay and the decay obtained by a Carr-Purcell-Meiboom-Gill (CPMG) sequence [28,29], discussed in section 2.2. In fact, in the CPMG sequence given by $(\pi/2)_x - \tau - [\pi_y - 2\tau -]_n$, any dephasing of the nuclear magnetization $M(t = 2\tau)$ due to a change of the local magnetic field at the nuclear site during the time interval τ is not cumulative and thus can be minimized by choosing τ shorter than the intrinsic spin-spin relaxation time T_2. However we found spin-locking effects present in the CPMG sequence experiment for short τ values as discussed in section 2.2. In order to avoid spin-locking effects we have devised a modified sequence with alternating phases of the y-pulses given by $(\pi/2)_x - \tau - [\pi_y - 2\tau - \pi_y - 2\tau - \pi_{-y} - 2\tau - \pi_{-y} - 2\tau -]_n$ which will be called the AP-CPMG sequence [30]. With the above AP-CPMG sequence, the results for the echo decay rate for $T > T_c$ are nearly the same as the results for the TPSE as expected in the absence of flux motion, confirming that the phase alternation does indeed eliminate spin-locking effects. On the other hand, just below T_c, one observes the onset of an extra contribution to the spin-echo decay, a contribution which becomes negligible in the AP-CPMG decay as shown in Fig. 5.3. We are thus led to the conclusion that the additional contribution to the decay of the spin-echo signal is to be attributed to a change of local magnetic field due to the time dependence of the magnetic field gradient associated with flux motion.

We turn now to the temperature dependence of the echo decay. By referring to the fit of Eq. (5.4) we find a temperature independent exponential term yielding $T_2 = 13.5$ msec for $\boldsymbol{H} \parallel \boldsymbol{c}$ and $T_2 = 7.4$ msec for $\boldsymbol{H} \perp \boldsymbol{c}$ and an additional temperature dependent contribution $(T_{2add})^{-1}$. $(T_{2add})^{-1}$ is small and almost T independent above T_c, while just below T_c, $(T_{2add})^{-1}$ displays an enhancement followed by a decrease back to the same value as above T_c (see

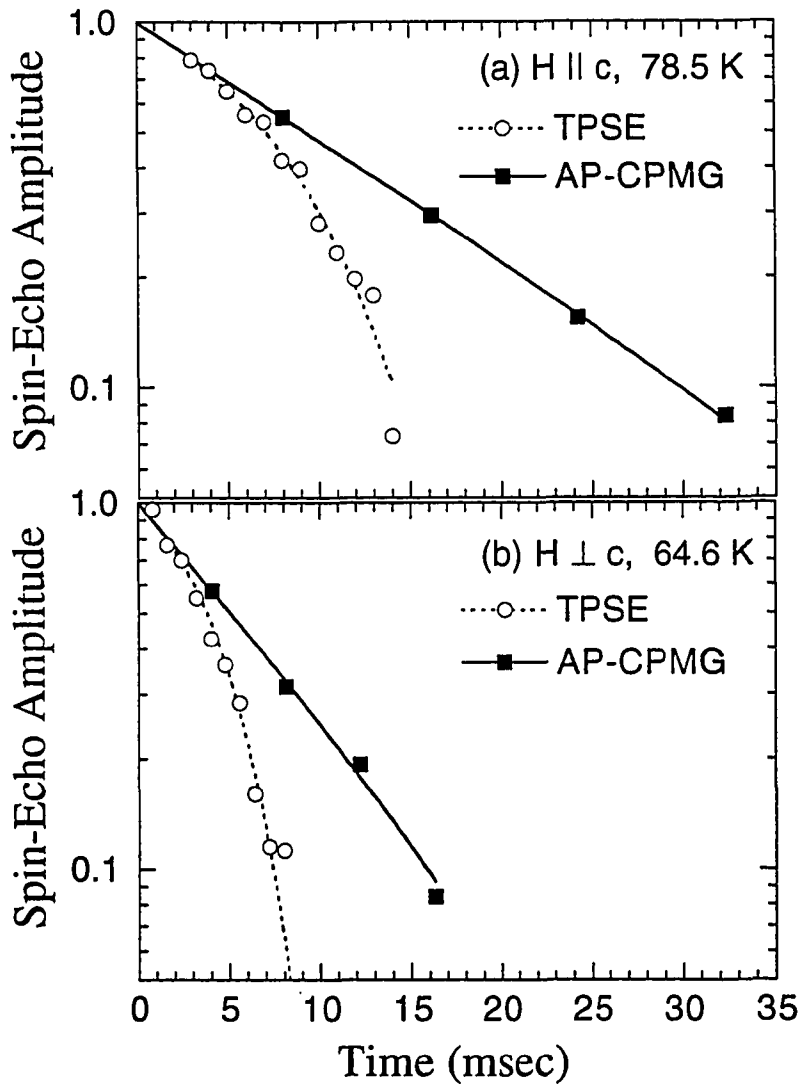

Fig. 5.3 Comparison of the spin-echo decay for ^{89}Y in $YBa_2Cu_3O_7$ in a TPSE and an AP-CPMG experiments. The curves are fits using Eq. (5.4) with (a) for $\boldsymbol{H} \parallel \boldsymbol{c}$, $T_2 = 13.5$ msec and $T_{2add} = 13.0$ msec (TPSE); $T_{2add} = 66.7$ msec (AP-CPMG), and (b) for $\boldsymbol{H} \perp \boldsymbol{c}$, $T_2 = 7.4$ msec and $T_{2add} = 6.8$ msec (TPSE); $T_{2add} = 29.0$ msec (AP-CPMG).

Fig. 5.4). We propose the maximum of $(T_{2add})^{-1}$ below T_c can be understood in terms of thermal motions of the vortices. By using for the line narrowing the theoretical approach [2] based on slow random fluctuations in the local Larmor frequency $\omega(t)$, it can be shown that one has an additional mechanism of the decay of the spin-echo intensity in a TPSE experiment given below at t =2τ by [112]

$$M_G(2\tau) = \exp\left\{-\Delta^2 \tau_c \left[2\tau - \tau_c(1-e^{-\tau/\tau_c})(3-e^{-\tau/\tau_c})\right]\right\}, \tag{5.5}$$

which reduces in the nearly static limit ($\Delta\tau_c >> 1$) to

$$M_G(2\tau) = \exp\left[-\Delta^2 (2\tau)^3 / 12\tau_c\right], \tag{5.6}$$

where $\Delta^2 = <\omega(t)\omega(0)>_{t=0}$ and the fluctuating local frequency is described by a simple exponential correlation function: $<\omega(t)\omega(0)> = \Delta^2 \exp(-t/\tau_c)$. The additional contribution due to FL thermal motion can thus described by $(T_{2add})^{-1} = (\Delta^2/12\tau_c)$. The temperature dependence of the effective $(T_{2add})^{-1}$ was extracted from the analysis of the echo decay of ^{89}Y NMR in YBCO and it is shown in Fig. 5.4. The correlation time τ_c can be estimated from the experimental results by assuming a simple model where the random frequency is given by

$$\omega(t) = \gamma \delta H(t) \approx \gamma \overline{G} u(t), \tag{5.7}$$

where $\overline{G}$ is the average magnetic field gradient due to the flux lattice. For a triangular lattice $\overline{G} \cong 0.24\Delta H/d$, where ΔH is the inhomogeneous NMR linewidth and d is the intervortex distance. The spatial variable $u(t)$ describes the instantaneous position of the core of a FL, yielding $\Delta^2 = (\gamma \overline{G})^2 <u^2>$.

This model can be generalized to the case where the local field is related to the FL position variable, $u(t)$, by a nonlinear relation. We have calculated the average square thermal fluctuation from the expression [101]:

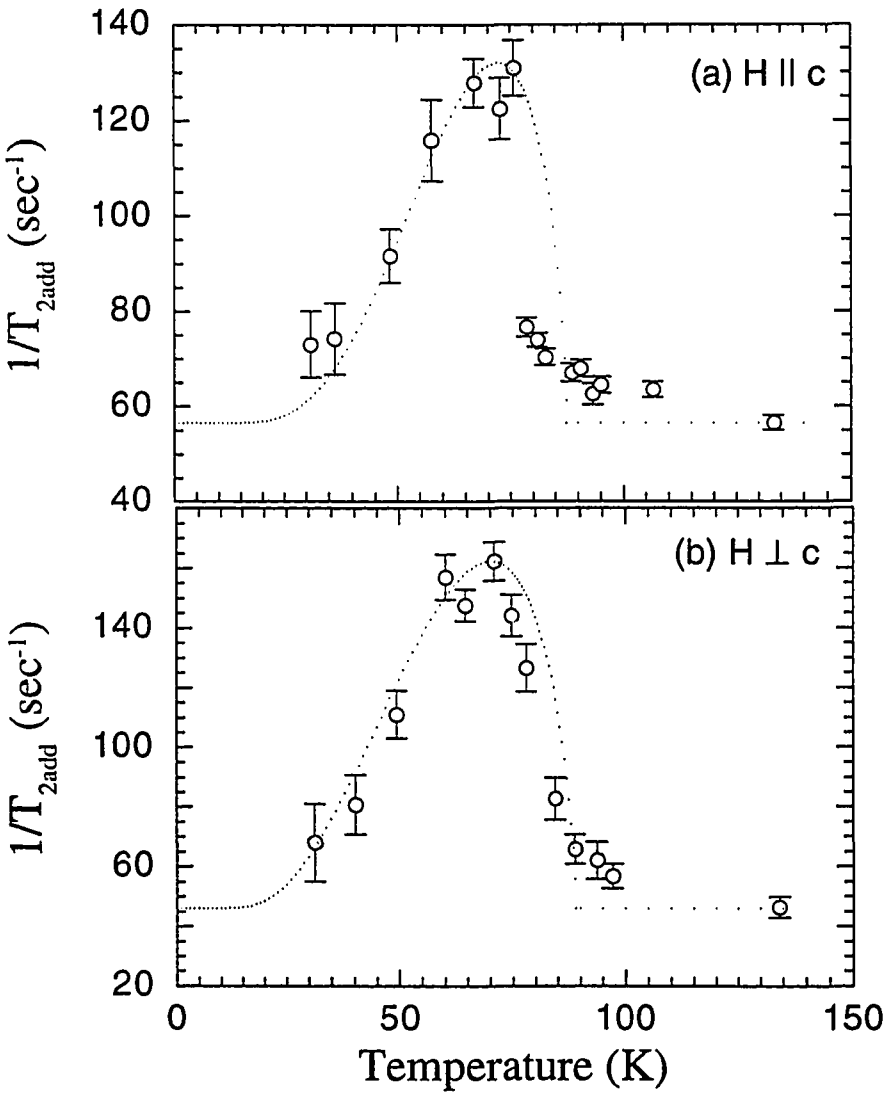

Fig. 5.4 Additional decay rate $(T_{2add})^{-1}$ obtained from the fit using Eq. (5.4) as a function of temperature for two orientations of the external field. The dotted curve is the theoretical fit from the expression $(T_{2add})^{-1} = (\Delta^2/12\tau_c)^{1/3}$ with τ_c given by Eq. (5.9) and a constant term given by $(T_{2add})_0^{-1} = 56.5$ sec^{-1} for $\boldsymbol{H} \parallel \boldsymbol{c}$ and $(T_{2add})_0^{-1} = 46.0$ sec^{-1} for $\boldsymbol{H} \perp \boldsymbol{c}$, respectively.

$$\langle u^2 \rangle = k_B T \mu_0 (4\pi / B\Phi_0^3)^{1/2} \lambda_{ab} \lambda_c \,, \tag{5.8}$$

where Φ_0 is the flux quantum and $\mu_0 = 1.2566\times10^{-6}$ m Kg/C and B is the external magnetic field. By using Eqs. (5.6)-(5.8), and the experimental values for the inhomogeneous linewidth, we evaluated the correlation time from the measured $(T_{2add})^{-1}$. The results are shown in Fig. 5.5. As can be seen, the correlation times τ_c are quite long and considerable error can come from the fact that the average field gradient may be overestimated. It is noted that the major part of the sample contributing to the NMR signal correspond to saddle point regions [61] where G is very small. Although one can correct for the overestimation of the average field gradient, the correlation time is still long. Such a long correlation time could be indicative of long wavelength fluctuations of the vortex lines. Another possible interpretation for the observed motion is obtained if one assumes that $\langle u^2 \rangle$ represents the average square hopping distance between pinning centers. This interpretation would lead to longer correlation times though.

In any case, the FL motion is considered due to thermal activation. The resultant correlation times can be fitted by the activated expression $\tau_c = \tau_0 \exp(U/T)$ and the fitting results are:

$$\begin{aligned} \tau_{c,\parallel} &= 3.2 \times 10^{-5} \exp\left(\frac{430}{T}\right) \quad \text{(sec)}, \\ \tau_{c,\perp} &= 2.4 \times 10^{-5} \exp\left(\frac{310}{T}\right) \quad \text{(sec)}. \end{aligned} \tag{5.9}$$

The fitting curves are shown in Fig. 5.5 and the dotted lines in Fig 5.4 represent the behavior expected for $(T_{2add})^{-1} = (\Delta^2/12\tau_c)^{1/3}$ when the fitting results for τ_c are used. As seen in Eq. (5.9), the τ_0 values for both orientations are rather large and seem to include considerable errors due to the uncertainty in $\overline{G}$. However the values of activation energy seem to be quite reasonable compared with other experimental results: $U \cong 145$ K in $YBa_2Cu_4O_8$ [105],

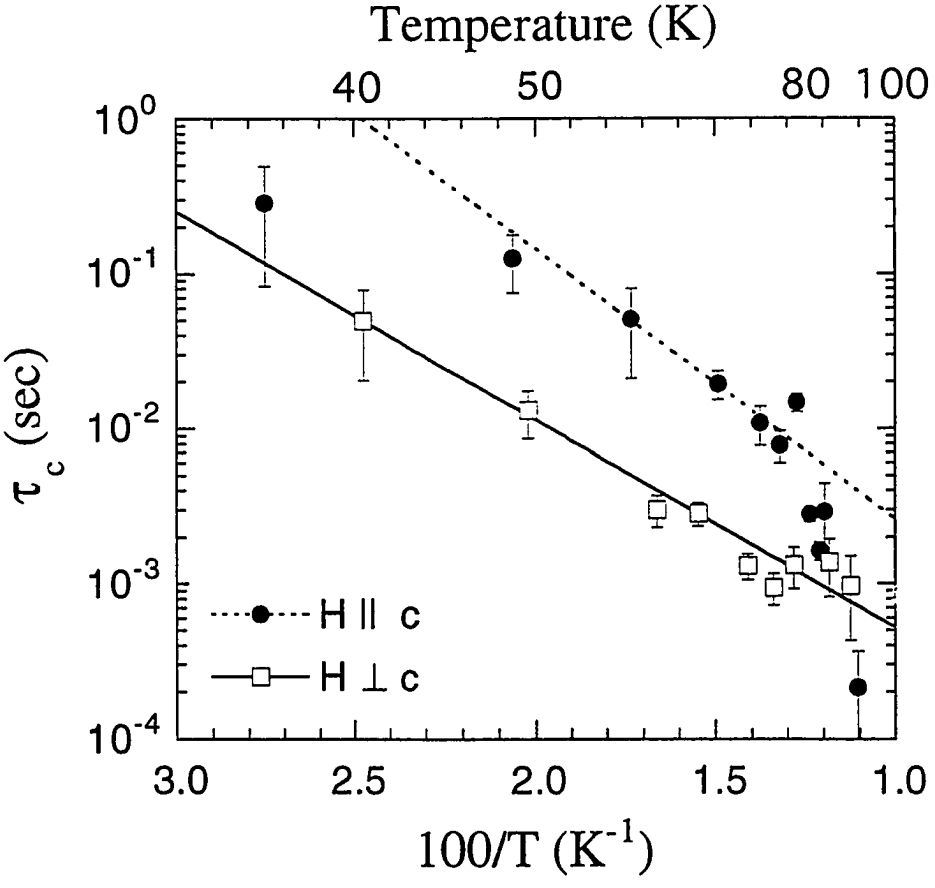

Fig. 5.5 The effective correlation time τ_c of the thermally excited vortex motion vs temperature in $YBa_2Cu_3O_7$ for $H = 8.2$ T and for the two orientations of the external field. The lines are fits to Eq. (5.9) in the text.

discussed previously, and $U \approx 100$ K in $HgBa_2CuO_{4+\delta}$, discussed in the next section. It is noted that systematic errors in the analysis would affect τ_0 but not the temperature dependence of τ_c. Thus we conclude that the activation energy obtained here are meaningful.

Now we discuss the recent ^{89}Y NMR measurement in YBCO reported by Song [113]. Using a 3-pulse sequence given by $\pi/2$ - t_1 - $\pi/2$ - τ_e - $\pi/2$ - t_2, he measured the ^{89}Y NMR spectra after the 2nd and 3rd pulses to test the change of the resonance frequency ω_L during the evolution time τ_e. He assumed the ω_L should be changed if the vortex moves during the time τ_e since the local field changes. However, as we showed, the vortex motion which gives rise to the change of the local field cannot change the whole field profile, or correspondingly the average of the field and the 2nd moment which determine the whole NMR spectrum. Thus although the vortices move and so the local field fluctuates in time, the resonance frequency, ω_L, cannot change whatever the characteristic time of the motion is. We conclude, contrary to Song's claim, that the 2D Fourier transform NMR plot of the resonance line is not a sensitive method to detect flux-line motion. On the other hand, he observed a faster decay in the ^{89}Y transverse magnetization for the longer τ_e. This effect is exactly the same as we observed in a TPSE. In fact, the sequence Song used is the so-called "stimulated echo" sequence originally found by Hahn [27]. This sequence generates five echoes and one of the echoes is called the "stimulated echo" positioned at $t = 2t_1 + \tau_e$. The decay of the stimulated echo is given by [114]

$$M(t_1, \tau_e) \propto \exp\left[-\left(\frac{\tau_e}{T_1} + \frac{2t_1}{T_2} + \frac{D\gamma^2 G^2 t_1^2 \tau_e}{3}\right)\right]. \tag{5.10}$$

Thus, the observation of the faster decay of $M(t_1,\tau_e)$ for the long τ_e indicates vortex motion with an effective diffusion constant D and in a field gradient G. It is noted that the effective diffusion contribution in a stimulated echo is dependent on a single exponential function of τ_e [see Eq. (5.10)] in contrast with the exponential t^3 dependence in a TPSE [see Eq. (5.6)]. Therefore the stimulated echo method is useful for the case of very slow motion and/or a

short T_2 if the field gradient is well defined during the measurement. Basically both the TPSE and stimulated echo sequence give the same information regarding the change of the local field in time in terms of an additional decay of the spin-echo amplitude. The observation of Song using the stimulated echo sequence is thus in agreement with our results for the vortex motion.

Alternative possible explanations for the effects we observed are considered below and shown to be inconsistent with the data. An enhancement of the ^{89}Y NMR echo decay rate below T_c was reported before [115] and attributed to the spin-flip suppression of unlike ^{63,65}Cu nuclear moments with a resultant increase of Y-Cu nuclear dipolar coupling. This interpretation predicts a monotonic increase of $(T_{2add})^{-1}$ below T_c rather than the maximum observed experimentally in Fig. 5.4. An ^{89}Y-^{89}Y pseudo-dipolar interaction via the charge carriers could be effective above T_c, similar to the discussion for ^{199}Hg in chapter 4. This indirect coupling could indeed contribute to the T_2 anisotropy above T_c. However, it could not explain the data below T_c since the opening of a superconducting gap could result in a decrease of $(T_{2add})^{-1}$ as observed for $(T_G)^{-1}$ of ^{199}Hg in $HgBa_2CuO_{4+\delta}$, discussed in chapter 4, but not an increase.

5.1.4 Conclusion

In conclusion, we have suggested a novel NMR method to investigate flux thermal motion. We have presented convincing experimental evidence that the effect is indeed observable in ^{89}Y echo decay rates in YBCO. From a quantitative fit of the data, the activated effective correlation times were derived which correspond to very slow components of the microscopic flux-line dynamics. This opens up the interesting possibility of comparison of the experimental results with hydrodynamic models in terms of statistical motion of polymer-like assemblies of parallel lines [116] and/or of collective low frequency-long wavelength modes of coupled vortices [101].

5.2 NMR Investigation of Thermally Activated Flux Motion in $HgBa_2CuO_{4+\delta}$ from ^{199}Hg Spin-Lattice Relaxation

5.2.1 Introduction

Regarding the nuclear spin-lattice relaxation (NSLR, T_1^{-1}, or R_1), evidence for a direct contribution due to thermally fluctuating FL's has been obtained only in an organic superconductor [117]. For HTSC the evidence remains highly uncertain after a characteristic T and H dependence of the ^{205}Tl NSLR in $Tl_2Ba_2CuO_4$, initially attributed to FL's motion [118], has been shown to be present also above T_c [119].

The contribution to R_1 due to FL's motion should be particularly prominent around the irreversibility temperature T_{irr} where the correlation time τ_c of the FL's motion should cross, as a function of temperature, the value of the reciprocal Larmor frequency ω_L, i.e. $\tau_c\omega_L \approx 1$, for which R_1 is maximum. The second condition to be met is that the NSLR of the nucleus investigated should not be dominated by other sources of relaxation.

In this section, we report ^{199}Hg nuclear spin-lattice relaxation rate (T_1^{-1}, R_1) studies in an oriented powder sample of $HgBa_2CuO_{4+\delta}$ (T_c = 96 K) for temperatures $10 \leq T \leq 300$ K and static magnetic fields H = 5.9, 8.2 and 9.4 Tesla. We have observed a strongly field dependent anisotropy of R_1 present only in a temperature interval of 10 - 50 K around the irreversibility line which was measured in the same sample used for NMR measurements. The anisotropy can be attributed to the contribution to the NSLR from thermally fluctuating FL's present only for the orientation of the crystals with H perpendicular to the CuO_2 plane. We could fit the data with an expression for R_1 derived for a simple model of FL's diffusive motion with a restoring force. The effective correlation time τ_c of the excitation

at wave length of the order of the intervortex distance obtained from the fit, is thermally activated with an effective activation energy, $U \propto 1/H$.

5.2.2 Results and Discussions

The measurements were performed in a single-phase powder sample with average grain size 12 - 20 μm. The grains were imbedded in epoxy and oriented in a magnetic field to achieve the alignment of the grains along a common crystal c axis. X-ray diffraction and DC magnetization were performed to test the sample alignment, to determine the sample quality, and to measure $T_c = 96$ K. Details are given in section 4.1. The irreversibility temperature shown in Fig. 5.6 was measured (at Ames Laboratory by J. Sok) as a function of the applied field up to 5.5 Tesla using a SQUID magnetometer. T_{irr} was chosen as the temperature at which the field-cooled and zero-field-cooled magnetizations depart from each other.

The ^{199}Hg NMR measurements were performed with Fourier transform (FT) spectrometers at 5.9 , 8.2, and 9.4 T. Typical $\pi/2$ radio frequency pulses were 4 μs corresponding to $H_1 \cong 80$ G sufficient to irradiate the whole NMR line with the exception of the lowest temperatures ($T < 20$ K). From an inversion recovery sequence π - $\pi/2$ a single exponential was obtained yielding R_1. Some measurements were performed with weaker radio frequency fields, $H \sim 30$ G, using a long sequence of saturating pulses. The results of R_1 versus temperature at three different fields are shown in Figs. 5.7 and 5.8. Above T_c the relaxation rate is field and orientation independent and R_1 follows a Korringa-type behavior T_1T = constant. Below T_c, R_1 remains isotropic except for the temperature interval 10 - 50 K where an extra contribution appears to be present for $\boldsymbol{H} \parallel \boldsymbol{c}$ (see the inset of Fig. 5.7).

The extra contribution has a maximum which shifts in temperature by changing the applied magnetic field (see Fig. 5.8). The temperature and field-dependent anisotropy of R_1

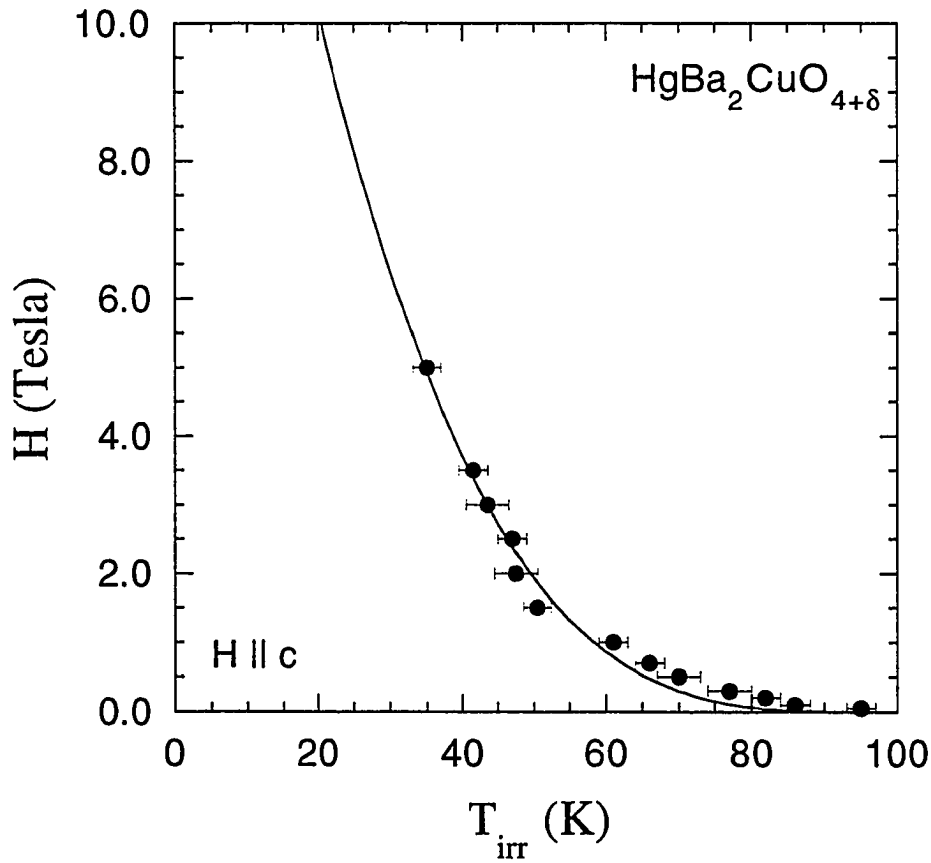

Fig. 5.6 The irreversibility line in oriented $HgBa_2CuO_{4+\delta}$ powder for $H \parallel c$. The solid curve is a fit to $H = 22(1\text{-}T_{irr}/96\ \text{K})^{3.3}$ Tesla. (Courtesy of J. Sok)

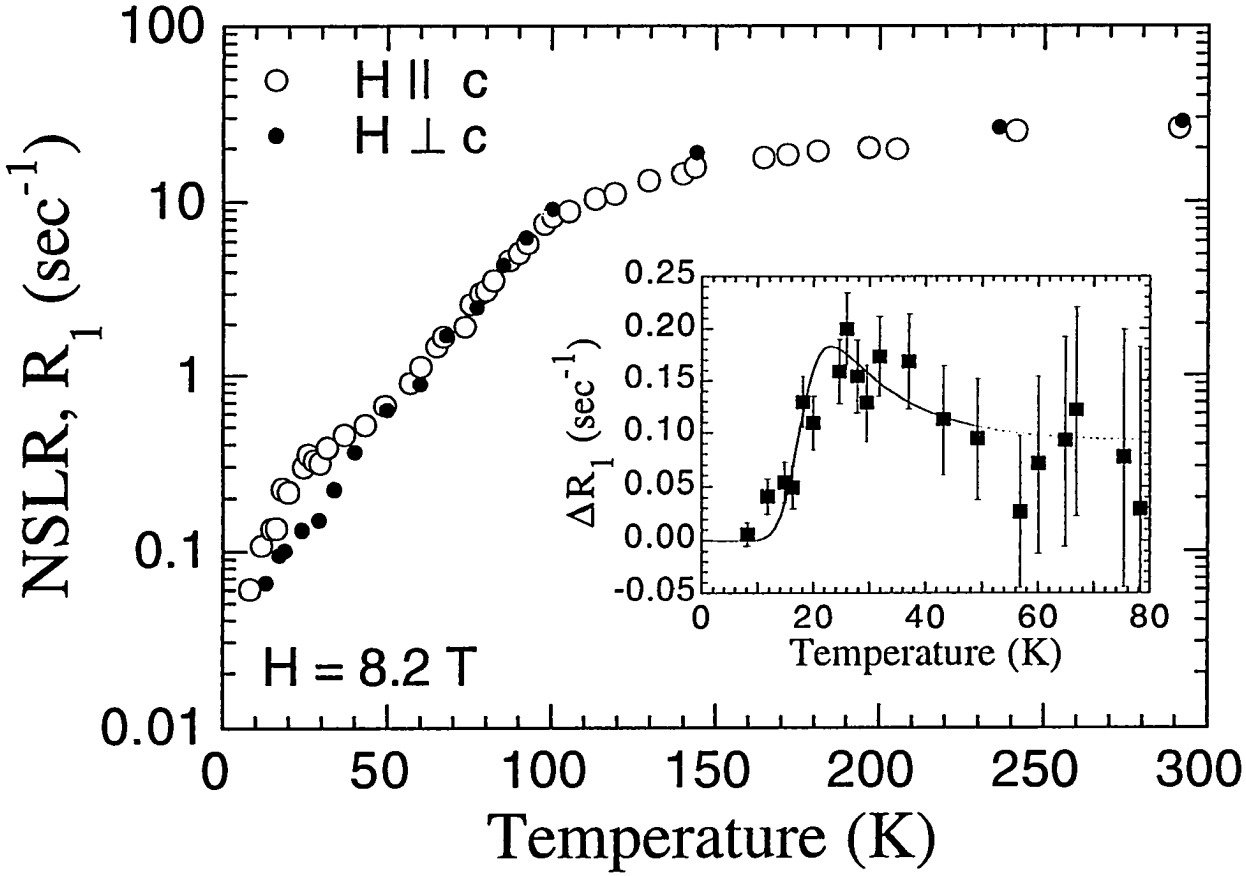

Fig. 5.7 Temperature dependence of ^{199}Hg NSLR, R_1, in oriented $HgBa_2CuO_{4+\delta}$ powder for $H = 8.2$ T. The inset shows the temperature dependence of the extra contribution to the R_1 for $H \parallel c$ obtained by subtracting the interpolated value of R_1 data for $H \perp c$ from the R_1 for $H \parallel c$. The solid curve is a fit of the extra R_1 data using Eq. (6) (see the text for details).

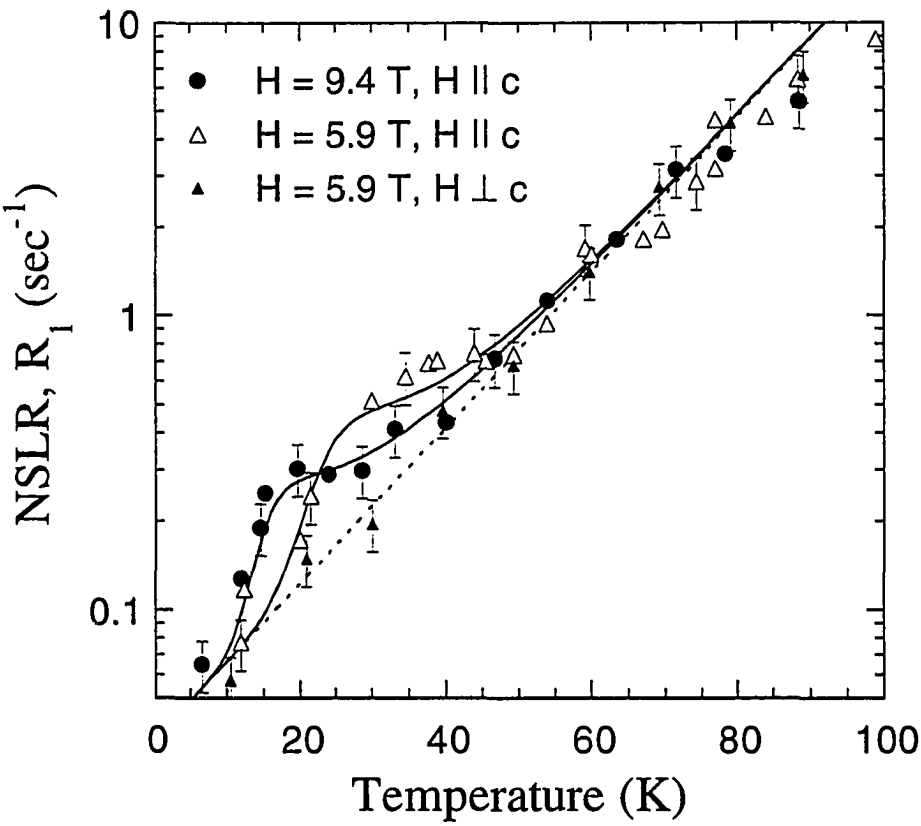

Fig. 5.8 Plot of ^{199}Hg R_1 vs T in oriented $HgBa_2CuO_{4+\delta}$ powder for two magnetic field intensities. The dashed line is the interpolation of the data of R_1 for $\boldsymbol{H} \perp \boldsymbol{c}$, yielding the background $R_1 = 0.036\exp[0.061T(\mathrm{K})]$ sec^{-1}. The solid curves are the theoretical curves obtained by adding the FL's contribution from Eq. (5.16) to the background obtained from the data for $\boldsymbol{H} \perp \boldsymbol{c}$ (see the text for details).

observed here are quite different from the ones observed in $YBa_2Cu_3O_7$ [120,121] and $YBa_2Cu_4O_8$ [122] for the relaxation due to the interaction with the Fermi liquid. Moreover, our results are inconsistent with a contribution due to fast relaxation within the vortex core nuclei in the superconducting region [99]. In fact in the rapid diffusion limit one has [123] $R_{1s} = R_{1n}H\xi^2/\Phi_0$ where R_{1s} and R_{1n} are the NSLR in the superconducting and normal phases, respectively. With $\Phi_0 = 2.07\times10^{-7}$ G cm^2, $\xi_{ab} = 20$ Å and $R_{1n} = 0.1T$ sec^{-1} (from Fig. 5.7) one has $R_{1s} = 2\times10^{-8}\,HT$ sec^{-1}. This estimate has the wrong order of magnitude and predicts an H and T dependence which is not observed here.

Instead, our results are quite consistent with a direct contribution to relaxation due to FL's random thermal motion. The anisotropy is due to the fact, already observed in organic superconductors [117], that for $\boldsymbol{H} \perp \boldsymbol{c}$ and with the a coherence length ξ_c of the order of the interplane spacing s in a strongly anisotropic superconductor, the FL's are self trapped between the superconducting planes and thus do not contribute to the NMR relaxation. Furthermore, the FL's contribution to R_1 (T_1^{-1}) for $\boldsymbol{H} \parallel \boldsymbol{c}$ shifts with $\boldsymbol{H}$ in the same direction as the irreversibility temperature (see Figs. 5.6 and 5.8).

We proceed now to calculate the FL's contribution to relaxation with a simple model applicable to highly anisotropic HTSC. The relaxation rate due to the fluctuating local field is obtained from time dependent perturbation theory as [see Eq. (2.14)]:

$$R_1 = \frac{1}{T_1} = \frac{1}{2}\gamma_N^2 \int_{-\infty}^{+\infty} \langle h_\perp(t) h_\perp(0) \rangle e^{-i\omega_L t} dt\,, \tag{5.11}$$

where γ_N is the nuclear gyromagnetic ratio, ω_L is the Larmor frequency and $h_\perp$ is the local field perpendicular to the applied field $\boldsymbol{H}$. By referring to a model of a stack of superconducting planes of thickness d and the interplane spacing s, the transverse field component for a single pancake vortex is, in cylindrical coordinates [60]:

$$h_{\perp}(\rho,z) = \frac{\Phi_0}{4\pi\lambda^2}\frac{d}{\rho}\left[\frac{z}{|z|}\exp\left(-\frac{z}{\lambda_{\parallel}}\right) - \frac{z}{\sqrt{\rho^2+z_n^2}}\exp\left(-\frac{\sqrt{\rho^2+z_n^2}}{\lambda_{\parallel}}\right)\right] \cong \frac{\Phi_0}{4\pi\lambda^2}\frac{d}{\rho}, \tag{5.12}$$

where λ is the bulk London penetration length $\lambda = \sqrt{d/s}\lambda_{\parallel}$ and z_n is the z coordinate of the n-th layer. Since the average intervortex distance $l_e = \frac{2}{\sqrt[4]{3}}\sqrt{\Phi_0/B}$ is much smaller than $\lambda_{\parallel}$ for the B fields used here we have simplified Eq. (5.12) by assuming $\rho, z << \lambda_{\parallel}$. We limit z_n to the two Cu planes above and below a given ^{199}Hg nucleus, i.e. $z_n = s/2 = d$. Equation (5.12) is valid only for $\rho >> s, \xi$.

Thus, assuming that the thermal motion involves fluctuations of the equilibrium position of the FL which is a small fraction of the intervortex spacing l_e we can write: $h_{\perp}(\rho(t)) \cong h_{\perp}(\rho) + [\partial h_{\perp}(\rho)/\partial\rho]_{\rho}\delta\rho(t)$. From Eqs. (5.11) and (5.12) and taking an ensemble average over ρ from ξ up to $l_e/2$ one can write for the uncorrelated fluctuation of two pancake vortices in the plane above and below a given ^{199}Hg nucleus:

$$R_1 \cong \frac{\gamma_N^2\Phi_0^2}{8\pi\sqrt{3}\lambda^4}\frac{d^2\langle u^2\rangle}{l_e^2\xi^2}\int_{-\infty}^{+\infty} g(t)\exp(-i\omega_L t)dt, \tag{5.13}$$

where the mean square fluctuation amplitude of the center of the FL core with respect to the equilibrium position can be expressed as [101]:

$$\langle|\delta\rho(0)|^2\rangle = \langle u^2\rangle = \frac{16\pi\lambda_{\parallel}^2 k_B T}{s\Phi_0 B}\ln\left(\frac{\pi B\lambda_{\parallel}^2}{\Phi_0\ln\left(\frac{l_e}{s}\right)}\right). \tag{5.14}$$

For $s = 9.5$ Å, reduces to $\langle u^2\rangle/l_e^2 = 7 \times 10^6 \lambda_\parallel^2 T$ with a negligible field dependence in the range $H = 5.9$ - 9.4 Tesla. The correlation function (CF) $g(t)$ contains the information on the FL dynamics. Above the irreversibility line the FL's should undergo thermally activated hopping. Thus it is reasonable to assume a model of two dimensional diffusive-like random motion under a restoring force. We write the CF as a sum over q of collective components of the form $\exp(-Dq^2t)$ with D an effective diffusivity constant and Dq^2 the width of the central component in the spectrum of the FL's excitations. The normalized spectral density becomes:

$$j(\omega) = \int_{-\infty}^{+\infty} g(t)\exp(-i\omega t)dt = \frac{1}{N}\sum_q \frac{2Dq^2}{(Dq^2)^2 + \omega^2} = \tau_D \ln\left(\frac{\tau_D^{-2} + \omega^2}{\omega^2}\right), \qquad (5.15)$$

where we have integrated over q in two dimensions up to $q_m = \frac{\sqrt{8\pi}}{\sqrt[4]{3}}(1/l_e)$ (in a triangular lattice) and set $\tau_D = (Dq_m^2)^{-1}$. Finally from Eqs. (5.13) and (5.15) one has

$$R_1 \cong \frac{\gamma_N^2 \Phi_0^2}{8\pi\sqrt{3}\lambda^4} \frac{d^2\langle u^2\rangle_{irr}}{l_e^2 \xi^2}\left(\frac{T}{T_{irr}}\right)\tau_D \ln\left(\frac{\tau_D^{-2} + \omega_L^2}{\omega_L^2}\right), \qquad (5.16)$$

where $\langle u^2\rangle_{irr}$ is the value at $T = T_{irr}$.

Since the FL's contribution to R_1 is present only for $\boldsymbol{H} \parallel \boldsymbol{c}$ we assume as background contribution the experimental data for $\boldsymbol{H} \perp \boldsymbol{c}$. In Fig. 5.7 inset and Fig. 5.8 we show the theoretical curves obtained by adding the FL's contribution from Eq. (5.16) to the background contribution obtained by interpolating the data of R_1 for $\boldsymbol{H} \perp \boldsymbol{c}$. To obtain a good fit of the data we assume in Eq. (5.16) $\tau_c = \tau_D = \tau_0 \exp(U/T)$ and set $A = \left(\gamma_N^2 \Phi_0^2 / 8\pi\sqrt{3}\lambda^4\right)\left(d^2\langle u^2\rangle_{irr}/\xi^2 l_e^2\right)$ as a fitting parameter. We obtain $A \cong 10^8$ (rad/sec)^2 and $\tau_0 \cong 10^{-11}$ sec for all three curves while the activation energy U is found to be inversely

proportional to H as shown in Fig. 5.9. Although the values of the parameters are only indicative due to the relatively small FL's contribution to the total R_1 and the presence of three fitting parameters, it is encouraging that their order of magnitude is quite reasonable. From Eq. (5.14) one has $\langle u^2 \rangle_{irr}/l_e^2 = 2.4 \times 10^{-2}$ for $\lambda_{\|} \cong 1500$ Å and $T_{irr} = 31$ K (at $H = 5.9$ Tesla). Thus by taking $d = s/2 = 4.75$ Å and $\xi \cong 20$ Å one can estimate the theoretical value $A \cong 5 \times 10^9$ (rad/sec)^2. The calculation which leads to Eq. (5.16) overestimates the effect of fluctuations by considering the pancakes completely uncorrelated along the c-direction. An even small degree of correlation between planes would reduce drastically the transverse field in Eq. (5.12) [60]. Thus the calculated value of A is not unreasonable.

5.2.3 Conclusions

Having established that the ^{199}Hg NSLR contains a measurable contribution from thermal FL's motion for $\boldsymbol{H} \| \boldsymbol{c}$ we conclude by comparing the parameters obtained here with the ones extracted from macroscopic magnetic and transport measurements [124]. In doing so one should keep in mind that NMR probes the spontaneous fluctuations associated with FL thermal hopping motion while other techniques probe dissipation effects related to the same FL dynamics. At the irreversibility line we find a smooth change of the correlation time consistent with continuous thermal depinning with a microscopic hopping time $\tau_c = 5 \times 10^{-8}$ sec. The prefactor τ_0 and the activation energy found here are of the same order of magnitude as found from dissipative flux motion in the thermally activated flux creep model for HTSC of similar anisotropy [125]. The simple field dependence $U \propto 1/H$ of the activation energy (in Fig. 5.9) was derived on the ground of physical arguments [126] but experimentally one often finds more complicated H-dependences [125,127]. For pancake vortices in anisotropic HTSC and for $\boldsymbol{H} \| \boldsymbol{c}$ it was shown [128] that the characteristic value of U depends strongly on the strength of the interlayer coupling with U becoming equal to the field independent intrinsic pinning energy U_p only for the highly

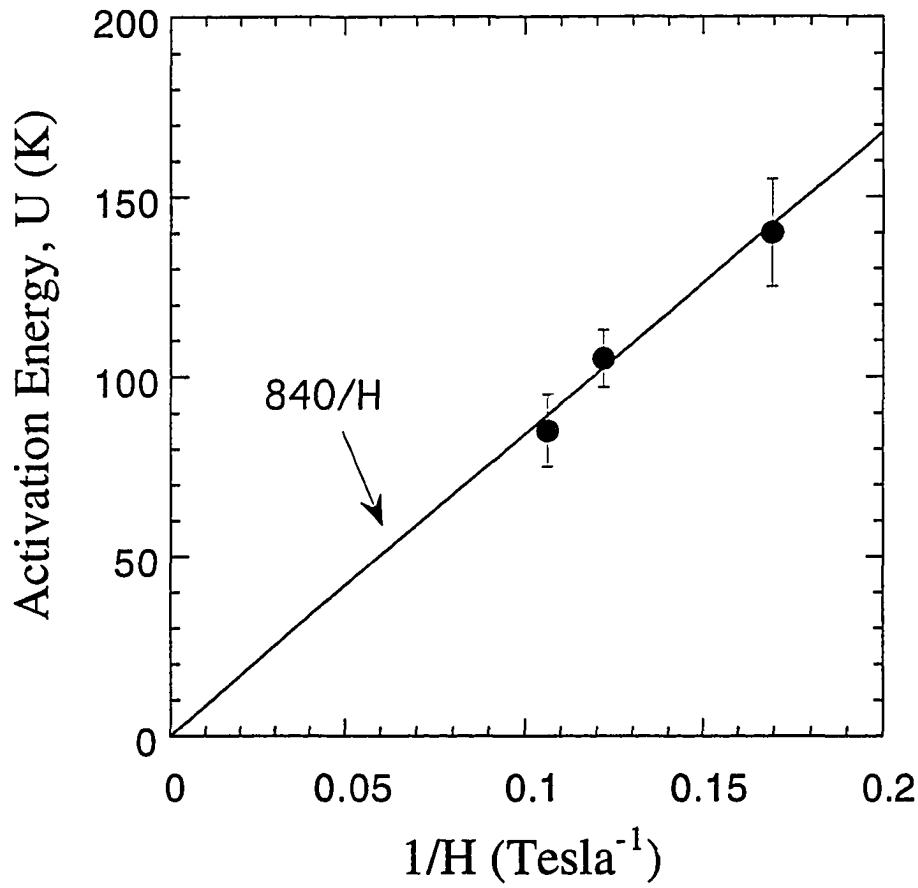

Fig. 5.9 Magnetic field dependence of the effective activation energy, U obtained by ^{199}Hg NSLR in oriented $HgBa_2CuO_{4+\delta}$ powder. The line is a fit to $U = 840/B(T)$ in unit of K.

anisotropic HTSC. In the case where the Josephson interlayer coupling is not negligible one may have a field dependent effective U for a flux bundle although the simple $1/H$ form is difficult to justify. We may thus tentatively conclude that the parameters derived near T_{irr} from the present NSLR experiment represent a thermally activated hopping motion of bundles of pancake vortices with non-negligible interlayer coupling.

6. SUMMARY AND CONCLUSIONS

This thesis has been devoted to three important aspects of HTSC research: (i) the dynamics and correlations of the Cu^{2+} spins in the parent compounds of HTSC which are predominantly antiferromagnetic insulators, (ii) the properties of the Fermi-liquid in the normal and in the superconducting state, and (iii) the thermally activated fluctuations of the flux lines in HTSC. For the investigation of the above aspects, the NMR technique, as a microscopic probe, was applied to obtain the information on the static and dynamical properties of the local hyperfine interactions and/or the local field in the system studied. In addition, since all the experiments were performed on high quality single crystals and/or orientated powder samples, novel effects could be discovered by analyzing the orientation-dependence of the NMR parameters. In general, we could explain our data quite quantitatively in every experiment and correspondingly, could describe the individual systems quite successfully. We conclude this thesis with a brief summary and some remarks for each investigation separately.

First, the spin dynamics and its correlations in a parent compound of HTSC, $Sr_2CuO_2Cl_2$ which is a weakly anisotropic 2D antiferromagnet, have been studied using ^{35}Cl NMR. We have demonstrated for the first time the occurrence of crossover effects in the correlations of the spin dynamics. By introducing a field-induced anisotropy we have explained the field-dependent 3D ordering temperature T_N. Generally our data could be explained quantitatively in terms of crossover effects near T_N due to the XY-like and/or the field-induced Ising-like anisotropy. Thus we have described the spin dynamics and its correlations in the spin $S = 1/2$ 2DSLHA quite completely.

Second, NMR investigations of two distinct superconductors, $HgBa_2CuO_{4+\delta}$ and YNi_2B_2C, have been reported and discussed. The investigation has concentrated on the

Fermi-liquid behavior both in the normal and in the superconducting state. From analyzing NMR data we have extracted the temperature dependence of the spin susceptibility. As a result, we conclude that $HgBa_2CuO_{4+\delta}$ is characterized by the *d*-wave pairing symmetry, whereas YNi_2B_2C is a conventional BCS-type superconductor. In particular, by testing the Korringa relation of ^{11}B NMR in YNi_2B_2C, we arrived at the conclusion that the antiferromagnetic fluctuations of localized or itinerant electron spins on the Ni sublattice are negligible, contrary to HTSC. By presenting these NMR measurements, we have demonstrated the power of NMR which can give direct information on the density of carriers, the spin susceptibility of the Fermi-liquid, and if any, the magnetic character of localized spins.

Finally, we have presented NMR measurements performed on two representative HTSC compounds, $YBa_2Cu_3O_7$ and $HgBa_2CuO_{4+\delta}$, aimed at the investigation of the thermally activated vortex motion. Additional relaxations in ^{89}Y T_2^{-1} for $YBa_2Cu_3O_7$ and ^{199}Hg T_1^{-1}, R_1, for $HgBa_2CuO_{4+\delta}$ were observed and explained quantitatively in terms of the thermal fluctuations of flux lines. Adopting simple models describing the thermally activated fluctuations of flux lines, we obtained a reasonable set of effective correlation time τ_c and effective activation energy U of the flux-line motion. These pioneering works have proved that the NMR technique is a useful probe of the microscopic motion of flux lines in the superconducting state and open up a new field of NMR application.

REFERENCES

[1] J. G. Bednorz and K. A. Müller, Z. Phys. B **64**, 189 (1986).

[2] A. Abragam, *Principles of Nuclear Magnetism* (Oxford, Clarendon, 1961).

[3] C. P. Slichter, *Principles of Magnetic Resonance*, 3rd ed. (Springer, Berlin, 1990).

[4] M. Mehring, in *Applied Magnetic Resonance* (Springer, Wien, 1992), Vol. **3**, p. 383.

[5] D. Brinkmann and M. Mali, in *NMR-Basic Principles and Progress* (Springer, Berlin, 1994), Vol. **31**, p.171.

[6] F. Borsa, P. Carretta, M. Corti, and A. Rigamonti, in *Applied Magnetic Resonance* (Springer, Wien, 1992), Vol. **3**, p. 509.

[7] F. Borsa, P. Carretta, F. Cintolesi, M. Corti, A. Rigamonti, B. J. Suh, and D. R. Torgeson, in *Applied Magnetic Resonance* (Springer, Wien, in press).

[8] N. Bloembergen and T. J. Rowland, Acta Met. **1**, 731 (1953); erratum Acta Met. **3**, 74 (1955).

[9] C. H. Townes, C. Herring, and W. D. Knight, Phys. Rev. **77**, 852 (1950).

[10] B. J. Suh, F. Borsa, J. Sok, D. R. Torgeson, M. Corti, A. Rigamonti, and Q. Xiong (unpublished).

[11] J. Korringa, Physica **16**, 601 (1950).

[12] G. C. Carter, L. H. Bennett, and D. J. Kahan, *Metallic Shifts in NMR* (Pergamon, New York, 1977), Pt. **I**.

[13] T. Moriya, J. Phys. Soc. Jpn. **18**, 516 (1963).

[14] A. Millis, H. Monien, and D. Pines, Phys. Rev. B **42**, 167 (1990).

[15] C. H. Pennington, D. J. Durand, C. P. Slichter, J. P. Rice, E. D. Bukowski, and D. M. Ginsberg, Phys. Rev. B **39**, 274 (1989).

[16] Y. Itoh, H. Yasuoka, Y. Fujiwara, Y. Ueda, T. Machi, I. Tomeno, K. Tai, N. Koshizuka, and S. Tanaka, J. Phys. Soc. Jpn. **61**, 1287 (1992).

[17] C. H. Pennington and C. P. Slichter, Phys. Rev. Lett. **66**, 381 (1991).

[18] T. Imai, C. P. Slichter, A. P. Paulikas and B. Veal, Phys. Rev. B **47**, 9158 (1993).

[19] R. Stern, M. Mali, I. Magelschots, J. Roos, D. Brinkmann, J.-Y. Genoud, T. Graf, and J. Muller, Phys. Rev. B **50**, 426 (1994); R. Stern, M. Mali, J. Roos, and D. Brinkmann, (unpublished).

[20] F. Borsa, M. Corti, T. Goto, A. Rigamonti, D. C. Johnston, and F. C. Chou, Phys. Rev. B **45**, 5756 (1992).

[21] F. Borsa and A. Rigamonti, in *Magnetic Resonance at Phase Transitions*, edited by C. P. Poole, Jr., F. J. Owens, and H. A. Farach (Academic, New York, 1979), p. 790.

[22] P. C. Hohenberg and B. I. Halperin, Rev. Mod. Phys. **49**, 435 (1977).

[23] T. Moriya, Prog. Theor. Phys. **16**, 23 (1956); **28**, 371 (1962).

[24] B. J. Suh, F. Borsa, L. L. Miller, M. Corti, D. C. Johnston, and D. R. Torgeson, Phys. Rev. Lett. **75**, 2212 (1995).

[25] D. J. Adduci and B. C. Gerstein, Rev. Sci. Instrum. **50**, 1403 (1979).

[26] D. J. Adduci, P. A. Hornung, and D. R. Torgeson, Rev. Sci. Instrum. **47**, 1503 (1976).

[27] E. L. Hahn, Phys. Rev. **80**, 580 (1950).

[28] H. Y. Carr and E. M. Purcell, Phys. Rev. **94**, 630 (1954).

[29] S. Meiboom and D. Gill, Rev. Sci. Instrum. **94**, 688 (1958).

[30] B. J. Suh, F. Borsa, and D. R. Torgeson, J. Magn. Reson. A **110**, 58 (1994).

[31] B. J. Suh, D. R. Torgeson, and F. Borsa, Phys. Rev. Lett. **71**, 3011 (1993).

[32] A. Narath, Phys. Rev. **162**, 320 (1967).

[33] L. L. Miller, X. L. Wang, S. X. Wang, C. Stassis, D. C. Johnston, J. Faber, Jr., and C.-K. Loong, Phys. Rev. B **41**, 1921 (1990).

[34] D. Vaknin, S. K. Sinha, C. Stassis, L. L. Miller, and D. C. Johnston, Phys. Rev. B **41**, 1926 (1990).

[35] L. P. Le, G. M. Luke, B. J. Sternlieb, Y. J. Uemura, J. H. Brewer, T. H. Riseman, D. C. Johnston, and L. L. Miller, Phys. Rev. B **42**, 2182 (1990).

[36] D. C. Johnston, J. Magn. Magn. Mater. **100**, 218 (1991).

[37] E. Manousakis, Rev. Mod. Phys. **63**, 1 (1991).

[38] B. Keimer, N. Belk, R. J. Birgeneau, A. Cassanho, C. Y. Chen, M. Greven, M. A. Kastner, A. Aharony, Y. Endoh, R. W. Erwin, and G. Shirane, Phys. Rev. B **46**, 14034 (1992).

[39] M. Matsuda, K. Yamada, K. Kakurai, H. Kadowaki, T. R. Thurston, P. M. Gehring, A. H. Moudden, and G. Shirane, Phys. Rev. B **42**, 10098 (1990).

[40] M. S. Makivic' and H.-Q. Ding, Phys. Rev. B **43**, 3562 (1991).

[41] H.-Q. Ding, Phys. Rev. Lett. **68**, 1927 (1992).

[42] M. Greven, R. J. Birgeneau, Y. Endoh, M. A. Kastner, B. Keimer, M. Matsuda, G. Shirane, and T. R. Thurston, Phys. Rev. Lett. **72**, 1096 (1994); Z. Phys. B **96**, 465 (1995).

[43] T. Thio and A. Aharony, Phys. Rev. Lett. **73**, 894 (1994).

[44] M. Corti, F. Borsa, L. L. Miller, and A. Rigamonti, J. Appl. Phys. **75**, 7146 (1994).

[45] T. Yildirim, A. B. Harris, O. Entin-Wohlman, A. Aharony, Phys. Rev. Lett. **72**, 3710 (1994).

[46] H. J. M. De Groot and L. J. De Jongh, in *Magnetic Properties of Layered Transition Metal Compounds*, edited by L. J. de Jongh (Kluwer, Dordrecht, 1990), p. 379.

[47] Y. Okabe and M. Kikuchi, J. Phys. Soc. Jpn. **57**, 4351 (1988).

[48] We infer that the suggestion in [33], that the minimum in χ_c at ~ 300 K corresponds to T_N, is not correct.

[49] See for example: H. Benner and J. P. Boucher, in *Magnetic Properties of Layered Transition Metal Compounds*, edited by L. J. de Jongh (Kluwer, Dordrecht, 1990), p. 323.

[50] D. Hone and A. Pires, Phys. Rev. B **15**, 323 (1977).

[51] F. Borsa, J. P. Boucher, and J. Villain, J. Appl. Phys. **49**, 1326 (1978).

[52] J. P. Boucher, Solid State Commun. **33**, 1025 (1980).

[53] D. Vaknin et al., (unpublished).

[54] J. L. Wagner, P. G. Radaelli, D. G. Hinks, J. D. Jorgensen, J. F. Mitchell, B. Dabrowski, G. S. Knapp, and H. A. Beno, Physica C **210**, 447 (1993).

[55] B. J. Suh, F. Borsa, Ming Xu, D. R. Torgeson, W. J. Zhu, Y. Z. Huang, and Z. X. Zhao, Phys. Rev. B **50**, 651 (1994).

[56] M. Horvatic', C. Berthier, P. Carretta, J. A. Giller, P. Ségransan, Y. Berthier, and J. J. Capponi, Physica C **235-240**, 1669 (1994).

[57] Q. Xiong, Y. Y. Xue, Y. Cao, F. Chen, Y. Y. Sun, J. Gibson, C. W. Chu, L. M. Liu, and A. Jacobson, Phys. Rev. B **50**, 10346 (1994).

[58] Q. Xiong, Y. Y. Xue, F. Chen, Y. Cao, Y. Y. Sun, L. M. Liu, A. J. Jacobson, and C. W. Chu, Physica C **231**, 233 (1994)

[59] H. Alloul, A. Mahajan, H. Casalta, and O. Klein, Phys. Rev. Lett. **70**, 1171 (1993).

[60] J. R. Clem, Phys. Rev. B **43**, 7837 (1991).

[61] Y.-Q. Song, S. Tripp, W. P. Halperin, L. Tonge, and T. J. Marks, Phys. Rev. B **50**, 16570 (1994).

[62] M. Takigawa, A. P. Reyes, P. C. Hammel, J. D. Thompson, R. H. Heffner, Z. Fisk, and K. C. Ott, Phys. Rev. B **43**, 247 (1991).

[63] H. Alloul, T. Ohno, and P. Mendels, Phys. Rev. Lett. **63**, 1700 (1989).

[64] M. Bankay, M. Mali, J. Roos, and D. Brinkmann, Phys. Rev. B **50**, 6416 (1994).

[65] R. E. Walstedt, B. S. Shastry, and S. -W. Cheong, Phys. Rev. Lett. **72**, 3610 (1994).

[66] F. Borsa and A. Rigamonti, Nuovo Cimento **48**, 194 (1967).

[67] N. Bloembergen and T. J. Rowland, Phys. Rev. **97**, 1679 (1955).

[68] M. A. Ruderman and C. Kittel, Phys. Rev. **96**, 99 (1954).

[69] A. Sokol and D. Pines, Phys. Rev. Lett. **71**, 2813 (1993).

[70] R. M. White, *Quantum Theory of Magnetism*, 2nd ed. (Springer, Berlin, 1983), p. 116.

[71] A. J. Leggett, Rev. Mod. Phys. **47**, 331 (1975).

[72] A. Sudbø, S. Chakravarty, S. Strong, and P. W. Anderson, Phys. Rev. **49**, 12245 (1994).

[73] N. Bulut and D. J. Scalapino, Phys. Rev. Lett. **68**, 706 (1992).

[74] Jun Chen, J. F. Zasadzinski, K. E. Grey, J. L. Wagner, and D. G. Hinks, Phys. Rev. B **49**, 3683 (1994).

[75] J. A. Martindale, S. E. Barrett, K. E. O'Hara, C. P. Slichter, W. C. Lee, and D. M. Ginsberg, Phys. Rev. B **47**, 9155 (1993).

[76] K. Ishida, Y. Kitaoka, K. Asayama, K. Kadowaki, and T. Mochiku, J. Phy. Soc. Jpn. **63**, 1104 (1994).

[77] M. Takigawa and D. B. Mitzi, Phys. Rev. Lett. **73**, 1287 (1994).

[78] N. Nagarajan, C. Mazumdar, Z. Hossain, S. K. Dhar, K. V. Gopalakrishnan, L. C. Gupta, C. Godart, B. D. Padalia, and R. Vijayaraghavan, Phys. Rev. Lett. **72**, 274 (1994).

[79] R. J. Cava, H. Takagi, H. W. Zandbergen, J. J. Krajewski, W. F. Peck, Jr., T. Siegrist, B. Batlogg, R. B. von Dover, R. J. Felder, K. Mizuhashi, J. O. Lee, H. Eisaki, and S. Uchida, Nature **367**, 252 (1994).

[80] H. C. Ku, C. C. Lai, Y. B. You, J. H. Shieh, and W. Y. Guan, Phys. Rev. B **50**, 351 (1994).

[81] J. L. Sarrao, M. C. de Andrade, J. Herrmann, S. H. Han, Z. Fisk, M. B. Maple, and R. J. Cava, Physica C **229**, 65 (1994).

[82] B. K. Cho, P. C. Canfield, and D. C. Johnston, Phys. Rev. B **52**, 3844 (1995).

[83] T. Siegrist, H. W. Zandbergen, R. J. Cava, J. J. Krajewski, and W. F. Peck. Jr., Nature **367**, 254 (1994).

[84] F. Borsa, Q. Hu, K. H. Kim, B. J. Suh, D. R. Torgeson, P. C. Canfield, M. Xu, and B. Zhong, Physica C **235-240**, 2547 (1994).

[85] M. E. Hanson, F. Lefloch, W. H. Wong, W. G. Clark, M. D. Lan, C. C. Hoellwarth, P. Klavins, and R. N. Shelton, Phys. Rev. B **51**, 674 (1995).

[86] K. Ikushima, J. Kikuchi, H. Yasuoka, R. J. Cava, H. Takagi, J. J. Krajewski, and W. W. Peck, Jr., J. Phys. Soc. Jpn. **63**, 2878 (1994).

[87] T. Kohara, T. Oda, K. Ueda, Y. Yamada, A. Mahajan, K. Elankumaran, Z. Hossian, L. C. Gupta, R. Nagarajan, R. Vijayaraghaven, and C. Mazumdar, Phys. Rev. B **51**, 3985 (1995).

[88] L. F. Mattheiss, Phys. Rev. B **49**, 13279 (1994).

[89] W. E. Pickett and D. J. Singh, Phys. Rev. Lett. **72**, 3702 (1994).

[90] J. I. Lee, T. S. Zhao, I. G. Kim, B. I. Min, and S. J. Youn, Phys. Rev. B **50**, 4030 (1994).

[91] B. K. Cho, P. C. Canfield, L. L. Miller, D. C. Johnston, W. P. Beyermann, and A. Yatskar, Phys. Rev. B **52**, 3684 (1995).

[92] B. K. Cho, Ph. D. Thesis, Iowa State University, 1995, (unpublished).

[93] S. Chikazumi, *Physics of Magnetism* (R. E. Krieger Pub., Huntington, 1978).

[94] P. W. Selwood, *Magnetochemistry*, 2nd ed. (Interscience, New York, 1956), p. 78.

[95] N. W. Ashcroft and N. D. Mermin, *Solid State Physics* (Holt, Rinehart and Winston, New York, 1976).

[96] J. Y. Rhee, X. Wang, and B. N. Harmon, Phys. Rev. B **51**, 15585 (1995).

[97] T. P. Das and E. L. Hahn, in *Nuclear Quadrupole Resonance Spectroscopy*, Suppl. 1, Solid State Physics Series, edited by Seitz and Turnbull (Academic, New York, 1958).

[98] L. C. Hebel and C. P. Slichter, Phys. Rev. **113,** 1504 (1959).

[99] D. E. MacLaughlin, in *Solid State Physics*, edited by H. Ehrenreich, F. Seitz, and D. Turnbull, (Academic, New York, 1976), Vol. **31**, p. 34.

[99a] B. J. Suh, F. Borsa, D. R. Torgeson, B. K. Cho, P. C. Canfield, D. C. Johnston, J. Y. Rhee, B. N. Harmon, (unpublished).

[100] See for example: J. R. Clem, "Aisotropic Superconductors: Fundamental of Vortices in Layered Superconductors" in *Vortices in Superconductors*, edited by N. Bontemps (Kluwer, Netherlands, 1993) and references therein.

[101] H. E. Brandt, Physica C **195**, 1 (1992).

[102] H. E. Brandt, Phys. Rev. B **37**, 2349 (1988).

[103] J. M. Delriu, J. Phys. F: Metal Phys. **3**, 893 (1973).

[104] P. Carretta and M. Corti, Phys. Rev. Lett. **68**, 1236 (1992).

[105] P. Carretta, Phys. Rev. B **45**, 5760 (1992).

[106] Y.-Q. Song, W. P. Halperin, L. Tonge, T. J. Marks, M. Ledvij, V. G. Kogan, and L. N. Bulaevskii, Phys. Rev. Lett. **70**, 3127 (1993).

[107] J. T. Moonen and H. B. Brom, Physica C **244**, 1 (1995); *ibid*, 10 (1995).

[108] P. Carretta, Phys. Rev. B **48**, 16570 (1993).

[109] W. G. Clark, W. H. Wong and F. Lefloch, Physica C **235-240**, 1973 (1994).

[110] F. Borsa, Q. Hu, K. H. Kim, B. J. Suh, D. R. Torgeson, P. C. Canfield, M. Xu, and B. Zhong, Physica C **235-240**, 2629 (1994).

[111] M. Tinkham, *Introduction to Superconductivity* (McGraw-Hill-Kogakuse, Tokyo, 1975).

[112] M. Takigawa and G. Saito, J. Phys. Soc. Jpn. **55**, 1233 (1986).

[113] Y.-Q. Song, Phys. Rev. Lett. **75**, 2008 (1995).

[114] E. Fukushima and S. B. W. Roeder, *Experimental Pulse NMR* (Addison-Wesley, Reading, 1981).

[115] J. T. Markert, T. W. Noh, S. E. Russek, and R. M. Cotts, Solid State Commun. **63**, 847 (1987).

[116] M. C. Marchetti and D. Nelson, Physica C **174**, 40 (1991).

[117] S. M. De Soto, C. P. Slichter, H. H. Wang, U. Geiser, and J. M. Williams, Phys. Rev. Lett. **70**, 2956 (1993).

[118] L. M. Bulaevskii, N. N. Kolesnikov, I. F. Schegolev, and O. H. Vyaselev, Phys. Rev. Lett. **71**, 1891 (1993).

[119] S. Kambe, H. Yasuoka, A. Hayashi, Y. Ueda, Phys. Rev. Lett. **73**, 197 (1994).

[120] J. A. Martindale, S. E. Barrett, C. A. Klug, K. E. O'hara, S. M. De Soto, C. P. Slichter, T. A. Friedmann, and D. M. Ginsberg, Phys. Rev. Lett. **68**, 702 (1992).

[121] F. Borsa, A. Rigamonti, M. Corti, J. Ziolo, O. Hyun, and D. R. Torgeson, Phys. Rev. Lett. **68**, 698 (1992).

[122] M. Bankay, M. Mali, J. Roos, I. Mangelschots, and D. Brinkmann, Phys. Rev. B **46**, 11228 (1992).

[123] K. Ishida, Y. Kitaoka and K. Asayama, Solid State Commun. **90**, 563 (1994).

[124] K. E. Gray, Appl. Supercond. **2**, 295 (1994).

[125] T. T. M. Palstra, B. Batlogg, R. B. von Dover, L. F. Schneemeyer, and J. V. Waszczak, Phys. Rev. B **41**, 6621 (1990).

[126] M. Tinkham, Phys. Rev. Lett. **61**, 1658 (1988).

[127] J. H. P. M. Emmen, V. A. M. Brabers, and W. J. M. de Jonge, Physica C **176**, 137 (1991).

[128] J. Clem, Physica A **200**, 118 (1993).

ACKNOWLEDGMENTS

This work was completed with the help of many individuals.

I would like to express my sincere gratitude to my advisor Professor F. Borsa for his guidance, encouragement and constructive criticism which made this work possible. Many helpful discussions, which have been always available, were invaluable. Furthermore, his inexhaustible enthusiasm for research has always made a deep impression on me.

I also would like to thank D. R. Torgeson for his helpful advice and suggestions in NMR instrumentation and experimental technique.

I wish to express my appreciation to Professor D. C. Johnston for many valuable discussions and suggestions on physics. I learned a great deal in the discussions with him.

I also wish to my thanks to Professor A. Rigamonti, Dr. M. Corti, S. Aldrovandi and all the other colleagues at University of Pavia, Italy for their help and collaborations.

I am indebted to many professors and colleagues in our department for their fruitful discussion, collaborations and/or sample preparations, especially to Professor B. N. Harmon, Dr. Ming Xu, J. Sok, J. Y. Rhee, B. K. Cho, P. C. Canfield and L. L. Miller. I am also indebted to Dr. Q. Xiong at University of Arkansas for the sample preparation.

Finally, I am deeply appreciate to my wife Sueyeon, my daughter Juwan, my parents and parents-in-law. Without their encouragement and patience this work could not have been possible.

This work was performed at Ames Laboratory under Contract No. W-7405-Eng-82 with the U.S. Department of Energy. The United States government has assigned the DOE Report number IS-T 1767 to this thesis.

APPENDIX. FIELD-INDUCED ANISOTROPY

A simple derivation of the anisotropy term [Eq. (3.9)] induced by the applied magnetic field is presented. Let us consider for simplicity one spin $\boldsymbol{S}$ which interacts via an antiferromagnetic (AF) exchange interaction J (< 0) with n neighboring spins. The Hamiltonian of the spin can be written as [95]:

$$\mathcal{H} = -J\sum_i \boldsymbol{S}\cdot\boldsymbol{S}_i \,. \tag{A.1}$$

The spins minimize the energy by lining up antiferromagnetically, leading to the energy as:

$$E = nJ \quad (J<0) \,. \tag{A.2}$$

Here we assumed $\boldsymbol{S}$ normalized to 1 ($|\boldsymbol{S}| = 1$) for simplicity. Suppose a field H is now applied perpendicular to the spin direction. The field induces a component of the magnetization along the field as illustrated in Fig. A.1, and the energy of the system is given by

$$\begin{aligned} E &= -nJ\cos(\pi - 2\varphi) - 2\mu H\sin\varphi \\ &= nJ(1-2\sin^2\varphi) - 2\mu H\sin\varphi \,. \end{aligned} \tag{A.3}$$

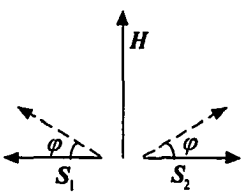

Fig. A.1 Two-spin system aligned antiferromagnetically with an applied field perpendicular to the spin direction.

From Eqs. (A.2) and (A.3), the energy difference ΔE between the situation without the field and with the applied field is

$$\Delta E = -2nJ\sin^2\varphi - 2\mu H\sin\varphi \cong -2nJ\sin^2\varphi \quad (\because J >> \mu H)\,. \tag{A.4}$$

The ΔE represents an effective field induced anisotropy. The sinφ in the above can be written in terms of the effective magnetic moment μ of the spin and the magnetic susceptibility χ using the condition:

$$\langle\mu\rangle = \mu\sin\varphi = \chi H\,. \tag{A.5}$$

Therefore, if we write χ approximately as:

$$\chi = \frac{C}{T+\theta} \approx \frac{C}{\theta} \tag{A.6}$$

with $C = \mu^2/3k_B$ and $\theta = 2nJ/3k_B$ [95], Eq. (A.5) can be written as

$$\sin\varphi = \frac{\chi H}{\mu} = \frac{\mu H}{2nJ}\,. \tag{A.7}$$

From Eqs. (A.4) and (A.6), one finally has

$$D(H) = \Delta E \cong -2nJ\left(\frac{\mu H}{2nJ}\right)^2 = -\frac{\mu^2 H^2}{2nJ}\,. \tag{A.7), (3.9}$$